Resonance Forcing in Catalytic Surface Reactions

vorgelegt von
Master of Science (M.Sc.)
Prabha Kaira

von der Fakultät II - Mathematik - und Naturwissenschaften
der Technische Universität Berlin
zur Erlangung des akademischen Grades
Doktor der Naturwissenschaft
-Dr.rer.nat.-
genehmigte Dissertation

Promotionsausschuss:

Vorsitzender: Prof. Dr. E. Sedlmayr
Berichter: Prof. Dr. H. Engel
Berichter: Prof. Dr. H. H. Rotermund

Tag der wissenschaftlichen Aussprache: 03.02.2009

Berlin 2009
D 83

Kurzfassung

Die vorliegende Arbeit untersucht theoretisch und experimentell die raumzeitliche Musterbildung der CO-Reaktion auf Pt(110) mit den Methoden der nichtlinearen Dynamik. Die Reaktion selbst ist eine gut erforschte und verstandene chemische nichtlineare Reaktion auf einer Einkristalloberfläche. Es werden hier die statistischen und nichtlinearen Eigenschaften (wie Chaos, Turbulenz, Defekte, Cluster) der Musterbildung dieser chemischen Reaktion in Abhängigkeit von Druck und Druckmodulation betrachtet.

Die Untersuchungen werden in einer UHV-Kammer von 10^{-10} mbar Basisdruck durchgeführt. Die Musterbildung der Reaktion auf der Pt(110)-Oberfläche wird mit einem Photoelektronenmikroskop (PEEM) beobachtet. Ein spezieller neu entwickelter Kompressor erlaubt CO-Druckmodulationen großer Amplitude in der UHV-Kammer.

Die Reaktionen werden in subharmonischen 2:1, 3:1, und 4:1 Resonanzen des Verhältnisses Anregungsfrequenz (forcing frequency) zur mittleren natürlichen Fourier-Eigenfrequenz (natural frequency) der Katalysatorfläche betrieben. In der 2:1 Resonanz kann die chemische Turbulenz durch die erzwungenen Schwingungen unterdrückt werden. Mit steigender Amplitude dieser Modulation kann man dann über eine Periodenverdopplungskaskade die Musterbildung der chemischen Reaktion ins Chaos treiben. Bei der 3:1 Resonanz werden zwei-, drei- und sechs-Phasencluster beobachtet, was mit einer entsprechenden subharmonischen Synchronisation (entrainment) des System einhergeht. Die 4:1 Resonanz wird im turbulenten und nicht-turbulenten Bereich untersucht. Im turbulenten Bereich werden 4-Phasencluster gefunden, im nicht-turbulenten Bereich 2-Phasencluster.

Die Experimente werden mit Simulationen des gängigen realistischen Krischer, Eiswirth, und Ertl (KEE) Modells verglichen. Das Modell zeigt einen signifikanten Unterschied zwischen der Eigenfrequenz eines einzelnen (Punkt-)Oszillators und der mittleren Eigenfrequenz des flächig verteilten Systems im turbulenten Bereich. Die natürliche Eigenfrequenz der Fläche ist größer als die des einzelnen-Punkt-Oszillators. Im nicht-turbulenten Bereich tritt dieser Unterschied nicht auf, weil hier die diffusive Kopplung über die Fläche geringer ist. In den meisten Fällen zeigen die Simulationen qualitativ dasselbe Verhalten wie die Experimente. In den Simulationen konnten jedoch keine 2:1 Amplituden-Cluster reproduziert werden Umgekehrt konnten im nicht turbulenten Bereich die theoretisch vorhergesagten 4-Phasen-Cluster nicht experimentell beobachtet werden. Weiterhin wurden im Rahmen der vorliegenden Arbeit die statistischen Eigenschaften chemischer Turbulenz anhand der topologischen Defekte untersucht. Bei steigendem CO-Druck konnte eine Erhhung der Defektanzahl nachgewiesen werden.

Abstract

Pattern formation is a subfield of nonlinear science. In the last few decades pattern forming processes in non-equilibrium systems have been extensively studied. A well known example of pattern-forming non-equilibrium systems is CO oxidation on Pt(110). The dynamics of the reaction are widely understood. Thus, CO oxidation on Pt(110) is utilized as a well-suited model system for the analysis of spatial and temporal pattern formation.

A large part of the present work is focused on the effects of periodic external forcing on chemical turbulence in CO oxidation on Pt(110), investigated both experimentally and theoretically.

Experiments are performed in an UHV chamber with a base pressure of 10^{-10} mbar. Photoemission electron microscopy (PEEM) is used to obtain spatially resolved images of adsorbate patterns on the catalytic Pt(110) surface. A compressor driven reactor which allows global gas-phase forcing for frequency modulations up to 4 Hz was specifically designed.

Experiments are performed in different resonant forcing regimes such as 2:1, 3:1, and 4:1.

Under 2:1 forcing, experiments show that periodic forcing on chemical turbulence may suppress spatial turbulence and could lead to a chaotic response of the system. The path to chaos is given by a period doubling cascade, which could be experimentally followed by the subsequent increase of the forcing amplitude. Two different types, phase clusters and amplitude clusters, are found.

At 3:1 forcing, two, three, and six phase clusters are found at 2:1, 3:1, and 6:1 entrainment respectively.

4:1 resonance forcing is performed in turbulent and nonturbulent regimes. In turbulent regime, four phase clusters are observed while in nonturbulent regime, two phase clusters are observed.

The experimental results are compared with numerical simulations by using the realistic Krischer, Eiswirth, and Ertl (KEE) model. An analysis of the KEE model reveals significant differences between the oscillation frequency of the single oscillator and the mean frequency of the extended system, which appears to be higher in the turbulent state.

Numerical simulations support the findings of experimental results with only small deviations found. Under 2:1 forcing, only phase clusters are observed numerically, while under 4:1 forcing in nonturbulent regime, the four phase patterns could not be observed experimentally.

Thus, the results of this work demonstrate that by means of periodic forcing, turbulence can be effectively controlled and manipulated. Furthermore, the statistical properties of chemical turbulence are determined with increasing order of CO pressure experimentally.

Contents

List of Figures

List of Tables

Chapter 1

Introduction

Spatiotemporal pattern formation in spatially extended systems out of equilibrium maintained through the dissipation of energy which is continuously fed into the system has been a rapidly growing field of research for several decades, due to its importance in many fields such as biology, chemistry, and physics [1–8]. Pattern formation in these systems can lead to coherent pattern formation, which is generated by the interplay of the nonlinear components of the system.

The study of the dynamics of two-dimensional patterns often includes the observation of spatiotemporal disorder, sometimes called turbulence as an analogy to fluid dynamics. Such pattern turbulence has been observed in a wide variety of spatially extended experimental systems with different governing mechanisms [4]. The general study of model equations for these systems has led to the delineation of the categories: phase turbulence [8]; spatiotemporal intermittency [9]; and defect-mediated turbulence [10, 11]. The transition from a simple regular pattern (for example stripes, hexagons, or a spiral) to a time-dependent disorder often involves the spontaneous nucleation of defects in the pattern, which can move through the system as individual entities, or

coherent structures.

Theoretical work by Prigogine and coworkers in 1955 [12, 13] provided the basis for the understanding of how order can emerge out of disorder in systems far from equilibrium. They pointed out in that open systems, i.e., systems open to the exchange of matter and/or energy with their surroundings, kept far from equilibrium could exhibit spontaneous self-organization by dissipating energy to the surroundings to compensate for the entropy decrease in the system. The temporal or spatial structures that can arise in this way are called dissipative structures. A closed system must reach equilibrium and so can exhibit only transitory oscillations as it approaches equilibrium. Sustained oscillations require an open system with a continuous flow of new reagents and removal of waste products. The first chemical model was proposed by Prigogine and Lefever in 1968 and dubbed the "Brusselator" by Tyson in 1973. In 1977, Nicolis and Prigogine summarized the work of the Brussels school in a book entitled Self-Organization in Non-equilibrium Systems. For his work on non-equilibrium systems, Ilya Prigogine was awarded the 1977 Nobel Prize in Chemistry.

Nonlinear phenomena are essential in surface chemical reactions. The mechanisms of surface chemical reactions are often relatively simple. The most prominent examples are the Belousov-Zhabotinsky (BZ) reaction and CO oxidation on Pt(110) [14–16].

A BZ reaction involves several reagents and various intermediate species; the central reaction step is the oxidation of malonic acid by bromate, catalyzed by metal ions. The first observations of kinetic oscillations in a continuously stirred BZ medium were reported by Belousov in 1951 [17, 18]. Two decades later, Zhabotinsky and Winfree observed traveling waves of chemical activity in an unstirred reactor [19, 20].

CO oxidation on Pt(110) has emerged as a fascinating interdisciplinary branch of the natural sciences, since Langmuir's pioneering studies [21], the oxidation of CO over Pt is a classic example of a heterogeneous catalytic reaction. It is considered to be generic due to its apparently simple mechanism, richness of spatiotemporal behavior, and practical relevance [22–24]. Kinetic oscillations in this reaction were first found by Hugo in 1970 on a supported catalyst [25]. This phenomenon was later observed for other types of catalysts (polycrystalline wires and single crystals) both at ultrahigh vacuum (UHV) and sub-atmospheric conditions [26].

In particular, Ertl and co-workers have demonstrated that on Pt(100) and (110), at UHV, the oscillations result from the interplay between bistability and adsorbate-induced surface reconstruction exposing patches with different O_2 sticking probabilities [23, 26]. For his contribution on studies of the catalytic oxidation of CO on platinum, Ertl was awarded the Nobel Prize in Chemistry 2007.

A Modern surface imaging technique, photoemission microscopy (PEEM, described in Chapter 3) with high spatial resolution has provided real time pictures of propagating fronts, spiral waves, target patterns, standing waves, and chemical turbulence. Before these spatial features could be resolved, work function measurements had already revealed that the reaction rate may become oscillatory and even chaotic.

Controlling deterministic chaos has become an active field in the study of nonlinear dynamics over the past few decades. Since the pioneering work of Ott, Grebogi, and Yorke [27], significant progress [28–31] has been achieved in controlling chaos in systems with few degrees of freedom. These efforts have been naturally extended to control spatiotemporal chaos [32] in spatially extended systems, due to it's many potential applications in many fields: plasma devices [33]; laser systems [34]; chemical reactions [35]; and biological systems [36], where both spatial and temporal dependence need to be considered.

Theoretically spatiotemporal chaos has been extensively studied in the complex Ginzburg-Landau equation (CGLE) system [37], which describes universal dynamics features of spatially extended systems near a supercritical Hopf bifurcation. It exhibits defect mediated turbulence or spiral wave turbulence in a wide range of parameter regions.

In order to control spiral wave turbulence in spatially extended systems, global control methods are practical since local access to all system elements is often difficult to achieve. Previous studies performed in the framework of abstract models have theoretically investigated the effects of periodic forcing [38–41] and different schemes of global feedback [42–44], suggesting that turbulence and pattern formation can be successfully controlled in nonlinear systems.

As a recent theoretical contribution, Davidsen *et. al.* studied the dynamics of fronts between phase-locked domains in resonantly forced catalytic CO oxidation on Pt(110)

[45]. Their numerical investigations were carried out using the Krischer, Eiswirth, and Ertl (KEE) model, a well-established realistic model of the CO oxidation reaction [46]. Motivated by similar observations in the forced CGLE [47, 48], they focused on explosion-type front instabilities that can be observed if the forcing amplitude is decreased below a critical value.

In the 2:1 resonantly forced regime, this instability gave rise to a disordered state of defect mediated turbulence. Depending on the forcing parameters, a cascade of period doubling bifurcations was observed as the front instability was approached with decreasing forcing amplitude.

In the case of 3:1 resonance forcing, a labyrinthine structure emerged. Interestingly, resonance with a bistability between 3:1 and 2:1 locking to the external force can be observed.

The present work is focused on spatiotemporal pattern formation in CO oxidation on Pt(110). In particular, control of turbulence by resonance forcing is studied. Also, the effect of resonance forcing is analyzed theoretically in extended systems by using the KEE model. Furthermore, the effect of CO pressure on defect mediated turbulence is presented and applied experimentally.

The outline of the thesis is as follows. In Chapter 2 the basic concept of nonlinear dynamics and CO oxidation on Pt(110) is described in detail.

Chapter 3 deals with the experimental setup, numerical method, and the method used for the pattern analysis. In the first section, the laboratory setup, Photoemission electron microscope (PEEM), implementation for periodic forcing, and the modification is briefly discussed.

In the second section the numerical method and implementation for the resonance forcing is explained. Finally in the last section the method used for the pattern analysis is explained.

In Chapters 4 and 5, control of chemical turbulence by high frequency resonance forcing is investigated in detail experimentally and theoretically, respectively.

In Chapter 6, the effect of CO pressure on defect mediated turbulence is considered

experimentally. Topological defects can be identified in the phase and amplitude representation of the data and are characterized statistically.

Finally, Chapter 7 summaries the basic results presented in this thesis and gives possible perspectives for future research.

Chapter 2

Basic Concepts

A reaction diffusion system is an extended nonlinear system. The field of nonlinear systems is one that has been rapidly developing for the past 30 years. A nonlinear system is defined as one which does not satisfy the superposition property. The simplest form of nonlinear system is the static nonlinearity where the output depends only on the current value of input but in a nonlinear manner, for example the mathematical relationship.

$$y(t) = ax(t) + bx^3(t) \tag{2.1}$$

where the output is a linear plus cubed function of the input.

In the first section of this Chapter, we briefly discuss the basic concepts of nonlinear dynamics and in the second section, the oxidation of carbon monoxide on Pt(110) single crystal surface is introduced in detail.

2.1 Nonlinear Dynamics

The dynamic behavior of a single element with no diffusion coupling can be explained in terms of a set of n coupled ordinary differential equations.

$$\frac{\partial \mathbf{u}}{\partial t} = \mathbf{f}(\mathbf{u}, \mathbf{p}) \tag{2.2}$$

where the function $\mathbf{f}(\mathbf{u}, \mathbf{p})$ represents the kinetics of the reaction and depends on a set of time dependent concentrations of reacting species $\mathbf{u} = (u_1, u_2, u_3, ...u_n)$ and system parameters $\mathbf{p} = (p_1, p_2, p_3, ..., p_m)$. In a chemical context, $\mathbf{u}$ represent concentrations and $\mathbf{p}$ the parameters (i.e., rate constants, temperature, reactant composition, flow rate, etc.).

2.1.1 Limit Sets, Stability, and Bifurcations

The concepts of phase space and phase portrait are important tools for visualizing the evolution of a system. Solving the dynamic system equation (2.2) for each variable $u_1, u_2, u_3...., u_n$ gives a point in phase space. The trajectories in phase space are the temporal evolution of a system with some initial conditions. The deterministic nature of dynamics uniquely determines the function f for a given initial condition. A phase portrait is a geometric representation of the trajectories of a dynamical system in the phase plane.

Subsets of phase space that are approached by the trajectories as $t \to \pm\infty$ are called limit sets. The limit sets with $t \to +\infty$, are called attractors. A system may have various attractors; they may correspond to stationary, periodic, quasi-periodic, or chaotic dynamical states. Limit sets with $t \to -\infty$ are called repellers.

Many features of system dynamics can be understood by the stability analysis of the fixed points of the system.

The type of limit sets (fixed points) depends on the chemical kinetic term $\mathbf{f}(\mathbf{u}; \mathbf{p})$ and on the dimension n of phase space. While fixed points are the only possible attractor

in one-dimensional phase spaces, another important type of attractor is possible in two-dimensional phase spaces, namely the limit cycle. A limit cycle on a plane or a two-dimensional manifold is a closed trajectory in phase space having the property that at least one other trajectory spirals into it as time $t \to +\infty$. In cases where all of the neighboring trajectories approach the limit cycle as time $t \to +\infty$, it is referred as a stable limit cycle (see Fig. 2.1). Stable limit cycles imply self sustained oscillations. Any small perturbation from the closed trajectory would cause the system to return to the limit cycle, making the system stick to the limit cycle.

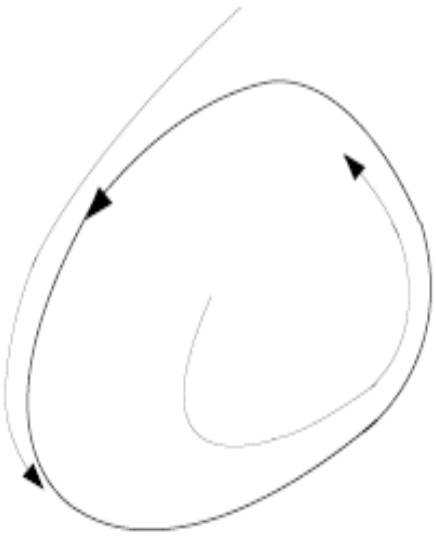

Figure 2.1: Phase space portrait of the stable limit cycle.

Stability

The stationary states or fixed points of system are denoted as $\mathbf{u_s}$ and satisfy the condition $\dot{\mathbf{u}} = 0$. Consider any infinitesimal small perturbations $\delta\mathbf{u}$ on any orbit $\mathbf{u}_0$ leading to $\delta\mathbf{u}(t) = \mathbf{u}(t) - \mathbf{u_s}$.

The difference vector $\delta\mathbf{u}(t)$ is inserted into equation (2.2) and $\mathbf{f}$ is expanded around $\mathbf{u_s}$ in a Taylor series, where only the linear term is kept yielding

$\dot{\delta\mathbf{u}} = \mathbf{J}(\mathbf{u_s})\delta\mathbf{u}$ where $J_{ij} = \frac{\partial f_i}{\partial u_j}$

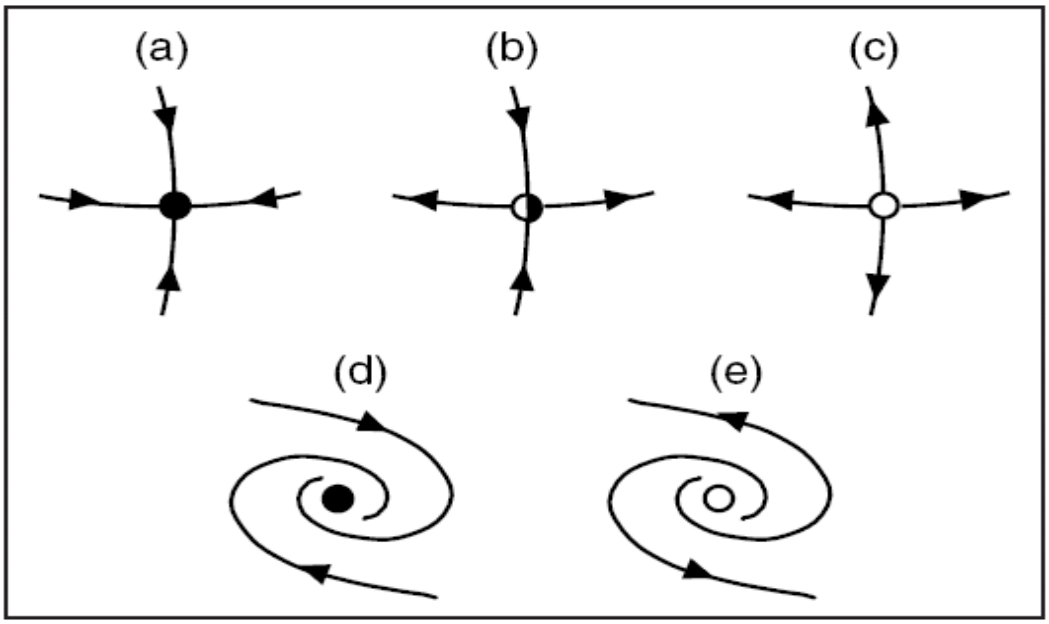

Figure 2.2: Fixed points in two-dimensional phase space. (a) Stable node, (b) saddle point, (c) unstable node, (d) stable focus, and (e) unstable focus.

The eigenvalues λ_1,λ_2,...λ_n of the linear evolution matrix $\mathbf{J}$ evaluated at a fixed point $\mathbf{u_s}$ govern its stability. The fixed point is stable if the real parts of all eigenvalues λ_i are negative; it is unstable if the real part of at least one eigenvalue is positive. In two-dimensional phase space, the eigenvalues λ_1 and λ_2 may either be real or complex conjugated. Different types of fixed points for a two-dimensional vector field are summarized in Fig. 2.2.

Bifurcations

The stability of a fixed point may changed when a system parameter is changed and at least one of the eigenvalues of a fixed point changes its sign. This change is called bifurcation.

If a control parameter μ having a critical value μ_c is varied around the critical value, this leads to non-stationary behavior. The simplest example of bifurcation leading to non-stationary dynamical behavior is the supercritical Hopf bifurcation, see Fig.

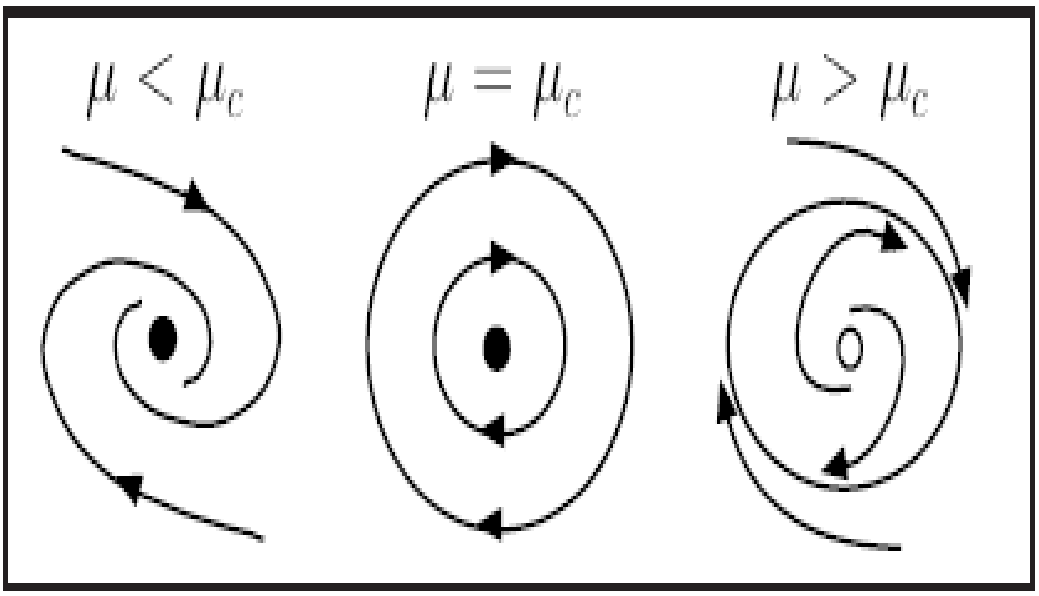

Figure 2.3: Phase portraits in the vicinity of a supercritical Hopf bifurcation.

2.3. In subcritical Hopf bifurcation the existing solution becomes stable and newly emerging solutions are unstable. As an appropriate parameter μ is varied beyond its critical value μ_c, a stable focus becomes unstable and simultaneously a stable limit cycle is born. Sufficiently close to the bifurcation point, the oscillations are harmonic and amplitude follows a square root dependence $A \sim \sqrt{\mu - \mu_c}$. Far from the Hopf bifurcation, the amplitude may become large and strongly anharmonic, depending on the properties of the system. Supercritical Hopf bifurcation does not depend on the direction of the parameter change.

Further examples of local bifurcation include the subcritical variant of Hopf bifurcation. Supercritical and subcritical Hopf bifurcations are displayed in Fig. 2.4. In the subcritical case, the oscillations are born suddenly with finite amplitude at one critical parameter value. Fig. 2.4(b) illustrates the situation when an unstable limit cycle born in a subcritical Hopf bifurcation is stabilized in a saddle-node bifurcation (a stable node and a saddle point appear at the bifurcation point) of limit cycles. In subcritical Hopf bifurcation, when the parameter is scanned in the opposite direction,

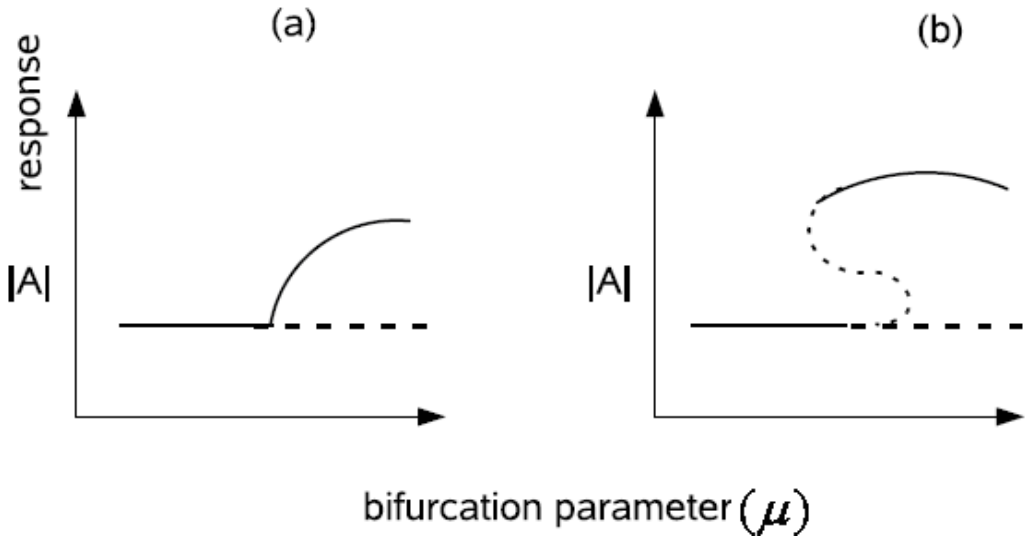

Figure 2.4: The amplitude $|A|$ of the limit cycle is shown as a function of the control parameter μ in supercritical Hopf bifurcation (a), and subcritical Hopf bifurcation with stabilized limit cycle (b). Solid (dashed) lines denote stable (unstable) states.

the oscillations disappear at another critical parameter value and hysteresis occurs. Detailed information about limit sets and their stability can be found in [49].

2.1.2 Extended Dynamics

Pattern formation is a ubiquitous phenomenon in the dynamics of extended nonlinear systems. Patterns in extended systems arise as a result of the interplay of many factors including nonlinearities, external forcing and/or excitability of the medium, spatial interactions, and internal dissipation.

In an extended or distributed system, the elements can be considered as being composed of many individual components. Extended systems are commonly classified according to the local dynamics of their individual elements [50]. Fig. 2.5 shows the schematic diagram of monostable, bistable, excitable, and oscillatory systems.

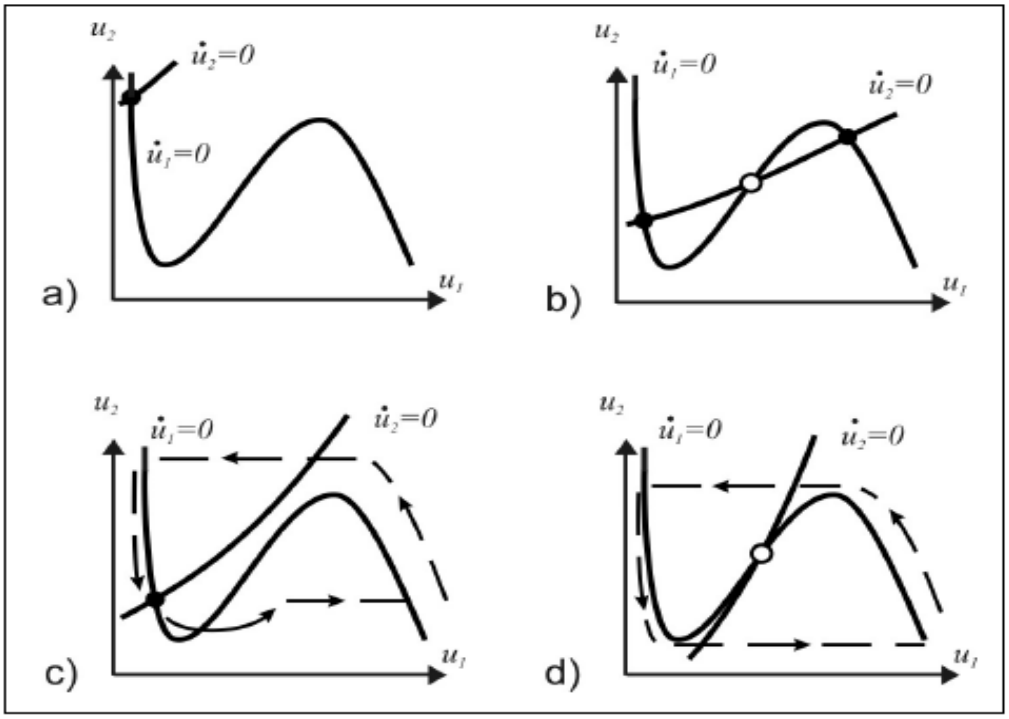

Figure 2.5: Schematic phase space diagrams. (a) monostable, (b) bistable, (c) excitable, and (d) oscillatory dynamics.

Monostable System

In a monostable system (Fig. 2.5(a)) the dynamics is determined by the stable fixed point. Under perturbation the system experienced damping and always returned to the same stable steady state.

Bistable systems

A bistable system is characterized by the presence of two stable steady states separated by a saddle point. In other words bistability refers to the situation in which two stable steady states coexist. The nullclines (the line in phase space obeying $\dot{\mathbf{u}}_1 = 0$, $\dot{\mathbf{u}}_2 = 0$)

of a bistable system possesses three intersection points, which correspond to two stable fixed points separated by a saddle point (Fig. 2.5(b)).

For small perturbations the system remains in one of the stable states, while under sufficiently strong perturbations transitions between the two states may occur. Bistability often arises as a result of symmetry breaking the instabilities of uniform states.

Bistability comes from the fact that its free energy has three critical points with two minima and one maximum. By default, the system state will be in either of the minima states, because that corresponds to the state of lowest energy. The maximum can be visualized as a barrier. A transition from one state of minimal free energy requires some form of activation energy to penetrate the barrier. After the barrier has been reached, the system will relax into the next state of lowest energy again. The time it takes is usually attributed as the relaxation time.

Excitable Systems

Excitable systems are characterized by only one stable steady state corresponding to a single intersection of nullclines (Fig. 2.5(c)). For small perturbations away from the equilibrium, the return is monotonic, however, for perturbations beyond a threshold value, the return is not monotonic, but undergoes a large excursion before settling down.

An excitable system remains in a stable configuration in absence of (or in presence of small) perturbations. If the perturbations surpass a threshold, the system performs an excursion in phase space (in most cases independent on the strength of the perturbation), returning back to the original state.

For the system in continuous or discrete media, it usually gives rise to some global behaviors which are believed to be related to the realization of certain functions of the system. A spiral wave is one of a typical global phenomenon of excitable medium, and has been observed in various systems [51–57].

Oscillatory Systems

Oscillatory systems are characterized by a stable limit cycle and an unstable fixed point (Fig. 2.5(d)).

An oscillatory system, however, can be subjected to an external force which may alter the nature of oscillation. For example, a system capable of oscillation can be set to oscillate at a frequency other than a natural frequency. (The natural frequency is the frequency at which a particular object or system vibrates when pushed by a single force or impulse, and is not influenced by other external forces or by damping.)

Traveling pulses, target patterns [58], standing waves [59], and asymmetric target patterns [60, 61] have been observed in the oscillatory systems and in some cases reproduced by numerical simulations.

2.1.3 Periodically Forced System

A nonlinear dynamic system has four states: the fixed point, the periodic motion, the quasi-periodic motion, and the chaotic motion. When the system is in the critical state, a small perturbation of the system parameters may lead to the qualitative change of the system state. Periodic forcing of nonlinear oscillators produces a rich variety of dynamical responses, including frequency locking, quasi-periodic oscillations, period doubling, and chaos [62]. The well known examples are physical, biological, and chemical systems [63–68].

Single Oscillator

Most theoretical studies of periodically forced oscillatory systems have focused on frequency locking phenomena and the onset of chaos in single oscillator models [45, 62]. Frequency locking refers to the property of a forced system to oscillate at a frequency ω which is a rational fraction of the forcing frequency ω_f in some range. These ranges of resonant behavior get wider as the forcing strength is increased, and are commonly refer to as Arnold tongues. The fractional frequencies a forced system can realize follow the Farey rule: between the tongues $\omega_f : \omega = \mathrm{n} : \mathrm{m}$, where $\mathrm{n} : \mathrm{m}$ resonance is denoted as sub-harmonic if $\mathrm{n} > \mathrm{m}$ and super-harmonic if $\mathrm{n} < \mathrm{m}$.

Extended System

The response of a spatially extended system to a periodic stimulus is more complicated than that of a single oscillator since it is possible for individual elements to oscillate with different amplitude and phase with respect to each other. Frequency locking in spatially extended systems can be enhanced or suppressed by diffusive coupling. On the other hand, close to the boundaries of Arnold's tongues stable frequency locked patterns may exist at forcing parameters where single oscillatory elements are not locked. For example, the dominating contribution of the diffusion terms can prevent frequency locking at small forcing amplitudes [41].

In spatially extended oscillatory systems, periodic forcing can change the nature of the phase patterns from traveling waves or spiral waves in the unforced system to standing wave labyrinths [69] or multiphase spirals [70].

Theoretical work on resonantly forced oscillators has focused on the complex Ginzburg-Landau equation (CGLE) (a generic equation for oscillatory systems close to the Hopf bifurcation), FitzHugh-Nagumo, Brusselator, and the Krisher, Eiswirth, and Ertl (KEE) model [41, 45, 69, 71].

Frequency locking of extended oscillatory systems has been observed experimentally in the light-sensitive Belousov-Zhabotinsky (BZ) reaction and in CO oxidation on Pt(110). In a BZ reaction the uniform oscillations and spiral wave could be entrained, however, the always stable and spontaneous development of turbulence is not known [72–78], while in catalytic CO oxidation on Pt(110) periodic forcing was used to control chemical turbulence [79, 80]. Catalytic CO oxidations on Pt(110) single crystal surface show both stable oscillations as well as spiral wave turbulence [8, 14].

2.2 CO Oxidation on Platinum Crystal

CO oxidation on a platinum single crystal is one of the most studied heterogeneous catalytic reactions due to its simplicity and it can be treated as model system for the experimental and theoretical understanding of heterogeneous catalysis [16]. The catalytic oxidation of CO on a platinum single crystal surface follows the Langmuir-

Hinshelwood mechanism where the two reacting species are chemisorbed on the catalyst surface before the reaction takes place [21]. Under UHV condition with certain sets of control parameters (partial pressure of CO, O_2, and temperature (T)), different spatiotemporal patterns can be observed [81, 82].

Different surface imaging techniques like photoemission electron microscopy (PEEM) [14, 83–85], Reflection Anisotropy Microscopy (RAM) [22, 86], and Ellipsomicroscopy for Surface Imaging (EMSI) [87] can be used to study the pattern formation on Pt surface. In particular, PEEM is used as a powerful tool for real-time pattern formation on catalytic surface due to its non-destructive imaging nature.

2.2.1 The Platinum(110) Surface

A clean Pt(110) single crystal surface is a face centered cubic (fcc) structure at room temperature, having lattice constant a = 0.392 nm. The (110) surface of fcc metals is the most open of the low Miller index surfaces therefore it has the lowest surface atomic density and the highest surface energy.

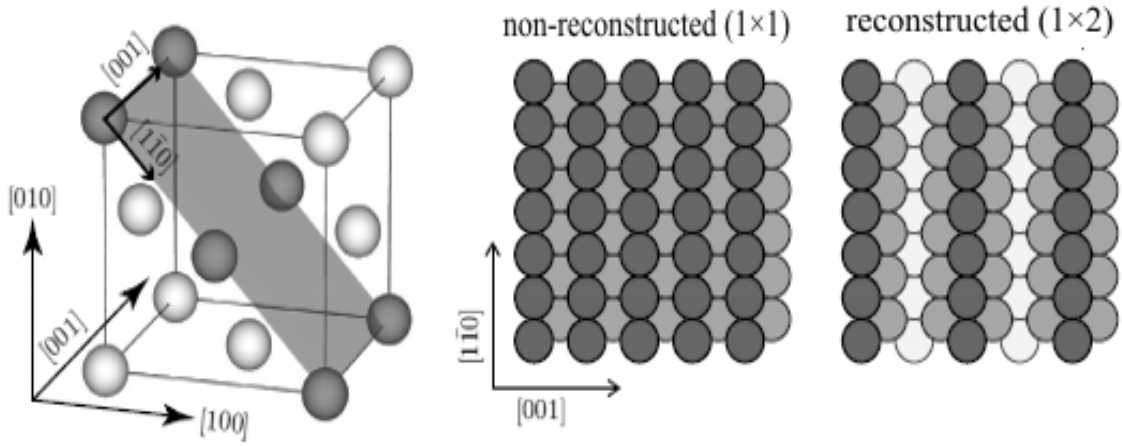

Figure 2.6: Face centered cubic (fcc) crystal structure of Pt(110) (left) and the (1×1) and (1×2) structure of the Pt(110) (right).

In the non-reconstructed form, also known as (1×1), the platinum atoms on (110) surface are arranged according to their bulk position, however, the clean Pt(110) surface undergoes a reconstruction to lower its surface energy that leads to a missing row structure characterized by (1×2) [88–92]. The (1×2) structure is composed of alternating rows and troughs of Pt atoms in the $[1\bar{1}0]$ direction as seen in Fig. 2.6.

2.2.2 Interaction of Adsorbates with Surface

When atoms or molecules adsorb on ordered crystal surfaces, they usually form ordered layer structures over a wide range of temperatures and surface coverage. The driving force for ordering originates in mutual interatomic interactions. Here, an important distinction must be made between adsorbate-adsorbate and adsorbate-substrate interactions.

The adsorbate-adsorbate forces are usually small compared to the adsorbate-substrate binding forces, so that the adsorbate locations are determined by an interplay between their entropy-related accessibility and the optimum adsorbate substrate bonding. The adsorbate-adsorbate interactions dominate the long-range ordering of the over-layer. These interactions can be studied experimentally by examining, e.g. the changes in the over-layer structure as a function of coverage, or by theoretical calculations. The surface coverage is thus an important parameter in ordering.

The effects of a strong adsorbate-substrate bond on the surface structure of the substrate can be large. The presence of an adsorbed over-layer often removes the reconstruction of clean surfaces and the substrate surface atoms usually return to their bulk-like equilibrium position. The thermodynamic driving force for adsorbate-induced restructuring is the difference in strength of the adsorbate-substrate bonds for the reconstructed and unreconstructed surfaces. More specifically, the loss in adsorption energy is larger than the gain in energy associated with the reconstruction of the clean surface. If massive diffusion-controlled atom transport along the surface is not needed, adsorbate-induced restructuring can occur on the time scale of catalytic reactions (seconds).

Carbon Monoxide Adsorption on Pt(110)

The adsorption of CO on Pt surfaces has attracted much attention because of the many potential applications, such as in car exhaust catalysts where it promotes the oxidation of CO to CO_2. CO generally prefers binding at low coordination sites, such as on-top of a Pt atom or bridging two Pt atoms.

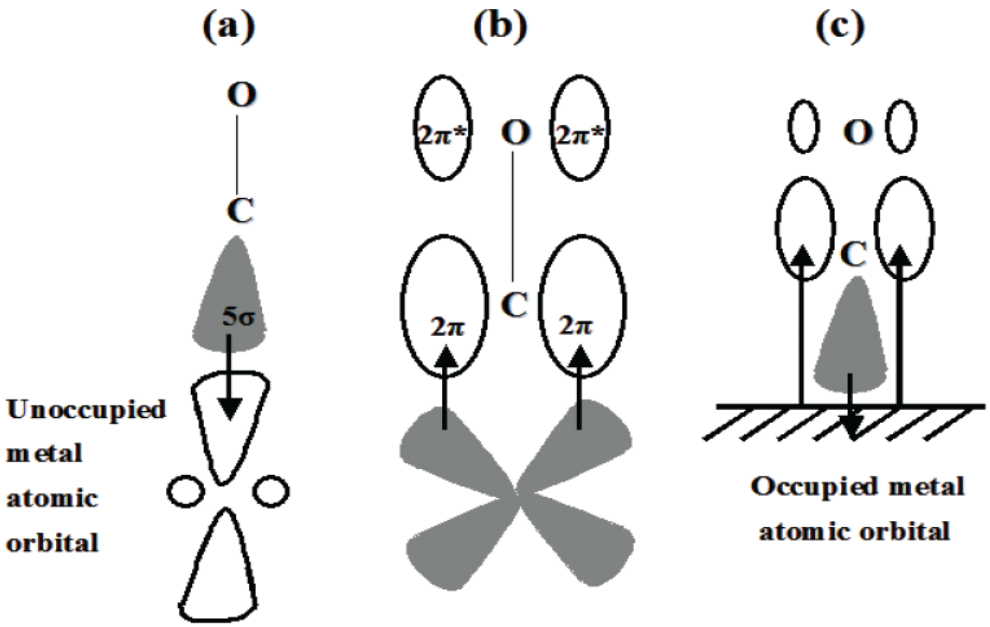

Figure 2.7: Schematic diagram of synergic bonding of CO to a metal. In CO the molecular orbital are $1\sigma^2 2\sigma^2 3\sigma^2 4\sigma^2 1\pi^4 5\sigma^2 2\pi^*$. The 4σ orbital is localized on the oxygen atom while the 5σ orbital is localized on the carbon atom, and both of these orbitals are non-bonding. The empty $2\pi^*$ anti-bonding orbital is also available to take parting the interaction with the surface. This combination of σ and π orbital of CO in the interaction with the surface is called synergic bonding. In the case of molecular chemisorption of CO, a covalent bond is formed by donation of electrons from the 5σ orbital to a vacant metal d orbital (a). At the same time, the full d orbital are able to donate electron density into the vacant $2\pi^*$ orbital (b). On adsorption the situation is analogous (c).

The adsorption of CO on Pt(110) takes place in molecular form and induces a structural change in the surface. The CO bonding to metal surfaces is described in the terms of the Blyholder model, which invokes a donor-acceptor mechanism [93, 94]. The 5σ and the 2π frontier molecular orbital (MO) of the CO molecule are substantially modified by the presence of the metal surface.

A filled 5σ "lone pair" orbital interacts with the empty dσ metal orbital, leading to a partial transfer of electron density to the metal. At the same time the filled metal dπ orbital overlap with the $2\pi^*$ antibonding molecular orbital of the CO (Fig. 2.7) [22, 87, 95, 96]. Moreover, since the 5σ and 2π MO of CO are localized mainly at the C atom, the bonding occurs with the carbon atom facing the surface.

In the clean platinum surface (1×2) structure, the CO sticking probability on Pt(110), s_{co} is close to unity and remains almost constant for low coverage of CO [88, 97, 98]. For higher coverage ($u = 0.35$ monolayers), the sticking coefficient decreases. According to Gasser and Smith who described it in [99], $s_{co} = s^0_{co}(1 - u^q)$ (where q is a mobility parameter between 3 and 4). The CO saturation coverage on Pt(110) is equal to unity [97, 100, 101].

The adsorption of CO on Pt(110) induces a structural change in the surface. The 1×2 missing row reconstruction is lifted to 1×1 bulk phase.

The Adsorption of Oxygen on Pt(110)

The adsorption of oxygen take place dissociatively at temperature 240K. Dissociative adsorption of oxygen was found to proceed via second order kinetics in the free sites [102, 103]. The activation energies for oxygen diffusion are much higher than CO diffusion, and depends on the crystallographic orientation. Diffusion of oxygen is practically limited to the $[1\bar{1}0]$ direction and no transport occurs perpendicular to the ridges of the missing row structure.

Oxygen desorbs only in molecular form. At about 800K recombinative molecular desorption takes place. The dissociation of oxygen on metal surfaces has been modeled by ab-initio fully quantum-dynamical simulations [102, 104].

The initial sticking probability for oxygen on the (1×2) surface of the Pt(110) facet is about 0.4 at room temperature [103, 105, 106]. With growing oxygen coverage, the sticking coefficient decreases to 0.03 for a coverage greater than 0.35 ML [107].

Subsurface of Oxygen

Subsurface oxygen is defined as an atomic oxygen species located directly underneath the uppermost metal crystal layer. The formation of subsurface oxygen can take place only on the non-reconstructed (1×1) surface and subsurface oxygen tends to stabilized (1×1) phase which effects the reaction dynamics.

Subsurface of oxygen is responsible for the drastic decrease of the local work function of the Pt(110) surface.

2.3 Mechanism of the Reaction

In a catalytic process, the reaction occurs in a sequence of elementary steps. This sequence includes adsorption, surface diffusion, chemical rearrangement (bond breaking, bond-forming, molecular rearrangement) of the adsorbed intermediates, and products desorption.

The catalytic oxidation of CO on platinum follows the Langmuir-Hinshelwood mechanism (i.e., CO and oxygen have to adsorb before the reaction to CO_2 can take place), both reactants adsorb on the catalyst surface in order to yield the product [16].

The reaction steps are

$$2\mathrm{CO} + 2\oplus \rightleftharpoons 2\mathrm{CO}_{ad}$$

$$\mathrm{O}_2 + 2\oplus \rightarrow 2\mathrm{O}_{ad}$$

$$2\mathrm{CO}_{ad} + 2\mathrm{O}_{ad} \rightarrow 2\mathrm{CO}_2 \uparrow + 4\otimes$$

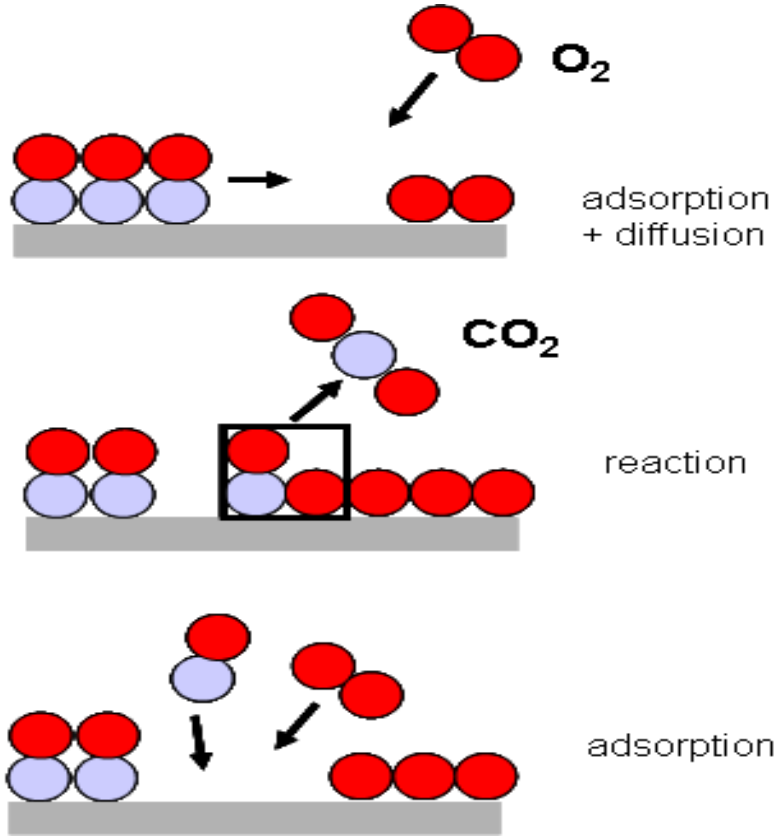

Figure 2.8: Basic reaction mechanism: adsorption of CO and O_2 molecules, CO diffusion, and reaction.

where index *ad* denotes adsorbed molecules or atoms and $\oplus$ stands for a free adsorption site. Due to a high energy barrier for spontaneous reaction of CO and O_2 in the gas phase they have to adsorb before the reaction. The adsorption of oxygen is dissociative. Adsorbed CO molecules are bound to the surface considerably less strongly than oxygen atoms and hence may desorb as well as diffuse on the surface and such processes are negligible for O_{ad} under typical reaction conditions.

At temperatures above 300K, produced carbon dioxide almost immediately desorbs into the gas phase, again leaving free space for adsorption. The reaction mechanism is illustrated in Fig. 2.8.

2.3.1 Bistability

In a certain range of parameters, the system exhibits bistability between a mainly oxygen covered, reactive state, and a non-reactive CO covered state. This bistability can be traced back to an asymmetric inhibition of adsorption. Adsorbed oxygen forms an open structure where CO molecules can still adsorb and react, whereas a fully CO covered surface completely inhibits the adsorption of oxygen, and hence poisons the reaction.

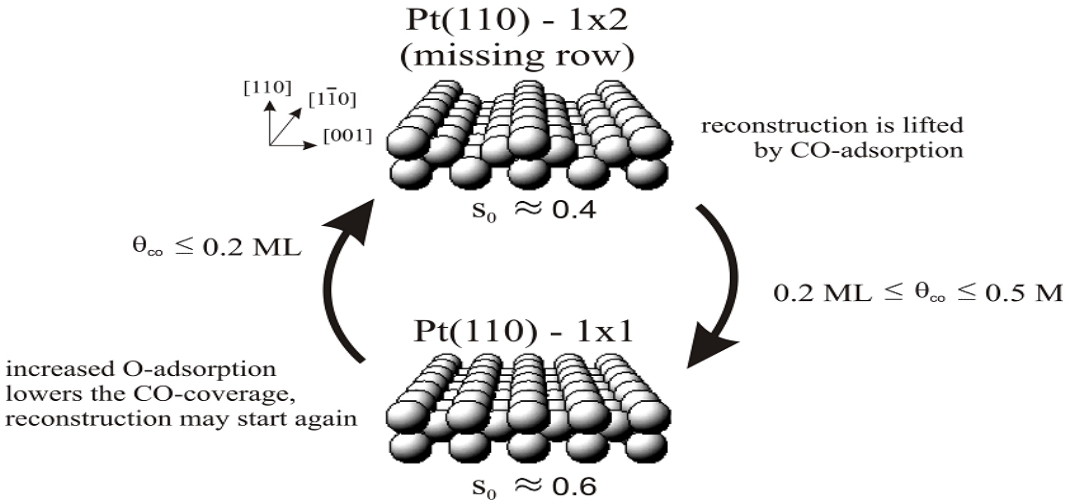

Figure 2.9: Reconstruction from 1×1 to 1×2.

After the sputtering (Ar ion) and annealing a reconstructed (1×2) phase is observed, as illustrated in Fig. 2.9. When CO is admitted in the reconstructed (1×2) phase this reconstruction will be lifted and a phase transition to a non-reconstructed (1×1) phase occurs. CO starts to lift the reconstruction of the surface at a CO coverage of 0.2 ML and completes the reconstruction at a coverage of 0.5 ML. The activation energy for this phase transition in 29 KJ/mol [108].

As already discussed in section 2.2, the sticking coefficient of the oxygen is higher in

the non-reconstructed (1×1) phase compared to the reconstructed one by a factor of 1.5. As a consequence, the surface will transform in to an oxygen covered one. When the surface is oxygen covered, with no CO species to lift the reconstruction, it will reconstruct again. A reconstructed surface has low sticking coefficient for oxygen thus enabling CO to take over. Now the surface become CO covered and the oscillation cycle starts again.

Faceting

Faceting is a process which causes an initially flat, single-crystal surface to separate into two (or three) other surface orientations [109, 110]. This process has been studied intensively on Pt(110) [99, 109, 111].

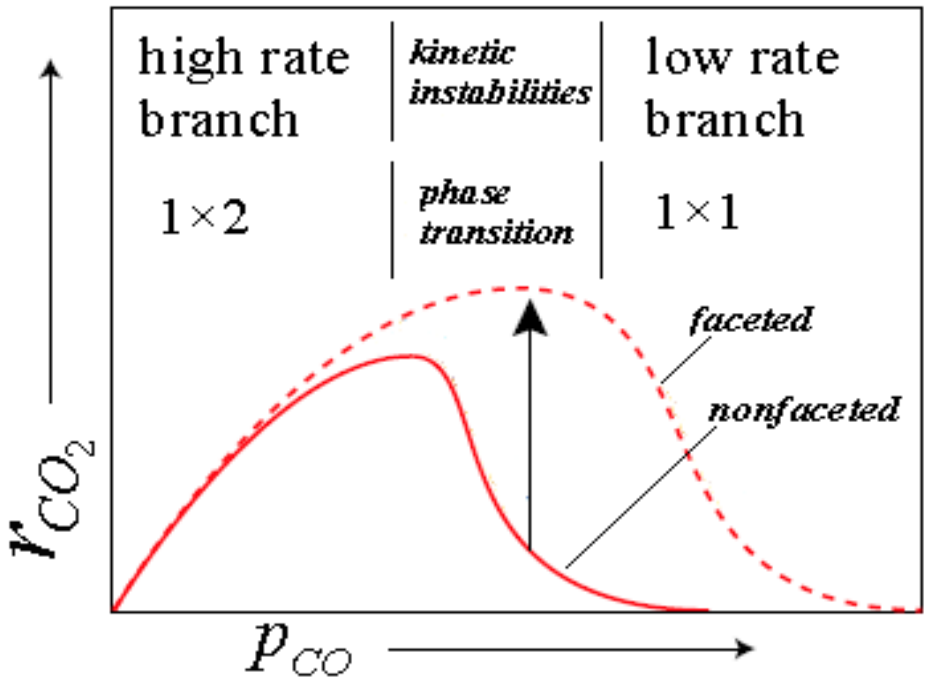

Figure 2.10: Schematic diagram of the relation between the conditions for faceting and the kinetics of catalytic CO oxidation on Pt(110).

Faceting takes place at temperatures below 530K, above this temperature a thermal

reordering process keeps the (110) surface flat. A CO covered 1×1 surface constitutes the starting point of an oscillation cycle. On this surface the reaction rate is low and the facets grow slowly. These facets have a high sticking coefficient for O_2, and at a certain point the surface becomes oxygen covered [23, 112].

The faceting of Pt(110) is associated with an increase in catalytic activity, which in a reaction rate vs. p_{CO} diagram, shows up as a shift of the rate maximum toward higher p_{CO} [23], as displayed in Fig. 2.10.

2.3.2 Spatial Coupling

Spatial coupling in CO oxidation on Pt(110) surface is provided by two different mechanisms: local coupling and global coupling. Surface diffusion of adsorbed CO molecules gives rise to local coupling between neighbored sites.

Global coupling acts in the gas phase as a consequence of mass balance in the reaction. Since the mean free path in the gas phase is typically large in comparison to the size of the chamber, local partial pressure variations that result from the consumption of the educts by the reaction quickly extend to affect the whole system. Therefore, the gas-phase coupling is global.

The interplay between diffusion and gas-phase coupling can lead to phenomena such as synchronous oscillations, standing waves, cellular structures, and spiral wave turbulence [14, 83].

2.4 Mathematical Modeling

The mechanism of low-pressure CO oxidation on Pt(110) is described through a three step reaction-diffusion type model knows as the Krischer-Eiswirth-Ertl (KEE) model [46].

KEE Model

The KEE model is based on decomposition of the entire reaction into elementary steps. It consists of three coupled ordinary differential equations for the local dynamics, taking into account the most significant physical processes.

$$\partial_t u = k_1 s_{CO} p_{CO} - k_2 u - k_3 uv \tag{2.3}$$

$$\partial_t v = k_4 s_O p_{O_2} - k_3 uv \tag{2.4}$$

$$\partial_t w = k_5 (f(u) - w) \tag{2.5}$$

where u, is the local CO coverage, i.e., the fraction of CO adsorption sites on the metal surface that are occupied by adsorbed CO molecules. The second variable, v, is the local oxygen coverage. The third variable, w, specifies the local fraction of the surface area occupied by the non-reconstructed (1×1) structural phase.

The first term in equation (2.3) describes the process of CO adsorption. Here, k_1 is the adsorption rate constant and s_{co} is the sticking coefficient for CO molecules. As mentioned above, the sticking coefficients are coverage dependent. For s_{CO} a precursor effect has to be considered and is modeled following Gasser and Smith [113].

Thus the sticking coefficient of CO is given by the expression,

$s_{CO} = s^0_{CO}(1 - u^3)$

where s^0_{CO} is the initial sticking probability of CO. The term $(1-u^3)$ for CO adsorption describes a precursor effect.

p_{CO} is the partial pressure of CO in the gas phase. The second and the third terms in this equation describe desorption of CO and its reaction with adsorbed oxygen molecules, where k_2 and k_3 are the desorption rate constant respectively.

The second equation (2.4) of the KEE model describes the kinetics of adsorbed oxygen. The first term is the adsorption rate depending on the partial pressure oxygen

molecules, where k_4 , p_{O_2}, and s_O are the impingement rate constants, partial pressure, and sticking coefficient of oxygen molecules respectively.

s_O given by the expression

$s_O = [s^0_{O,1\times1}w + s^0_{O,1\times2}(1-w)](1-u-v)^2$

where $s^0_{O,1\times1}$ and $s^0_{O,1\times2}$ denote the initial sticking probabilities of oxygen on the (1×1) and (1×2) surface.

The last equation (2.5) of the KEE model is a phenomenological mean-field description of the phase transition kinetics. The surface free of CO molecules is in the reconstructed (1×2) phase, while the surface completely covered by CO is in the non-reconstructed (1×1) phase. At intermediate CO coverage, a mosaic of microscopic domains of both structural phases occupy the surface. The characteristic sizes of such domain are, however, on the nanometer scale and cannot be resolved in the above mean-field micrometer scale description. Here, it is simply assumed that, at a fixed CO coverage u, the local fraction w of the surface area in the non-reconstructed phase tends to approach

$f(u) = \frac{1}{1+exp[(u-u_0)/\delta u]}$

The values of parameters u_0 and δ sets the threshold above which the surface structure is affected by the CO coverage and the steepness of the threshold [46, 114].

The partial pressure of the reactants (p_{CO} and p_{O_2}) and temperature T can be changed, which determines the rate constants k_2, k_3, and k_5 according to the Arrhenius activation law,

$k_i = \nu_i exp[Ei/kT]$

Depending upon the control parameters the model exhibits monostable, bistable, excitable, and oscillatory behavior.

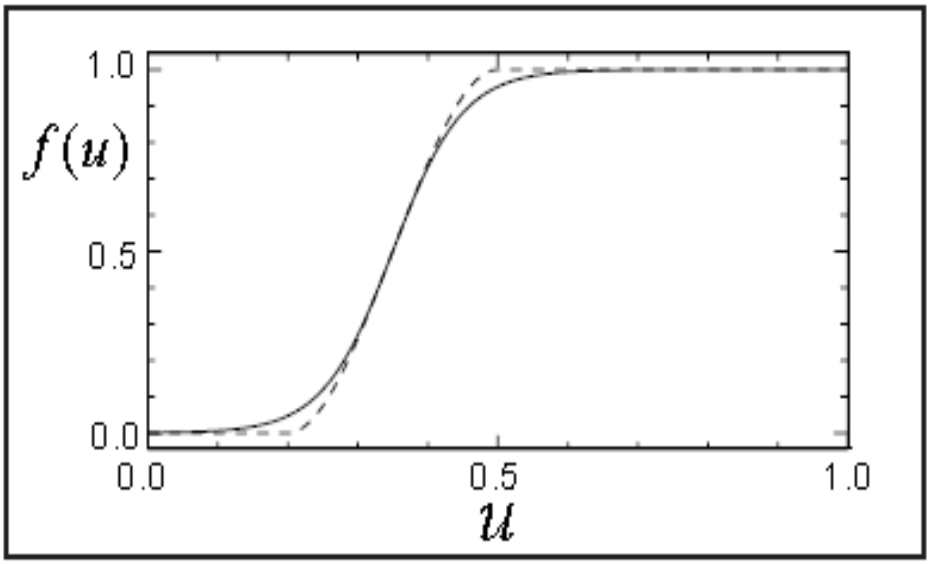

Figure 2.11: The function f (u) for parameters $u_0 = 0.35$ and $\delta u = 0.05$ (solid line), and its piecewise original form (dashed line).

2.5 Pattern Formation in CO Oxidation on Pt(110)

In the 1970s, the group of E. Wicke discovered oscillations of the reaction rate in catalytic oxidation of carbon monoxide [115]. In 1982 Ertl *et. al.* observed the oscillatory kinetics on single crystal surfaces, in CO oxidation on Pt(100) and later in 1986, oscillations were also reported on Pt(110) where they showed rich behavior, ranging from periodic and mixed-mode oscillations to deterministic chaos [26, 116].

The development of spatially resolving techniques such as PEEM [84, 117] has shifted the focus from purely temporal phenomena to spatiotemporal pattern formation. Measurements employing PEEM allow the display of the local work function, which is changed by the adsorbates, across a surface area of about 500 μm in diameter. The evolution of patterns on the catalytic surface can be followed in real time with a spatial resolution of about 0.2 μm. Among surface chemical reactions, by far the richest variety of spatiotemporal patterns has been found in CO oxidation on Pt(110). The observed phenomena include rotating spiral waves, target patterns, standing waves,

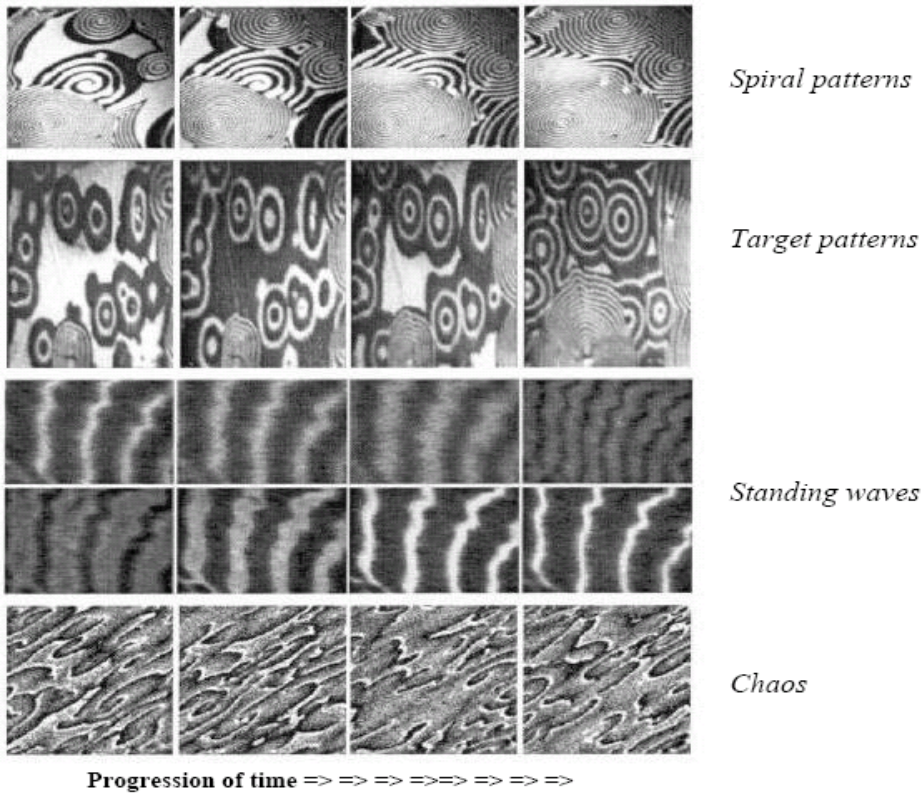

Figure 2.12: Snapshots of PEEM images displaying different patterns in CO oxidation on Pt(110). Dark areas in the images correspond to predominantly oxygen covered regions, and bright areas indicate mainly CO covered regions. (a) Rotating spiral waves, (b) Target patterns , (c) standing waves [122], and (d) chaos.

cellular structures, chemical turbulence, and solitary waves [14, 118–120]. Examples of such patterns are displayed in Fig. 2.12.

Chapter 3

Methods

This Chapter describes the experimental setup used, numerical method used, and the method used to analyze the patterns obtained from the experiments and numerical simulations.

3.1 Experimental Setup

This section explains the UHV, PEEM, implementation for periodic forcing, and modification for high periodic forcing.

3.1.1 UHV Chamber

The experiments presented in Chapters 4 and 6 are conducted in a stainless steel UHV chamber with a volume of 60L and the pressure about 10^{-10} mbar in the chamber. Attached to the UHV chamber are an automated dosing system that keeps the partial

pressures of gases constant within a maximal variation of 0.1, gas supplies for CO and O_2, and two pressure gauges that allow for controlled dosing of the reactants into the UHV chamber [121]. With the combination of feedback-regulated gas dosing and permanent pumping of the chamber the CO oxidation reaction can be observed under constant flow conditions.

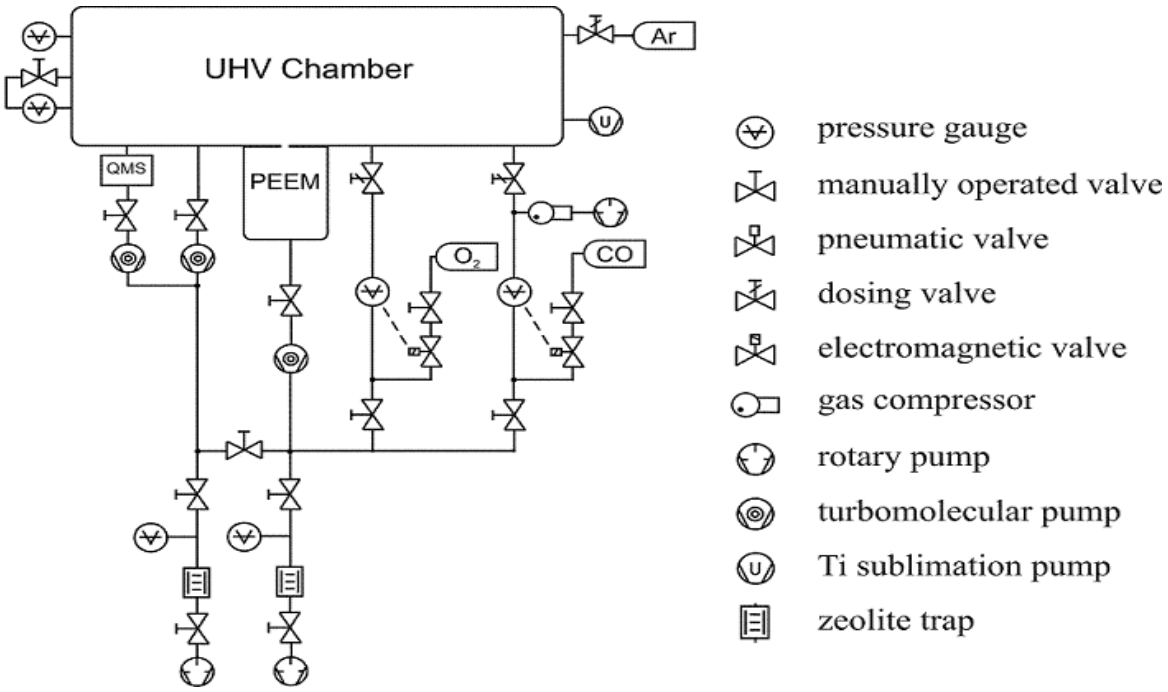

Figure 3.1: Schematic diagram of the ultrahigh vacuum (UHV) chamber with pumping and gas supply system.

The chamber is equipped with a PEEM, a quadrupole mass spectrometer, low energy electron diffraction (LEED), an Ar-ion sputtering gun, and resistive sample heating.

For imaging the spatiotemporal adsorbate patterns on the catalytic surface, the PEEM was used, which operated under differential pumping. Platinum crystal is mounted on a sample holder which allows controlled movement of the sample in x, y, and z-directions as well as radial and azimuthal rotation by electric step. Preparation of the clean platinum single crystal was performed by oxidizing at 750K (10^{-6} mbar), sputtering, and annealing cycles at up to 1100 K to image pattern formation on the

Pt(110) surface, which produces images of the intensity distribution of electrons photoemitted from an area with a typical diameter of about 500 μm.

3.1.2 Photoemission Electron Microscopy (PEEM)

The PEEM is an excellent imaging technique for the real time observation of pattern formation during catalytic reactions [14, 83–85]. The PEEM provides spatially resolved information of reacting species on the surface, since the local work function at a given point depends on the adsorbate coverage on the surface, therefore, images with different brightnesses are obtained due to different values of local work function ($\nabla\phi$).

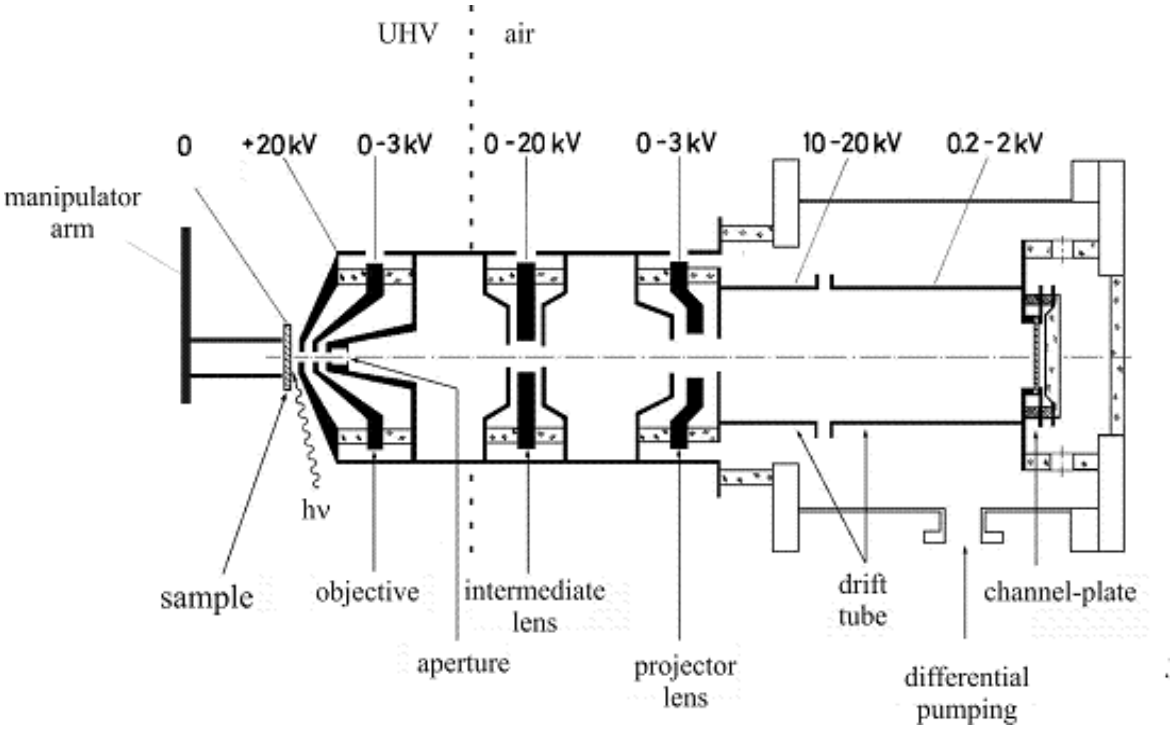

Figure 3.2: Schematic diagram of the photoemission electron microscope (PEEM).

The clean Pt surface has the lowest work function and displays therefore the brightest image. Compared to the clean Pt(110) surface, a monolayer of oxygen coverage increases the work function ($\nabla\phi$) by 0.8eV, thereby strongly decreasing the brightness

of PEEM images. Full CO coverage also increases the work function but produces a smaller effect ($\nabla\phi = 0.3$eV) [22, 122].

Fig. 3.2 shows the systematic drawing of the PEEM, creating a complete picture of the photoelectron distribution emitted from the imaged surface region. To induce the emission of photoelectrons, the platinum sample is irradiated with ultraviolet light from a 200 W deuterium discharge lamp. The ultraviolet light has a continuous spectral intensity characteristic [123]. The angle of light incidence is about 75^0 from the surface normal. To capture as many photoelectrons as possible for the imaging, the distance between the sample and the objective is small (d = 4 mm.). Within this distance, the electrons are accelerated by a potential difference of about 20kV.

Besides the objective lenses, on the left side in Fig. 3.2, two more lenses are used to create an image of the sample, an intermediate three electrode lens next to the objective lens magnifies the electron image by a factor of 10^2 to 10^3. The lens combination also decelerates the fast electrons to energies for which the channel plate has its highest sensitivity (about 1keV). The channel plate typically amplifies the electron distribution by a factor of 10^3.

Finally, a phosphor screen converts the electron image into a photon image which then recorded by a CCD camera.

An additional problem for investigating surface reactions with PEEM is the restriction of the pressures below 10^{-6} mbar. This is in part circumvented by the differential pumping of the PEEM which allows its operation up to pressures of 10^{-3} mbar even in the presence of the oxygen around the sample. To maintain the three orders of magnitude pressure difference, an aperture of 300 μm in diameter has to be incorporated at the focus of the cathode lenses indicated in Fig. 3.2.

In our experiments, the PEEM instrument has been used to monitor a surface area of 500 μm in diameter. The spatial resolution of the images was about 1 μm. The PEEM is combined with a CCD camera, and provides information on temporal evolution of reacting species on the surface. A frame rate of 25 images per second gives a sufficiently good temporal resolution of the PEEM recordings. The video pictures are stored on a recorder or are used as input for the LABVIEW card controlling the feedback loop.

3.1.3 Implementation for Resonance Forcing

Periodic forcing has been implemented experimentally in gas-phase. Partial pressure variations affect the reaction conditions on the catalytic surface in a uniform way. The automated gas inlet system allowed the controlled modulation of the CO partial pressure in the chamber by changing the dosing rate of CO molecules. Resonance forcing has been implemented by using a frequency generator to control the dosing rate of CO molecules. The schematic diagram of periodic forcing is shown in Fig. 3.3.

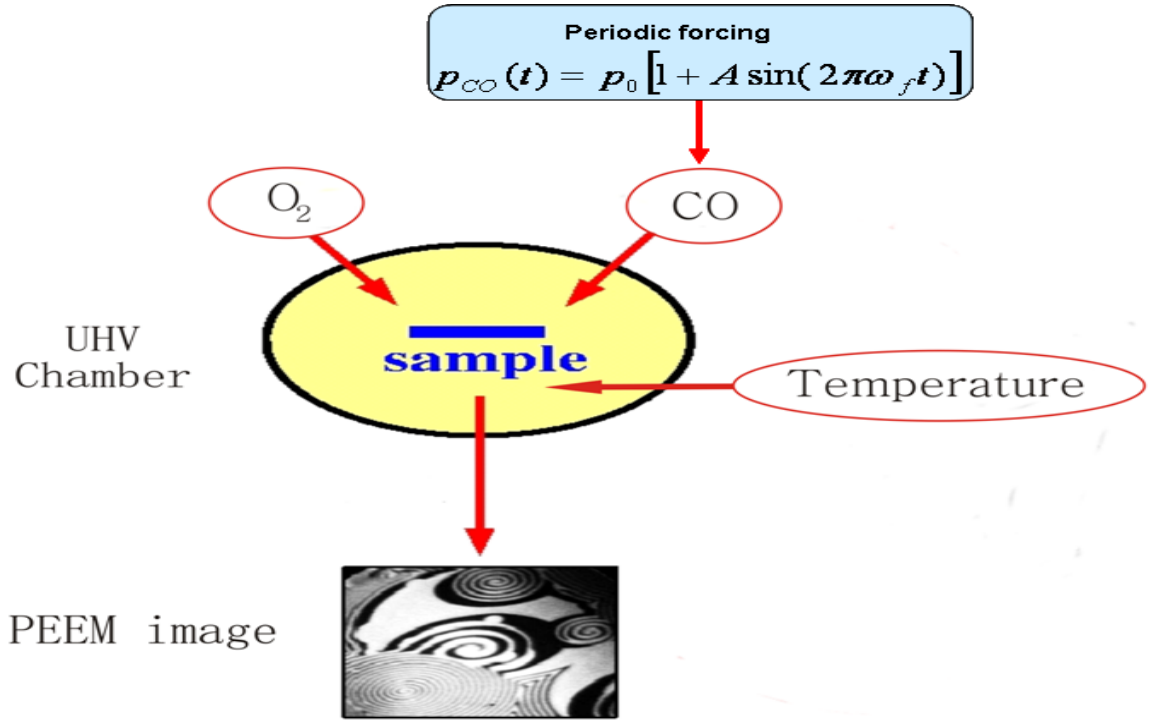

Figure 3.3: Schematic drawing of the experimental setup with periodic forcing.

For resonant forcing, the carbon monoxide pressure p_{CO} in the chamber is varied by:

$$p_{CO}(t) = p_o[1 + Asin(2\pi\omega_f t)], \tag{3.1}$$

where p_o is the base pressure of CO, A is the forcing amplitude, and ω_f is the forcing frequency. In this way, the CO partial pressure in the reaction chamber could be periodically modulated with a nearly harmonic signal of amplitude A and frequency

ω_f, while its temporal average p_o was kept constant. For forcing frequencies $\omega_f \leq$ 2Hz, an electronic valve was used to control the carbon monoxide flux. The valve is connected to the computer and is regulated by an oscillating voltage signal generated by the LABVIEW program. This setup provides the ability to scan over a predefined range of forcing amplitudes and frequencies to measure the system's response in a wide range of the parameter space [124].

Modification: The above setup fails for higher forcing frequencies, as the forcing amplitude is strongly damped.

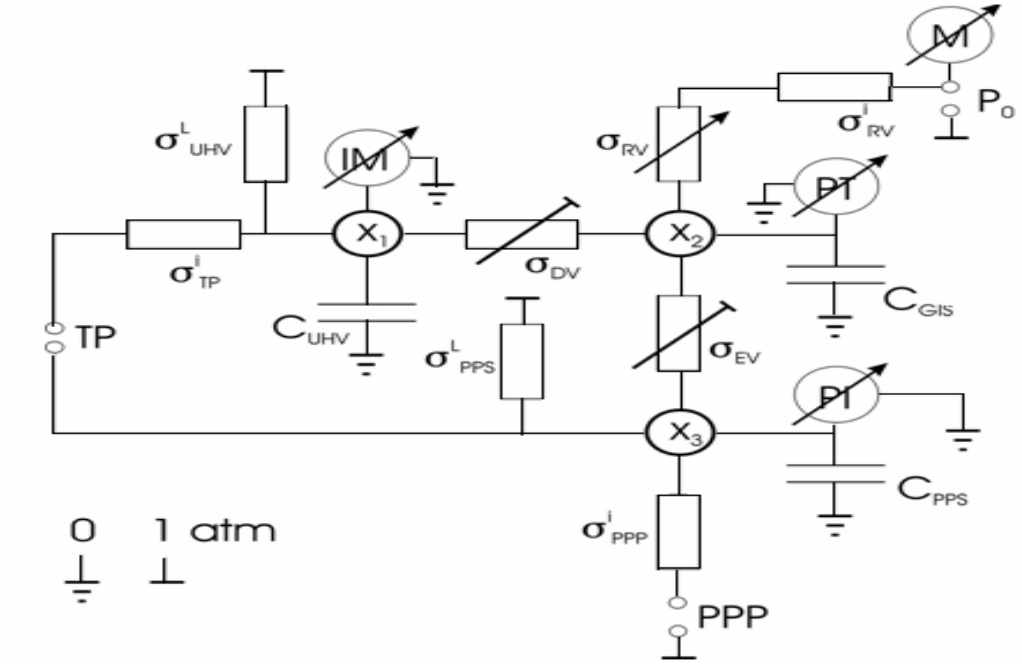

Figure 3.4: The CO pressure regulating system is represented as an electric circuit. Symbols, abbreviations, and indices: σ = conductivity, C = capacity, X_1 = pressure in the UHV chamber, X_2 = regulated CO pressure in the gas dosing system, X_3 = pressure in the pre-pressure system, DV = dosing valve, EV = exhaust valve, GDS = gas dosing system, i = inner, IM = ionization manometer, L = leakage, M = manometer, MOT = compressor, P_0 = pressure after manometer, PPP = pre-pressure pump, PPS = prepressure system, PI = Pirani pressure sensor, PT = pressure transducer, RV = regulating valve, TP = turbo pump, and UHV = ultrahigh vacuum.

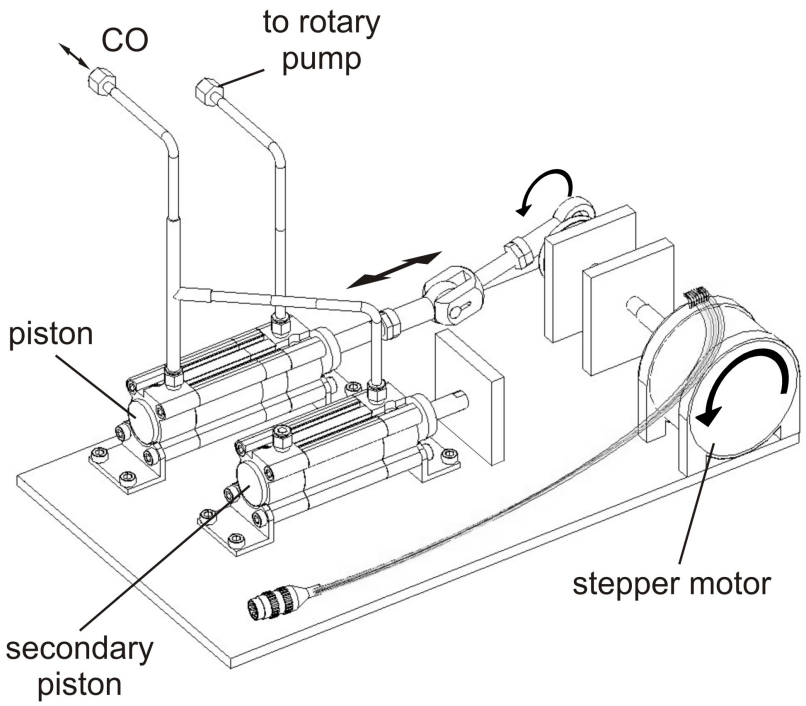

Figure 3.5: Design of the forcing compressor.

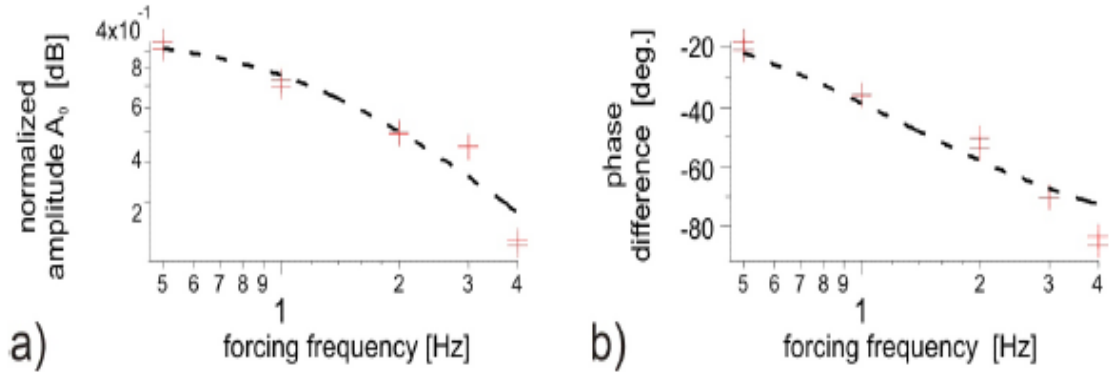

Figure 3.6: Bode plots of the UHV chamber showing the compressor (a) forcing frequency vs. phase, and (b) amplitude of resulting oscillations inside the UHV chamber. The experimental results are shown as (+), while the dashed lines indicate approximation fits with a first order low-pass filter function.

Based on the analogy between electrical and pneumatic circuits [125], the UHV chamber and the CO pressure regulating system was analyzed in detail.

Analysis of the UHV chamber and the whole CO pressure regulating system reveals its intrinsic low pass filtering characteristics, as could be deduced from the equivalent circuit diagram, given in Fig. 3.4. It neglects chemical and thermal driven flows in the system and it ignores the finite velocity of the gas.

In order to enlarge the oscillation amplitude at higher frequencies, a small self-built compressor was implemented in the gas dosing system (Fig. 3.5). This compressor basically consists of a piston which periodically draws CO from the gas line, compresses and pumps it back to the pre-pressure line, resulting in an harmonic modification of the p_{CO} in the chamber. The forcing frequency is adjusted by the velocity of the stepper motor driving the piston, while the amplitude can be regulated in a limited range by an additional cylinder setting an offset gas volume.

The forcing frequency is adjusted by the rotational frequency of the stepper motor driving the piston compressor. The other side of the piston is pumped by a rotary pump to ease the movement of the piston, since the CO pressure is normally operated between 50 and 100 mbar.

This new device allows the application of periodic forcing at frequencies up to 4Hz and well-defined amplitudes. The frequency response of the UHV chamber on partial pressure in the pre-pressure line is shown as Bode plot in Fig. 3.6. The measurement of the $p_{CO} = 2 \times 10^{-4}$ mbar in the UHV chamber was performed by using a ionization manometer (Leybold IM510 with VIG17-head) in linear scaling. The experimental results are shown as (+). The solid line indicates the linear approximation fit with a chamber's time constant.

3.2 Numerical Method

Mathematical modeling of the experiments is performed using a realistic model of catalytic CO oxidation on Pt(110) known as the KEE model, introduced in Chapter 2. The model takes adsorption of CO and oxygen molecules, reaction rates, desorption of

CO molecules, the structural phase transition of the Pt(110) surface, surface diffusion of adsorbed CO molecules, surface roughening into account while faceting, formation of subsurface oxygen, and the effects of internal gas-phase coupling are not considered.

The differential equations describing a single element of the extended system are given by:

$$u_t = k_1 s_{co} p_{co}(1 - u^3) - k_2 u - k_3 uv + D\nabla^2 u \tag{3.2}$$

$$v_t = k_4 p_{O_2}[s_{o,1\times1} w + s_{o,1\times2}(1 - w)](1 - u - v)^2 - k_3 uv \tag{3.3}$$

$$w_t = k_5(\frac{1}{1 + exp[(u - u_0)/\delta u]} - w) \tag{3.4}$$

Numerical simulations of the model were performed using a second-order finite difference scheme for the spatial discrimination with a grid resolution of dx = 4 μm. For the temporal discrimination an explicit Euler scheme with a fixed time steps dt = 0.001s is used. A system size of 400 μm^2 and no-flux boundary condition is taken.

3.2.1 Implementation for Resonance Forcing

Like in the experiments, resonance forcing is artificially introduced by means of controlled variation of CO partial pressures. Therefore, to implement resonance forcing in the CO oxidation model, it is assumed that the CO partial pressure p_{CO} in equation (3.2) is not constant but varies according to the equation (3.1).

All of the numerical simulations were carried out in a programming tool called Matlab. In all cases, model equations were integrated in time by an Explicit Euler method. The model parameters used for the numerical simulations are given in Tables 3.1 and 3.2.

3.3 Pattern Analysis

For further analysis, either the experimentally obtained PEEM image sequence or the numerical values of the CO surface coverage (for model simulations) are used. The course of time is visualized by space-time plots, showing the pattern evolution along a chosen line within the two-dimensional data as a function of time. Oscillatory behavior as well as motion of cluster boundaries cross-sectioning this line can be determined from these plots. Furthermore, the average image intensity in a small region of the platinum surface is shown in comparison to the forcing as a function of time. From these plots, the state of entrainment can be easily determined.

To measure the temporal response of the patterns, a frequency demodulation technique is used. At each image pixel the brightness of the image is recorded, giving an ensemble of time series of the local system dynamics. The Fourier transform of these time series is calculated, and the complex Fourier coefficients of the main frequency component allow for amplitude and phase representations of the data. The spatial distribution of amplitude and phase is analyzed as well as the overall distribution of phase states, given as phase histogram and mapping into the complex plane.

k_1	$3.14 \times 10^5\ s^{-1} mbar^{-1}$	Impingement rate of CO
k_2	$10.23\ s^{-1}$	CO desorption rate
k_3	$283.8\ s^{-1}$	Reaction rate
k_4	$5.86 \times 10^5\ s^{-1} mbar^{-1}$	Impingement rate of O_2
k_5	$1.610\ s^{-1}$	Phase transition rate
s_{CO}	1.0	CO sticking coefficient
$s_{O,1\times1}$	0.6	Oxygen sticking coefficient on the 1×1 phase
$s_{O,1\times2}$	0.4	Oxygen sticking coefficient on the 1×2 phase
$u_0, \delta u$	$0.35, 0.05$	Parameters for the structural phase transition
D	$40\ \mu^2 s^{-1}$	CO diffusion coefficient
p_{O2}	$1.2 \times 10^{-4}\ mbar$	O_2 partial pressure
p_O	$4.6219548 \times 10^{-5}\ mbar$	Base CO partial pressure

Table 3.1: Parameters of the KEE model (Turbulent regime)

k_1	$3.14 \times 10^5\ s^{-1} mbar^{-1}$	Impingement rate of CO
k_2	$10.21\ s^{-1}$	CO desorption rate
k_3	$281.6\ s^{-1}$	Reaction rate
k_4	$5.86 \times 10^5\ s^{-1} mbar^{-1}$	Impingement rate of O_2
k_5	$1.60\ s^{-1}$	Phase transition rate
s_{CO}	1.0	CO sticking coefficient
$s_{O,1\times1}$	0.6	Oxygen sticking coefficient on the 1×1 phase
$s_{O,1\times2}$	0.4	Oxygen sticking coefficient on the 1×2 phase
$u_0, \delta u$	$0.35, 0.05$	Parameters for the structural phase transition
D	$39.59\ \mu^2 s^{-1}$	CO diffusion coefficient
p_{O2}	$1.2 \times 10^{-4}\ mbar$	O_2 partial pressure
p_O	$4.75 \times 10^{-5}\ mbar$	Base CO partial pressure

Table 3.2: Parameters of the KEE model (Nonturbulent regime)

Chapter 4

Resonance Forcing: Experimental Results

4.1 Natural Frequency of the System

The natural frequency of the system is defined as the main frequency of the Fourier spectrum of the local PEEM intensity, i.e., the frequency with the highest amplitude in the power spectrum of a local intensity time series. For a quick measurement of the natural frequency during the experiments, a section of the PEEM image with a size of 10×10 pixels is chosen, its mean intensity is calculated, and its time series Fourier transformed (Fig. 4.1).

The natural frequency is determined from the maximum of the power spectrum. Even though the frequency analysis is performed locally, its validity is assumed for the whole sample. To prove this assumption, 2500 pixels, equally distributed over the region of interest were chosen from the same video sequence. The time series of the one single pixel is shown in Fig. 4.2.

However, on a time scale of several minutes the natural frequency slowly decreases al-

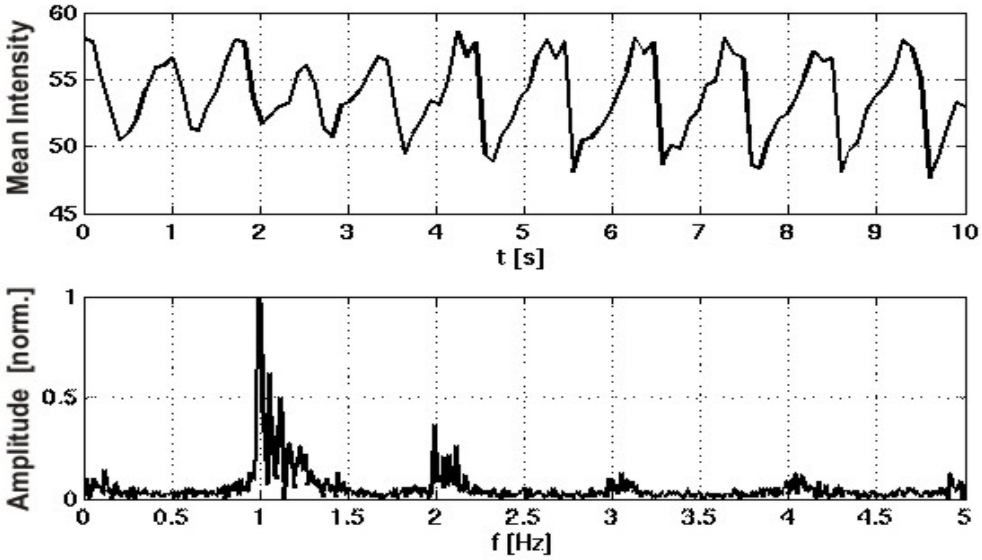

Figure 4.1: Time series of the averaged image intensity in an area of 10×10 pixels (top panel) and power spectrum of the data (bottom panel). The 1Hz oscillations are clearly seen in both the time series and the spectrum. The reaction parameters are T = 515K, $p_{o_2} = 1.5 \times 10^{-4}$ mbar, and $p_o = 7.5 \times 10^{-5}$ mbar.

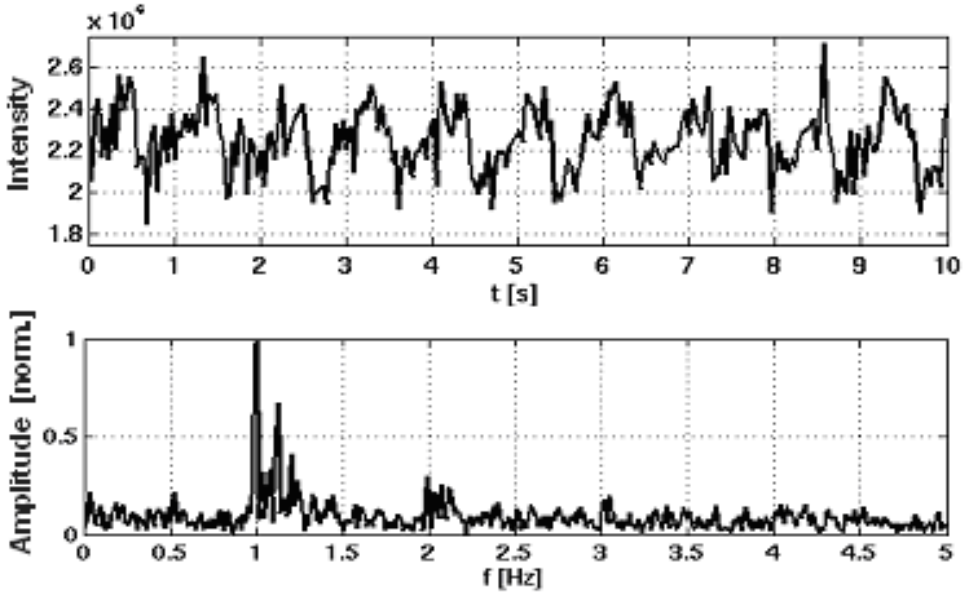

Figure 4.2: Time series of the gray value of one single pixel (top panel) and respective power spectrum (bottom panel). The reaction parameters are the same as in Fig. 4.1.

though the reaction parameters are kept constant (Fig. 4.3). This effect is presumably caused by a faceting of the platinum surface, which is known to take place at the used reaction conditions [99].

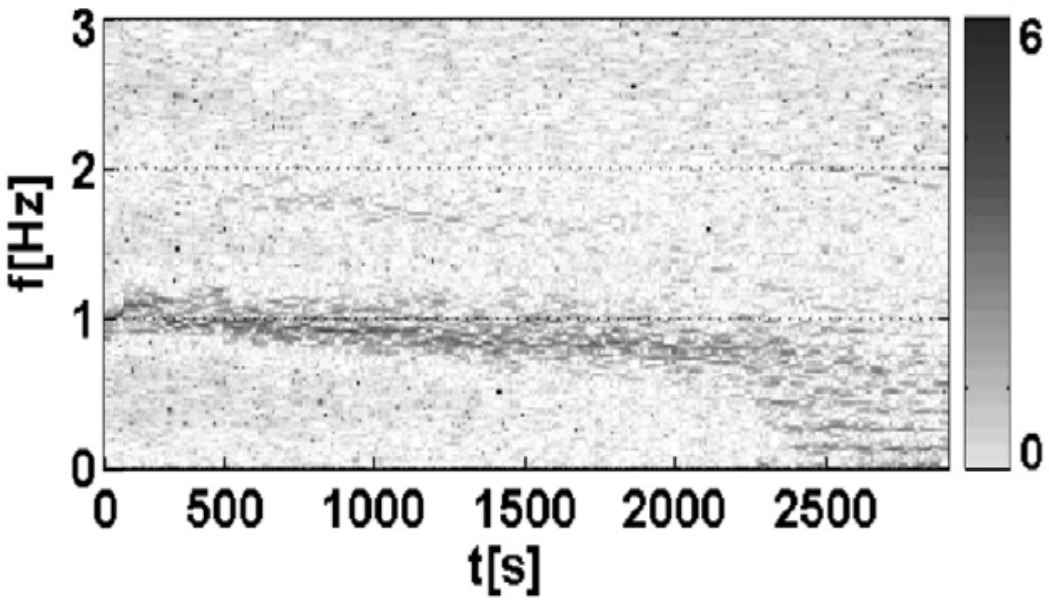

Figure 4.3: Fourier spectrogram showing the time evolution of the natural frequency of the system without forcing. For each time moment an interval of 20.48s (512 samples at 25 frames per second) is analyzed. The frequency has an initial value of about 1Hz. During the first 30 min it drops by approximately 0.2Hz. Broadening of the frequency line is also observed, which indicates, that the system has developed into a more turbulent state. Values of temperature (T = 515K), and partial pressures (p_{o_2} = 1.1×10^{-4} mbar, $p_o = 9.0 \times 10^{-5}$ mbar) were constant.

4.2 2:1 Forcing

The natural frequency of the system (ω_0) is taken after the full development of spiral wave turbulence. We apply the forcing $\omega_f = 2\omega_0$ in this system. After starting the forcing, the spiral wave turbulence is first replaced by the intermittent turbulence characterized by the repeated emergence and disappearance of localized turbulent

bubbles on a background of locked uniform oscillations. In different reaction and forcing parameters region, two types of clusters named phase and amplitude clusters were found.

4.2.1 Phase Clusters

Phase clusters are characterized by equal oscillation amplitudes and a constant phase shift between the cluster states. The oscillations in both cluster states correspond to the same limit cycle, but are opposite in phase. The phase fronts that separate different cluster domains exhibit rich behavior.

Fig. 4.4(a) shows the natural frequency of the system $\omega_0 = 0.68$Hz. The amplitudes of the Fourier coefficients are normalized to the maximum peak. We fixed the forcing frequency $\omega_f = 1.36$Hz and changed the forcing amplitude. During the experiment the reaction parameters were fixed.

At different forcing amplitudes two and four phase cluster patterns under 2:1 and 4:1 entrainment were found.

2:1 Entrainment

At forcing amplitude A = 0.22, a phase locked regime with stable cluster patterns due to 2:1 entrained was observed. Fig. 4.4(b) shows the Fourier spectrum of 2:1 entrained phase clusters and Fig. 4.5(a) shows three snapshots of PEEM images at time intervals of one forcing period between subsequent frames.

Due to the non-harmonicity of the CO oxidation, the size of these phase domains is not fixed but changes in time undergoing enlargement-reduction (breathing like) cycles with a periodicity that is again two times the forcing cycle.

The space-time plot (Fig. 4.5(b)) shows that the domain wall of the opposite phase is not stationary, taken along the line AB shown in Fig. 4.5(a). Fig. 4.5(c) gives the time course of the surface marked by the (solid line) AB in the first image of Fig. 4.5(a)

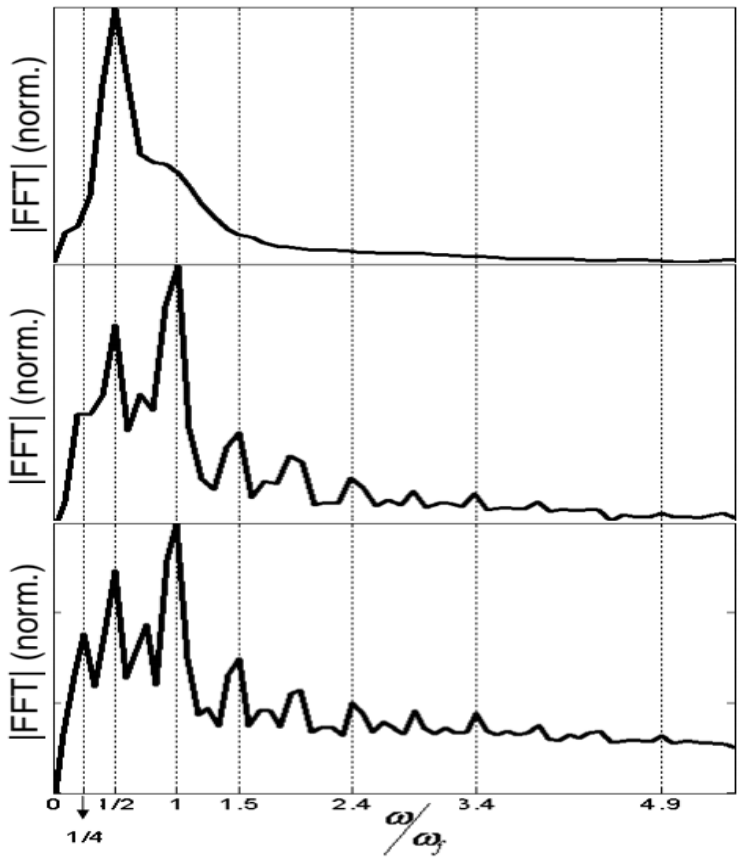

Figure 4.4: Mean Fourier spectra at different forcing amplitudes A. (a) 0, (b) 0.22, (c) 0.24. Other parameters are T = 529K, $p_{o_2} = 1 \times 10^{-4}$ mbar, $p_o = 9.26 \times 10^{-5}$ mbar, $\omega_0 = 0.68$Hz, and $\omega_f = 1.36$Hz.

and the course of the forcing signal (dotted line), shows the sub-harmonic entrainment of the system to the forcing frequency.

During two cycles of the forcing signal, the system performs one cycle of periodically changing CO coverage, indicated by low and high PEEM intensity.

To further analyze the dynamics of oscillatory clusters, the frequency demodulation technique (described detail in Chapter 3) was used which is useful for the characterization of resonant patterns. On analyzing the patterns at $\omega_f/2$, the two phase patterns differed by π were obtained.

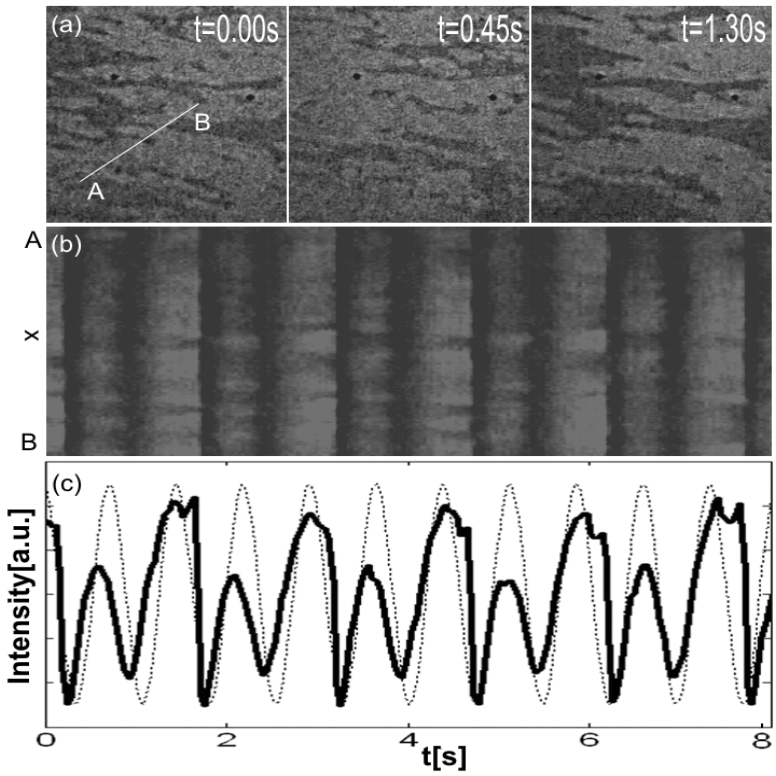

Figure 4.5: Phase cluster under 2:1 entrainment. (a) snapshots of PEEM images 300×300 μm^2 illustrating a phase locked regime, (b) space-time plot taken along the AB line (top panel), and (c) intensity of the PEEM image averaged globally (solid line) and the forcing signal (dotted line). The forcing amplitude A = 0.22 and other parameters are the same as in Fig. 4.4.

In phase pattern Fig. 4.6(a), two phase states are clearly visible. Fig. 4.6(b) illustrates that the oscillation amplitude is strongly reduced in the domain interfaces and that is the same within the domains of the opposite phase.

Phase portrait Fig. 4.6(c), shows two spots of accumulating points corresponding to the pixels located within the different domain. Phase histogram Fig. 4.6(d), corresponds to two phases which are differ by π. The two phase states are not evenly weighted.

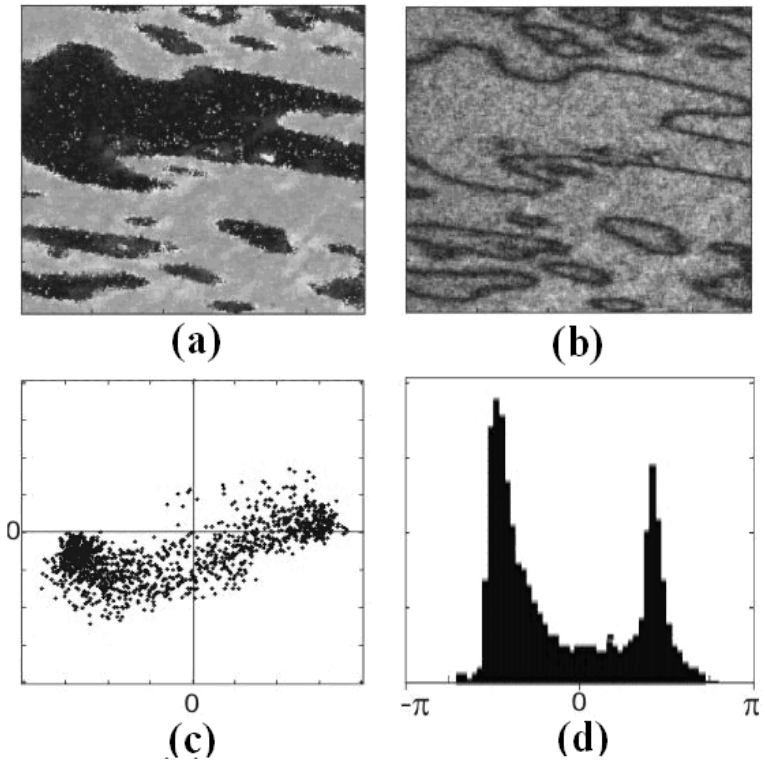

Figure 4.6: Phase and amplitude representation of the cluster patterns shown in Fig. 4.5(a). (a) phase pattern, (b) amplitude pattern, (c) phase portrait, and (d) phase histogram.

4:1 Entrainment

At forcing amplitude A = 0.24, two phase cluster patterns due to 4:1 entrainment were observed. Fig. 4.4(c) shows the Fourier spectrum under 4:1 entrainment and one can see the main sharp peak at $\omega_f/4$ and ω_f.

The phase and amplitude analysis of the cluster patterns at $\omega_f/4$ shows two phase cluster which differ by π have similar properties as 2:1 entrained cluster (data are not shown).

Four Phase Clusters under 4:1 Entrainment:

The experimental protocol is modified in a way that the system is brought back to

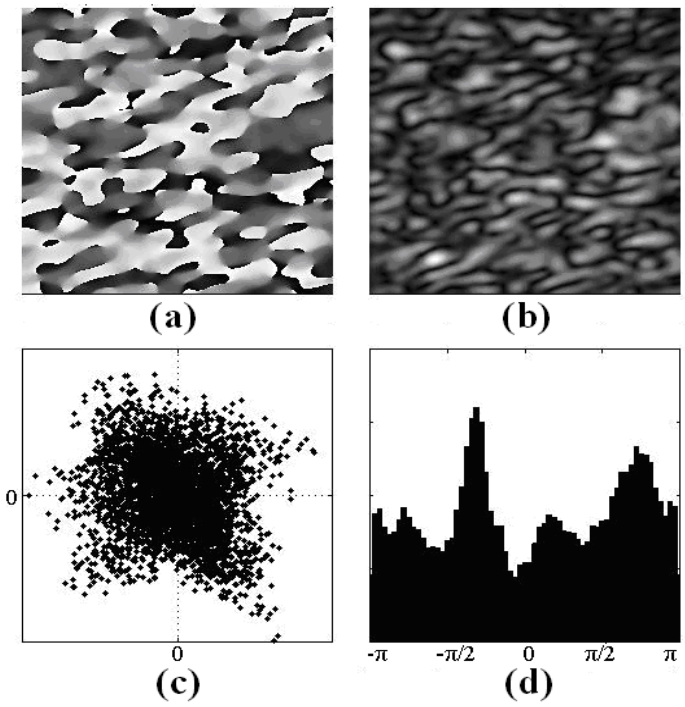

Figure 4.7: Phase and amplitude representation of the four phase cluster patterns. (a) phase pattern, (b) amplitude pattern, (c) phase portrait, and (d) phase histogram.The forcing amplitude A = 0.25 and other parameters are same as in Fig. 4.4.

the unforced state and is then forced with these differing initial conditions, four phase clusters could be obtained, in analogous to resonant 4:1 forcing. Fig. 4.7 shows the phase and amplitude representation, analyzed at $\omega_f/4$. (PEEM images are not shown.) The cluster patterns appears to be smaller scaled.

The phase portrait, given in Fig. 4.7(c), shows a cross-shaped structure rather than the line structure in the preceding images, indicating the presence of four distinct cluster states. This is confirmed by the phase histogram, shown in Fig. 4.7(d), where four maxima appear with a difference of $\pi/2$. However, two of the phase states, differing by π, are more predominant. This may indicate that the two phase cluster configuration might be more stable and the system tends to reach a two phase state.

4.2.2 Amplitude Clusters

In amplitude clusters, not only the oscillation phase but also the oscillation amplitude is different in the regions occupied by the two different states. Thus, uniform oscillations within two different clusters correspond to different coexisting limit cycles of an equal period. The phase shift between the oscillations in two cluster states is constant, but depends on the controlling parameters ω_f and A.

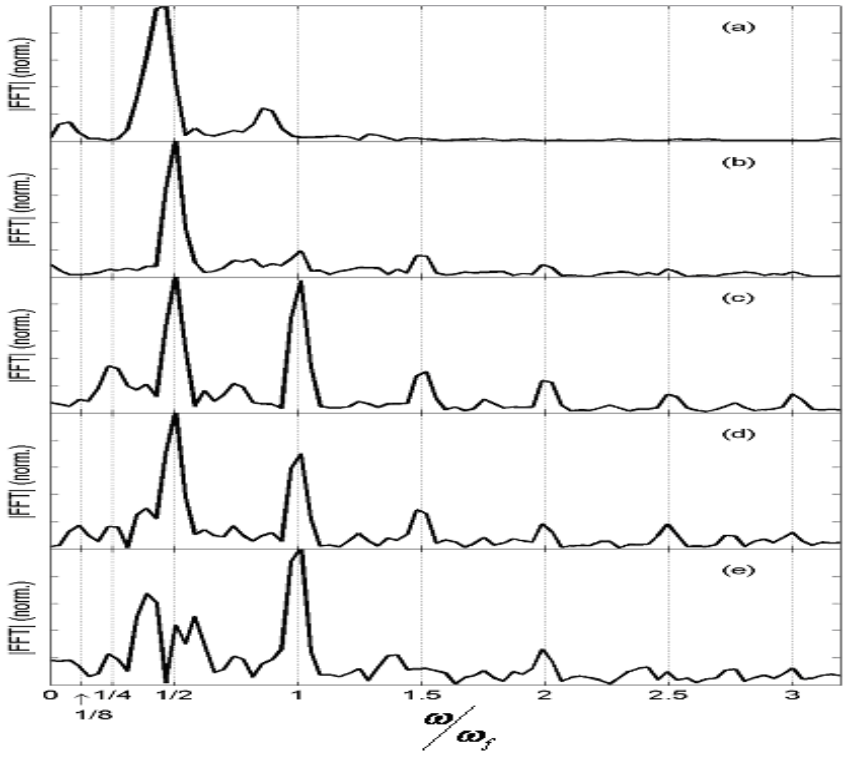

Figure 4.8: Mean Fourier spectra at different forcing amplitudes A. (a) 0, (b) 0.014, (c) 0.064, (d) 0.079, and (e) 0.093. Other parameters are T = 546 K, $p_{O_2} = 1.5 \times 10^{-4}$ mbar, $p_o = 6.22 \times 10^{-5}$ mbar, and $\omega_f = 1.27$Hz.

2:1 Entrainment

As above, forcing is applied after the full development of spiral wave turbulence. Fig. 4.8(a) shows the frequency spectrum of the unforced turbulent system. The natural

frequency, defined as the most prominent line, is found at $\omega_0 = (0.59 \pm 0.03)$Hz. The forcing frequency is set to $\omega_f = 1.27$Hz, which is slightly higher than twice the calculated natural frequency.

At A = 0.014, two phase frequency locked amplitude clusters were observed. It is locked to the external stimulus with a phase shift of one forcing period between the two states. Analysis of the phase and amplitude representation of amplitude cluster patterns at $\omega_f/2$ is shown in Fig. 4.9.

In phase pattern (Fig. 4.9(a)), two phase states are clearly visible and the amplitude pattern (Fig. 4.9(b)) indicates that the amplitude is different not only at the border of the cluster but also in different domains of the cluster pattern. The phase portrait Fig. 4.9(c) and histogram Fig. 4.9(d) shows the phase difference between two clusters is π.

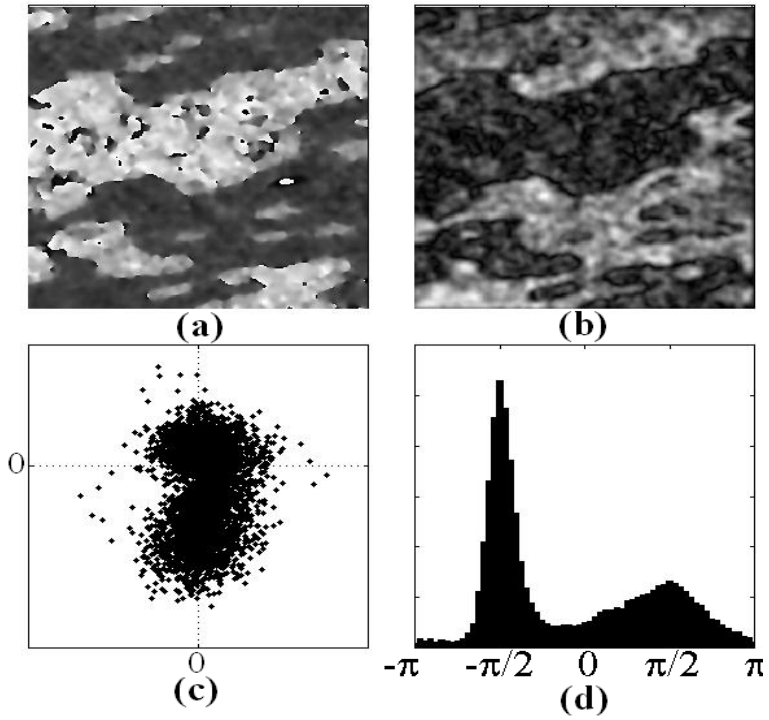

Figure 4.9: Phase and amplitude representation of amplitude clusters at 2:1 entrainment. (a) phase pattern, (b) amplitude pattern, (c) phase portrait, and (d) phase histogram.

4:1 Entrainment

At slightly stronger forcing amplitude A = 0.064, the system's oscillations are period doubled, indicated by the appearance of the sub-harmonic line $\omega = \omega_f/4$ and it's rational multiples $3/4\omega_f$, $5/3\omega_f$, as seen in Fig. 4.8(c). Two phase amplitude clusters were again observed.

The phase and amplitude representation of the amplitude clusters at $\omega_f/4$ shows the same properties as two phase cluster at 2:1 entrainment (data are not shown).

8:1 Entrainment

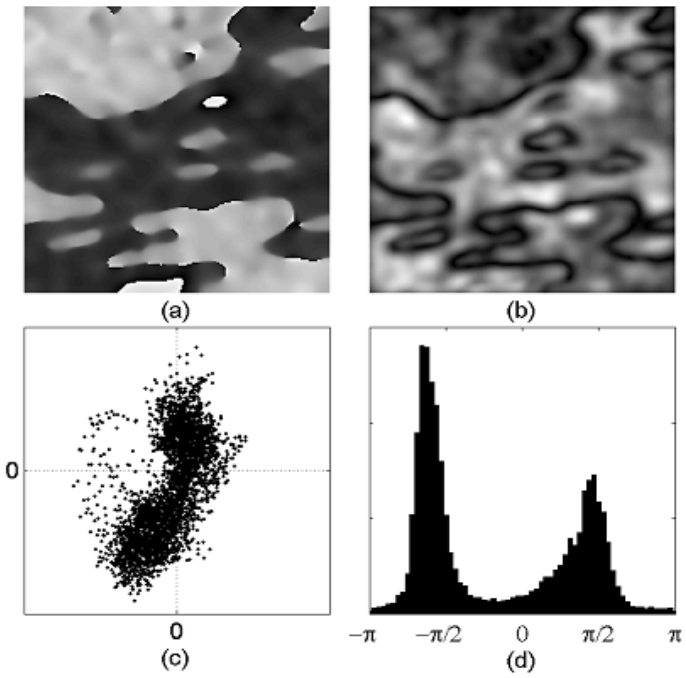

Figure 4.10: Phase and amplitude representation of the amplitude cluster patterns at 8:1 entrainment. (a) phase pattern, (b) amplitude pattern, (c) phase portrait, and (d) phase histogram.

A slight increase in the forcing amplitude to A = 0.0108 leads to the next bifurcation within the period doubling cascade. The system shows 8:1 entrainment, locking to

a frequency of $\omega_f/8$, while the Fourier coefficient of $\omega_f/4$ nearly vanishes, the sub-harmonic $3/8\omega_f$ is strongly pronounced as seen in Fig. 4.8(c))

In Fig. 4.10, the spatial amplitude, phase distribution, the phase portrait, and the phase histogram are shown, obtained for the Fourier coefficients of $\omega_f/8$. Fig. 4.10(a) shows the phase patterns, where two phase states are mainly observed. They appear in clusters, which are separated by low amplitude boundaries and the amplitude is different in two phase states as can be seen from the amplitude pattern in Fig. 4.10(b). The phase portrait, given in Fig. 4.10(c), is mainly line-shaped, with two accumulation points with opposite phase. The clustering into two phase states can clearly be seen in the phase histogram, given in Fig. 4.10(d).

Transition to Chaos

Finally, applying a slightly higher forcing amplitude of A = 0.093, the oscillation is no longer entrained. The Fourier spectrum given in Fig. 4.8(e), shows the absence of the sub-harmonic line at $\omega_f/8$. Lines at $\omega_f/4$, $\omega_f/2$, and ω_f are still present, but additional frequency components appear in the sub-harmonic regime.

The strong peak between $\omega_f/4$ and $\omega_f/2$ might be related to $3/8\omega_f$ within the frequency resolution, but the peak slightly above $\omega_f/2$ (determined to be at $\omega_f = (0.73 \pm 0.03)$Hz) cannot be assigned to a rational multiple of the forcing frequency. Therefore, we state a chaotic response of the system at sufficiently high forcing amplitude. Regarding the spatial dynamics, the entrainment of the system is accompanied by the suppression of chemical turbulence and cluster formation.

4.3 3:1 Forcing

Pattern formation under 3:1 resonance is explained in this section. Two phase, three phase, and six phase patterns were observed at 2:1, 3:1, and 6:1 entrainment respectively.

4.3.1 2:1 Entrainment

As above the system is forced with three times its natural frequency ($\omega_f = 3\omega_0$). The natural frequency of the system is found at about 0.76Hz. The forcing parameters were fixed at $\omega_f = 2.3$Hz and A = 0.12 and the phase locked regimes were observed (Fig. 4.11). As can be seen in the space-time plot (Fig. 4.11(b)), the system largely performs oscillations with a frequency of $\omega = \omega_f/2$ (2:1 entrainment). However, it seems that for this amplitude of 3:1 forcing the system is not fully entrained. At t = 5.5 s the pattern inverts in the space-time plot and a large amplitude oscillation is not followed by a small shoulder but by another large amplitude oscillation (Fig. 4.11(c)).

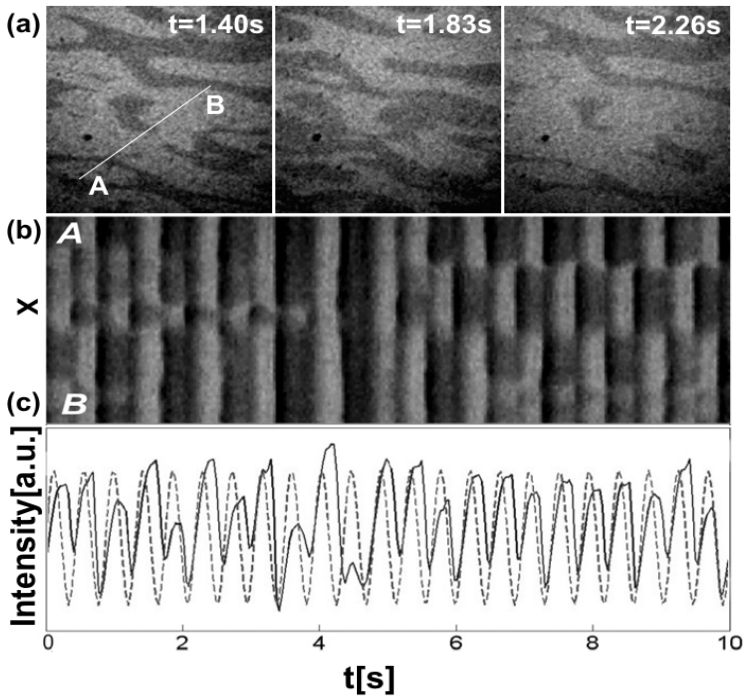

Figure 4.11: Two phase cluster due to 2:1 entrainment in 3:1 forcing. (a) snapshots of PEEM images (size $300 \times 300\ \mu m^2$), (b) space-time plot showing the pattern evolution along the AB line (see top panel), and (c) averaged intensity (solid line), and the forcing signal (dotted line). The reaction parameters are: T = 534 K, $p_{o_2} = 1.6 \times 10^{-4}$ mbar, $p_o = 7.6 \times 10^{-5}$ mbar, $\omega_o = 0.76$Hz, and the forcing parameters are A = 0.11, and $\omega_f = 2.3$Hz.

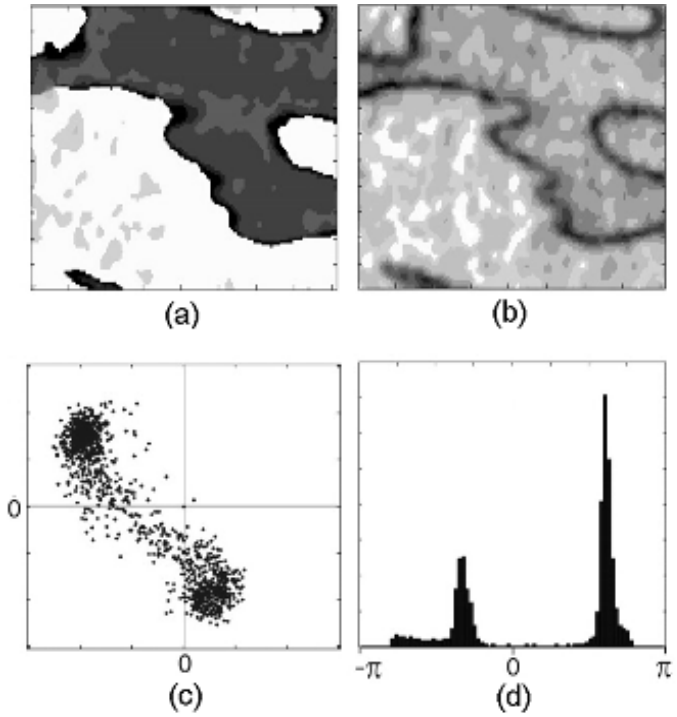

Figure 4.12: Phase and amplitude representation of the cluster patterns shown in Fig. 4.11(a). (a) phase pattern, (b) amplitude pattern, (c) phase portrait, and (d) phase histogram.

After this transition, the oscillations of the system are again 2:1 entrained. These more complex dynamics are also visible when phase and amplitude of the patterns are analyzed (Fig. 4.12). Two distinct clusters with sharp boundaries can be observed (Fig. 4.12(a)). The two phase locked cluster having different amplitude in different domains indicate the observation of an amplitude cluster (Fig. 4.12(a)), which are not exactly separated by a phase difference of π (Fig. 4.12(c) and (d)).

4.3.2 3:1 Entrainment

Another experiment begins with spiral wave turbulence, and without forcing the system oscillates with a natural frequency $\omega_0 = 0.8$Hz (Fig. 4.13(a)). The forcing frequency is set to $\omega_f = 2.4$Hz, which again is three times of the calculated natural

frequency. At forcing amplitude A = 0.12, the system oscillates with one third of the forcing frequency, and the system frequency locked in 3:1 entrainment. Fig. 4.13(b) shows the Fourier spectrum at 3:1 entrainment, where one can see the peak at ω_f and $\omega_f/3$.

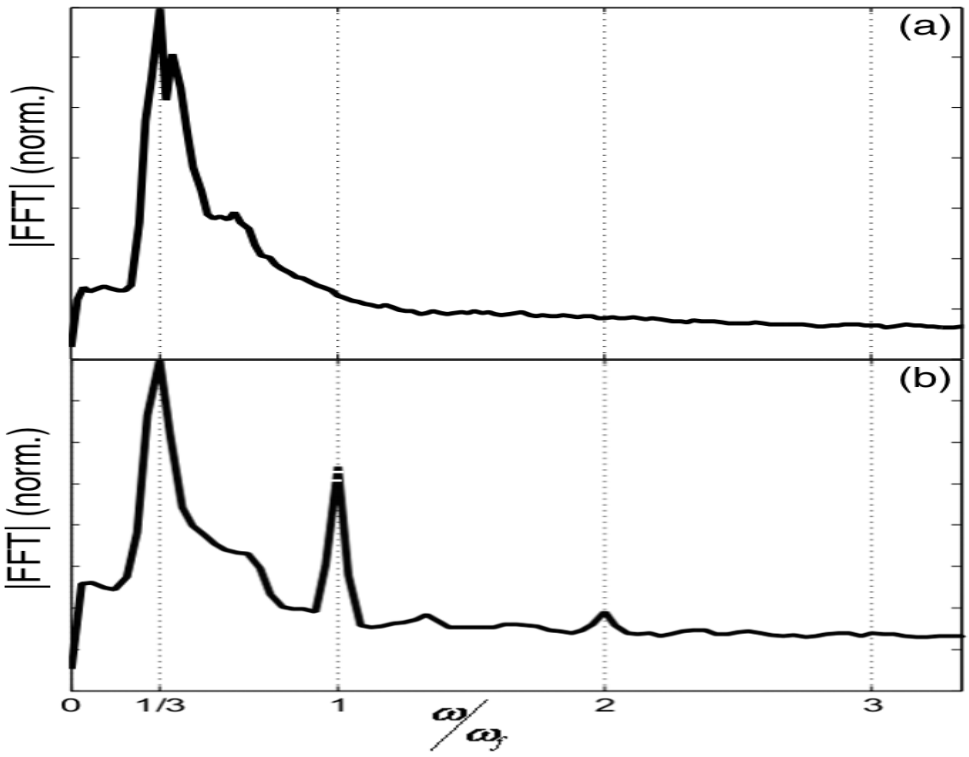

Figure 4.13: Fourier spectra at different forcing amplitudes A: (a) 0, and (b) 0.12. The reaction parameters are: T = 534 K, $p_{o_2} = 1.6 \times 10^{-4}$ mbar, $p_o = 7.66 \times 10^{-5}$ mbar, $\omega_o = 0.8$Hz, and $\omega_f = 2.4$Hz.

Fig. 4.14(a) shows the snapshots of stripe like wave fronts that periodically appear on the platinum surface under 3:1 entrainment. Every PEEM image is taken after one forcing period. The temporal evolution of the system is represented as a space-time plot in Fig. 4.14(b) taken along the AB shown in Fig 4.14(a).

In space-time plot one can see that the domain of opposite phase is not stationary. Fig. 4.14(c) gives the time course of the surface along the line AB shown in the first

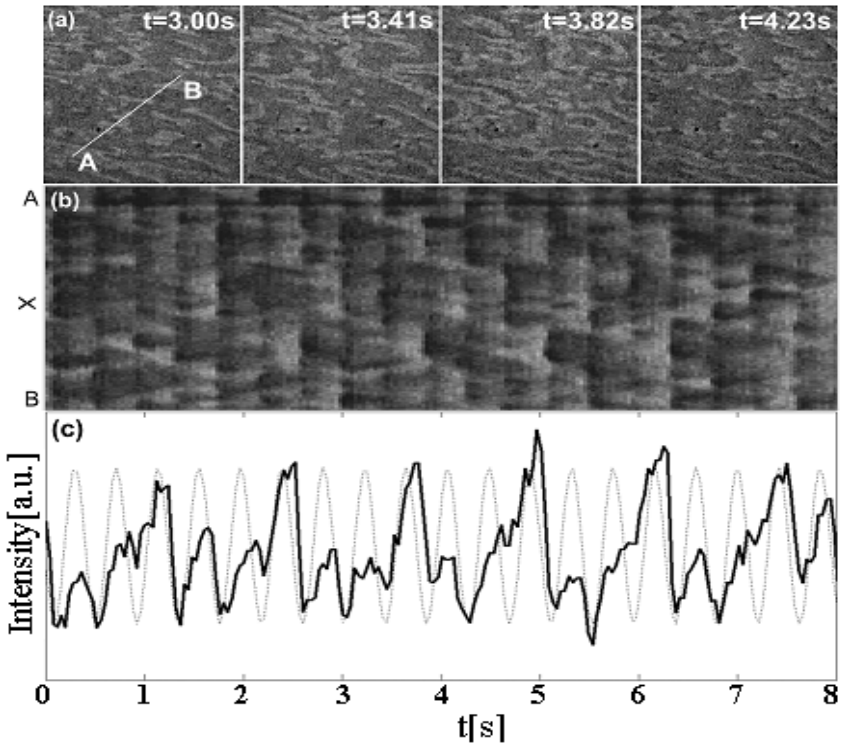

Figure 4.14: Three phase cluster formation and entrainment at 3:1 resonant forcing. (a) snapshots of PEEM images (size 300 × 300 μm^2), (b) space-time plot showing the pattern evolution along the AB line indicated in first image (top panel), and (c) averaged intensity (solid line) and the forcing signal (dotted line). The reaction parameters are: T = 534 K, $p_{o_2} = 1.6 \times 10^{-4}$ mbar, $p_o = 7.66 \times 10^{-5}$ mbar, ω_o = 0.8Hz, and the forcing parameters are A= 0.12, and ω_f = 2.4Hz.

image of Fig. 4.14(a) (solid line) and the course of the forcing signal (dotted line), shows the sub-harmonic entrainment of the system to the forcing frequency.

Fig. 4.15 shows the phase and amplitude representation at $\omega_f/3$. Well-defined phase fronts such as black, dark gray, and light gray areas are visible in phase pattern in Fig. 4.15(a). The amplitude pattern in Fig. 4.15(b) shows that the amplitude is approximately the same except for the border. Accordingly, the phase distribution, given in Fig. 4.15(c) and Fig. 4.15(d), shows three maxima with a distance of $2\pi/3$.

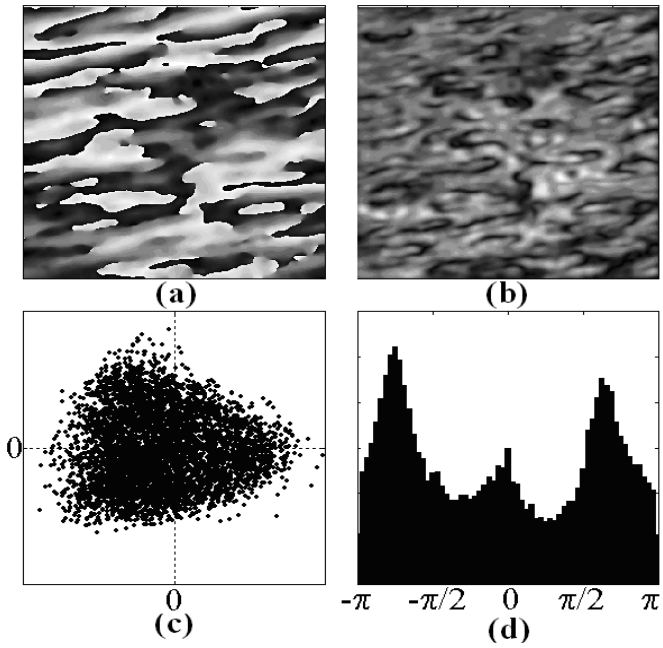

Figure 4.15: Phase and amplitude representation of the cluster patterns shown in Fig. 4.14(a). (a) phase pattern, (b) amplitude pattern, (c) phase portrait, and (d) phase histogram.

4.3.3 6:1 Entrainment

At forcing frequency $\omega_f = 2.5$Hz, a response with large spectral power at $\omega/\omega_f = 1/6$ was observed as shown in the power spectrum Fig. 4.16. The power spectrum shows the main peak at $\omega_f/6$, $\omega_f/3$, ω_f, $1.95\omega_f$.

The phase and amplitude representation at $\omega_f/6$ is shown in Fig. 4.17. In phase pattern the six phases are clearly visible (Fig 4.17(a)). In the amplitude pattern (Fig 4.17(b)), the amplitude drops only at the border. The phase portrait (Fig 4.17(c)) shows the six fold symmetry corresponding to six stable uniform phases, which are found at the point farthest from the center. The states are connected with traveling fronts that shift the phase by $\pi/3$ and do not go through the origin. The scattering of the point is due to the experimental noise. The phase histogram (Fig. 4.17(d)) shows that the phase difference in each phase is approximately $2\pi/6$.

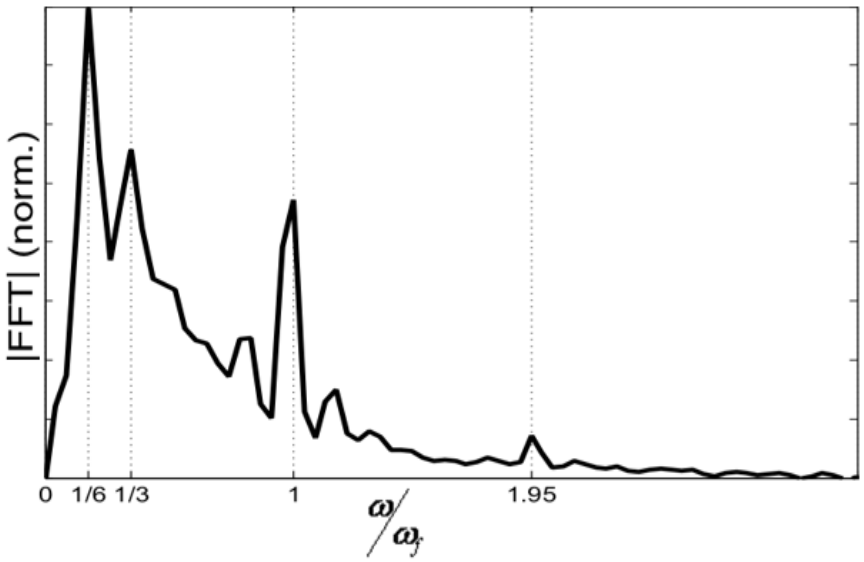

Figure 4.16: Spatially averaged Fourier spectrum of the PEEM intensity at $\omega_f = 2.5$Hz. Other parameters are same as in Fig. 4.15.

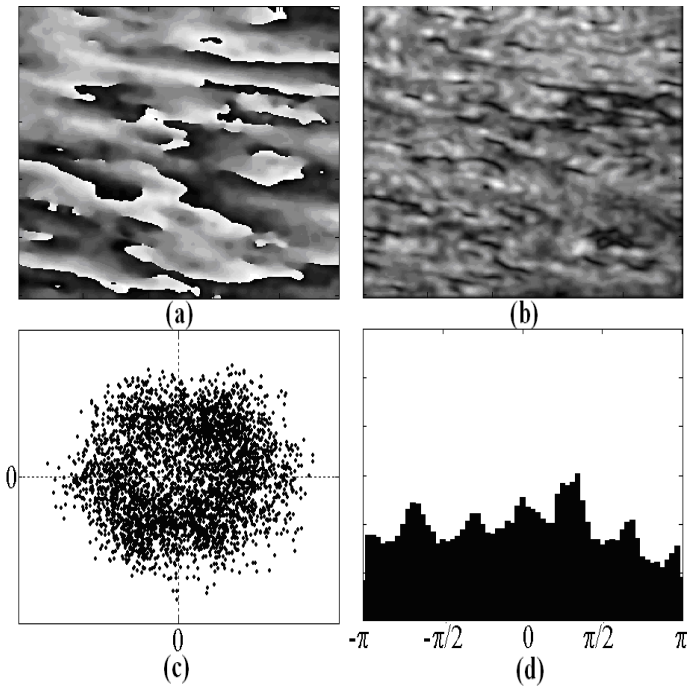

Figure 4.17: Phase and amplitude representation of the cluster patterns at 6:1 entrainment. (a) phase pattern, (b) amplitude pattern, (c) phase portrait, and (d) phase histogram.

4.4 4:1 Forcing

In this section we explore pattern formation of the forced CO oxidation on Pt(110) under 4:1 resonance in turbulent and nonturbulent regimes. Recent developments enable the exploration of a wider range of forcing parameters, allowing frequencies of about four times the natural frequency of the oscillatory system to be reached for the first time.

4.4.1 4:1 Forcing in Turbulent Regime

Like above, the natural frequency of the system was measured after the full development of the spiral wave turbulence. The natural frequency of the system is about 0.72Hz (see in Fig. 4.18(a)). At forcing amplitude of A = 0.068, the spiral-wave turbulence develops into stripe like wave fronts that periodically appear on the platinum surface (see Fig. 4.19(a) and 4.19(b)). Fig. 4.19(c), which gives the time course of the surface marked by the square in the first image of Fig. 4.19(a) (solid line) and the course of the forcing signal (dotted line), shows the sub-harmonic entrainment of the system to the forcing frequency.

During four cycles of the forcing signal, the system performs one cycle of periodically changing CO coverage. While small changes within the PEEM signal occur at all phases of the forcing frequency, the sudden increase of the CO coverage is in phase with the rising edge of the applied CO pressure.

The same could be observed for the strong decrease of the CO coverage occurring in accordance with every fourth trailing edge of the forcing signal. The moment of high and low CO coverage occurs at different phases of the sub-harmonic oscillation for different places on the surface. It can best be seen in the space-time plot, given in Fig. 4.19(b). It shows the intensity along the line indicated in the first image of Fig. 4.19(a). Spatially resolved analysis of the appearing pattern using the demodulation technique shows phase clusters (see Fig. 4.20(a)). Along with a notable amount of phase defects indicating that the system is still turbulent, especially in the upper right area and the lower part of the analyzed surface, a regular four-phase pattern can be

observed.

The different phase states are visible in the phase pattern in Fig. 4.20(a) as black, dark-gray, gray, and light-gray areas. These areas also show higher oscillation amplitude, given as bright areas in Fig. 4.20(b), while the domain interfaces are visible as regions with reduced amplitude, shown in gray. The regions with strongly reduced amplitude near zero, seen in black, are located at the defect points.

The two areas of high amplitude and regular phase pattern are separated by a turbulent regime, where the number of defects is larger and phase clusters cannot be identified. The phase portrait and the phase histogram, given in Fig. 4.20(c) and Fig. 4.20(d), show the presence of four distinct phase states with a phase difference of $\pi/2$, accompanied by an underlying random phase distribution due to the turbulent regime.

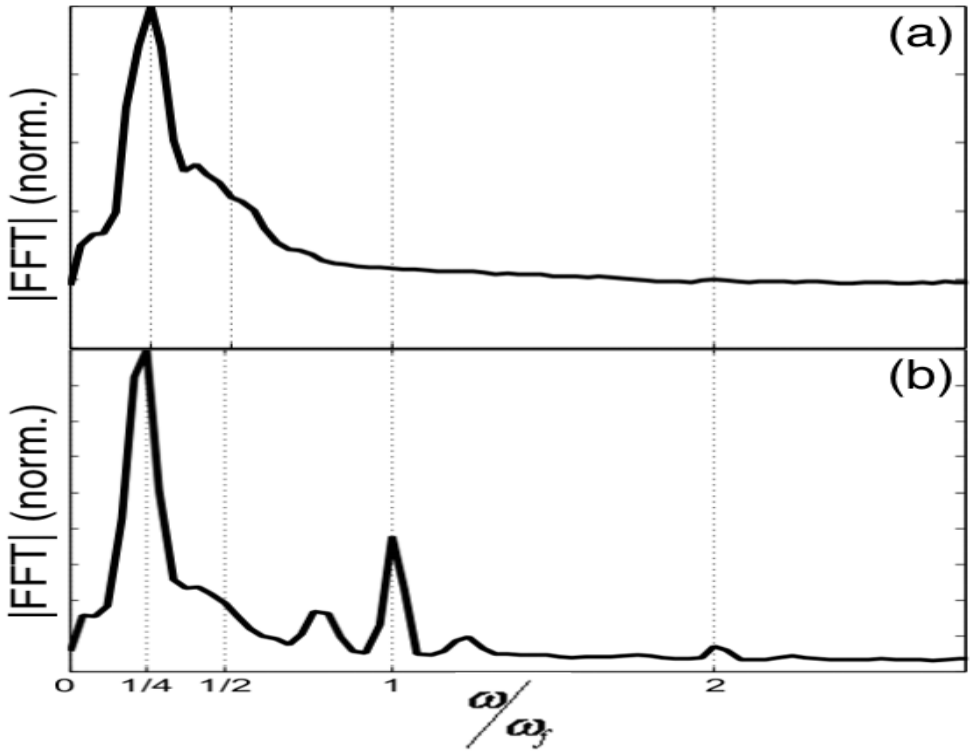

Figure 4.18: Fourier spectra at different forcing amplitudes A. (a) 0, (b) 0.068. The reaction parameters are: T = 534 K, $p_{o_2} = 1.7 \times 10^{-4}$ mbar, $p_o = 5.88 \times 10^{-5}$ mbar, $\omega_o = 0.72$Hz, and $\omega_f = 2.88$Hz.

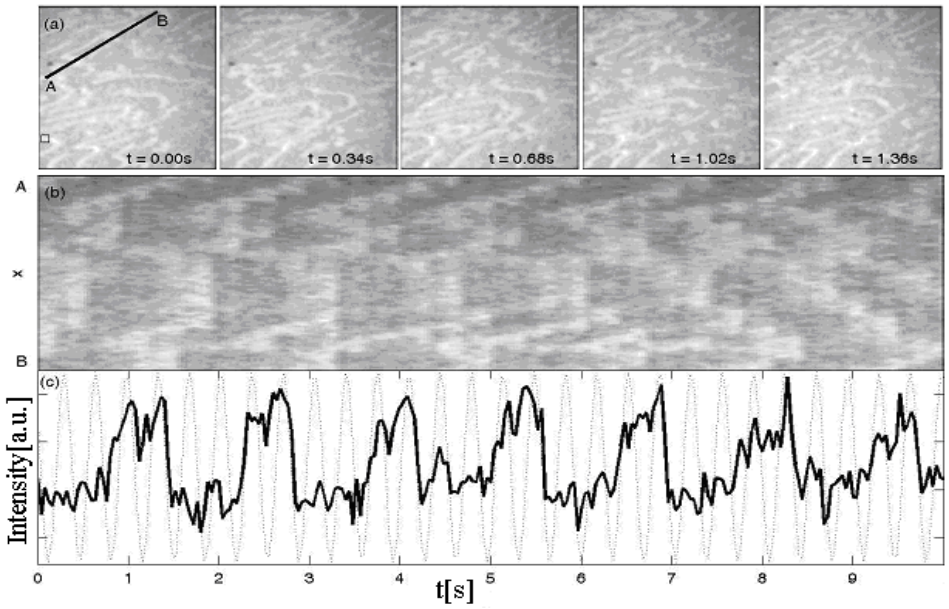

Figure 4.19: Four phase cluster at 4:1 resonant forcing. (a) snapshots of PEEM images (size $300 \times 300\ \mu m^2$), (b) space-time plot, and (c) averaged intensity of a local area of the surface (solid line), indicated by the square in (a), and the forcing signal (dotted line). The reaction parameters are the same as in Fig. 4.18.

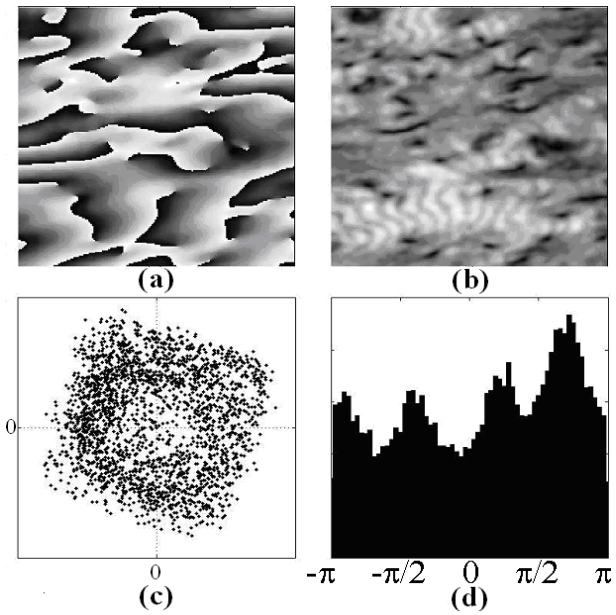

Figure 4.20: Phase and amplitude representations of the cluster patterns shown in Fig. 4.19(a). (a) phase pattern, (b) amplitude pattern, (c) phase portrait, and (d) phase histogram.

4.4.2 4:1 Forcing in a Nonturbulent Regime

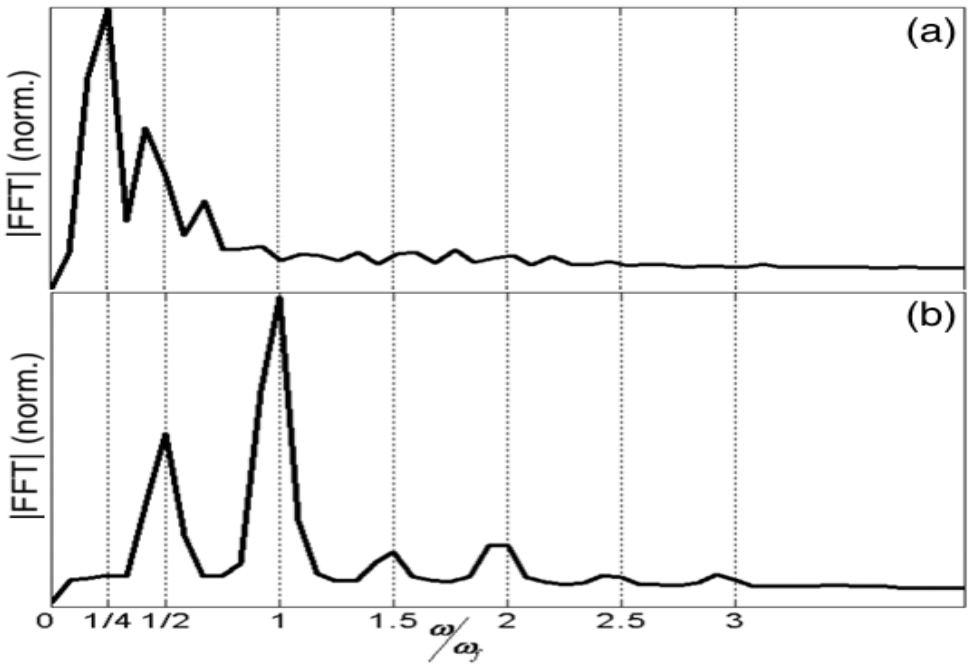

Figure 4.21: Fourier spectra at different forcing amplitudes A. (a) 0, and (b) 0.12. The parameters are: T = 534 K, $p_{o_2} = 1.2 \times 10^{-4}$ mbar, $p_o = 5.8 \times 10^{-5}$ mbar, $\omega_o =$ 0.5Hz, and $\omega_f = 2$Hz.

4:1 forcing is done experimentally in a nonturbulent regime in the ruthenium-catalyzed BZ reaction forced by periodic illumination revealed, where the unforced pattern is a rotating spiral wave of ruthenium catalyst concentration. However, four phase patterns at low forcing amplitude were seen but the two phase standing wave patterns at high forcing amplitude were not seen.

The system was forced after the full development of homogenous oscillation. Fig. 4.21(a) shows the natural frequency of the system around 0.5Hz. The system was forced around four times its natural frequency.

At weak forcing amplitude A = 0.11, the system oscillates with half of the forcing frequency; the system is frequency locked in 2:1 entrainment (see Fig. 4.21(b)). Fig. 4.22(a) shows the PEEM images of the phase clusters taken after one forcing period.

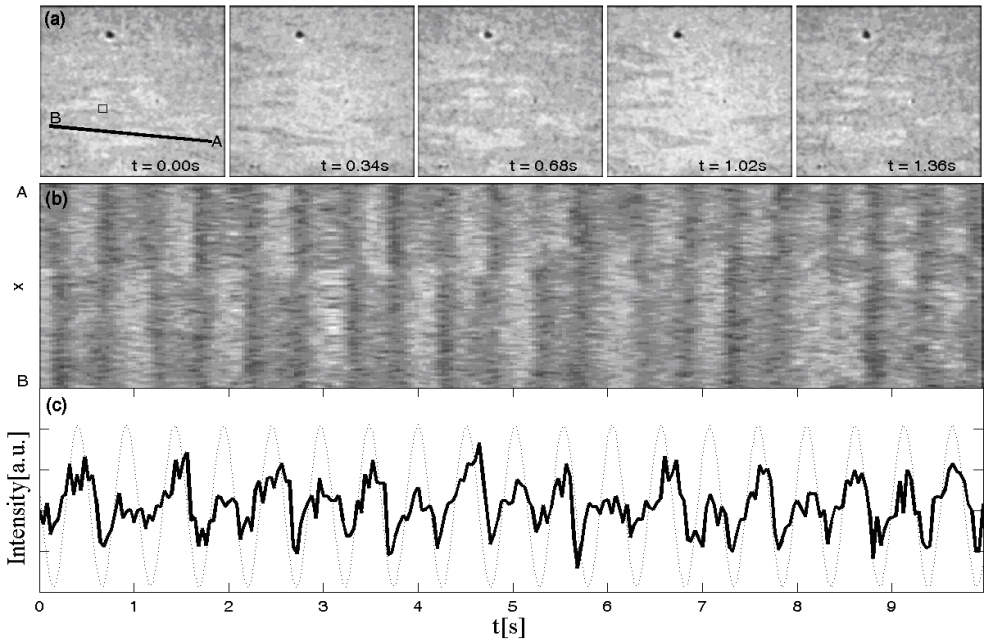

Figure 4.22: Two phase cluster formation and 2:1 entrainment at 4:1 resonant forcing. (a) snapshots of PEEM images (size 300×300 μm^2), (b) space-time plot showing the pattern evolution along the AB line indicated in (a), and (c) averaged intensity of a local area of the surface (solid line) and the forcing signal (dotted line). The parameters are: T= 534 K, $p_{o_2} = 1.2 \times 10^{-4}$ mbar, $p_o = 5.8 \times 10^{-5}$ mbar, $\omega_o = 0.5$Hz, $\omega_f = 2$Hz, A = 0.12.

The space-time plot represents (Fig. 4.22(b)) that the domain of the opposite phase are not stationary, taken along the line AB shown in Fig. 4.22(a). In Fig. 4.22(c) the solid line shows the average PEEM intensity and the dotted line shows the forcing signal of the system.

To get an idea about phase and amplitude frequency demodulation technique is used again. Fig. 4.23 shows the phase and amplitude representation of two phase clusters. In Fig. 4.23(b) one can see that the amplitude drops only at the border of the cluster and it is the same between the opposite domains Fig. 4.23(a). Fig. 4.23(c) and Fig. 4.23(d) represent that the phase difference is π.

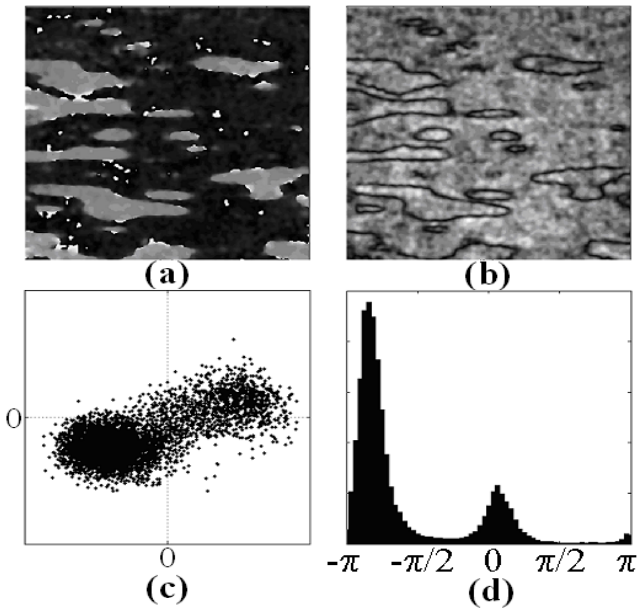

Figure 4.23: Phase and amplitude representations of the cluster patterns shown in Fig. 4.22(a). (a) phase pattern, (b) amplitude pattern, (c) phase portrait, and (d) phase histogram.

4.5 Conclusion

Resonance forcing is investigated in turbulent and nonturbulent regimes in CO oxidation on Pt(110). A compressor driven reactor which allows global gas-phase forcing for frequency modulations up to 4Hz was designed and built [80]. Experiments in different resonant forcing regimes (2:1, 3:1, 4:1) were performed and the observed pattern formation is discussed with respect to experimental studies.

In the case of 2:1 resonance forcing, a complete path from chemical turbulence to entrainment and further to chaotic oscillations via a period doubling cascade was obtained. A variety of patterns were observed under 2:1 forcing. Under 2:1 and 4:1 entrainment both types of cluster (phase and amplitude) differing by π were obtained. Four phase clusters are obtained under 4:1 entrainment. In the case of 8:1 sub-harmonic entrainment, only an amplitude clusters were obtained. Phase fronts separating different homogeneous phase locked states were clearly observed during the

experiments. In addition, the theoretical work under 2:1 resonance forcing in a single oscillator predicts [45] front explosions for decaying forcing amplitude, turbulent interfacial zones were not observed under 2:1 resonance forcing.

In 3:1 resonance forcing, three phase and six phase moving clusters were observed at 3:1 and 6:1 entrainment, while in BZ reaction three phase moving and six phase stationary clusters were observed respectively [77].

Theoretically predicted labyrinth patterns in a single oscillator [45], could not be found experimentally probably due to the high sensitivity of the system to parameter changes and present technical limitations in the application of soft changes in amplitude A.

Under 4:1 resonance forcing, 4:1 entrainment and four-phase cluster patterns could be observed [126]. However, the cluster formation takes place in finite regions of the surface, while other parts appear not to be 4:1 entrained, but still show turbulent behavior. This is one of the reasons why global coupling [46, 127] can be neglected under 4:1 forcing. Global coupling can stabilize homogeneous oscillations in a large surface area. This system, however, breaks up into a large number of rather small clusters. Thus, the effect of global coupling is averaged out. Additionally, the applied forcing amplitudes are comparably high, making an influence of global coupling even more unlikely.

In the case of 4:1 resonance forcing in a nonturbulent regime, only two phase moving phase clusters differing by π were obtained, while the four phase patterns could not be observed. Experimentally in BZ reaction in nonturbulent regime the four phase cluster patterns could be observed but the two phase standing wave patterns (predicted in CGLE equation, FitzHugh-Nagumo and Brusselator models) were not observed [71].

In summary, it was demonstrated that attempts to control chemical turbulence by periodic forcing may suppress spatial turbulence, but could lead to chaotic response of the system. The path to chaos was given by a periodic doubling cascade which was followed by the subsequent increase of forcing amplitude. Further with the help of a new compressor (described in Chapter 3) 3:1 and 4:1 resonance forcing regions were reached for first time.

Chapter 5

Resonance Forcing: Theoretical Results

Numerical simulations have been performed for comparison to the experiments. The KEE model was used and its implementation for resonance forcing is explained in Chapter 3.

Periodic forcing under 2:1 and 3:1 is explained by Davidson *et. al.* in a single oscillator [45] but this is unknown in an extended system. As the experimental system used an extended system, to compare the results the simulation was performed in an extended system.

5.1 Natural Frequency of an Extended System

As has been already discussed, the natural frequency of the single oscillator in nonturbulent state is identical with the oscillation frequency of the extended system, while

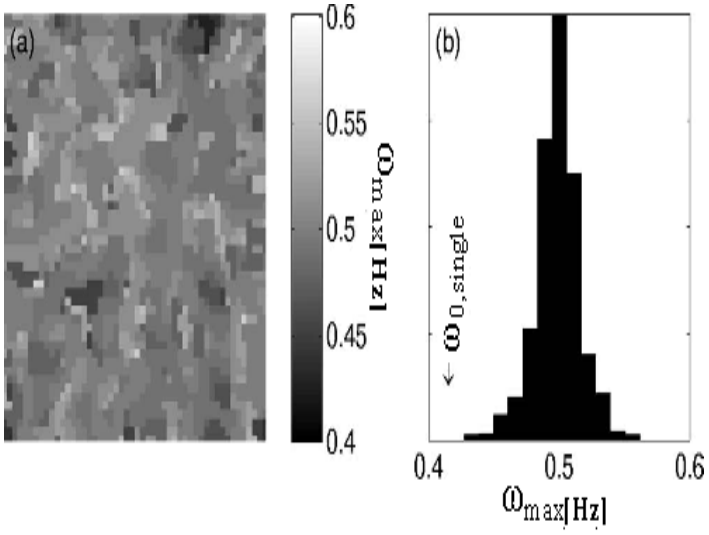

Figure 5.1: Frequency of an extended system. (a) spatial distribution, (b) histogram of most prominent frequency in a numerical simulation of unforced turbulence. $\omega_{0,single}$ denotes the natural frequency of a single oscillator. The parameters are given in Chapter 3, Table 3.1.

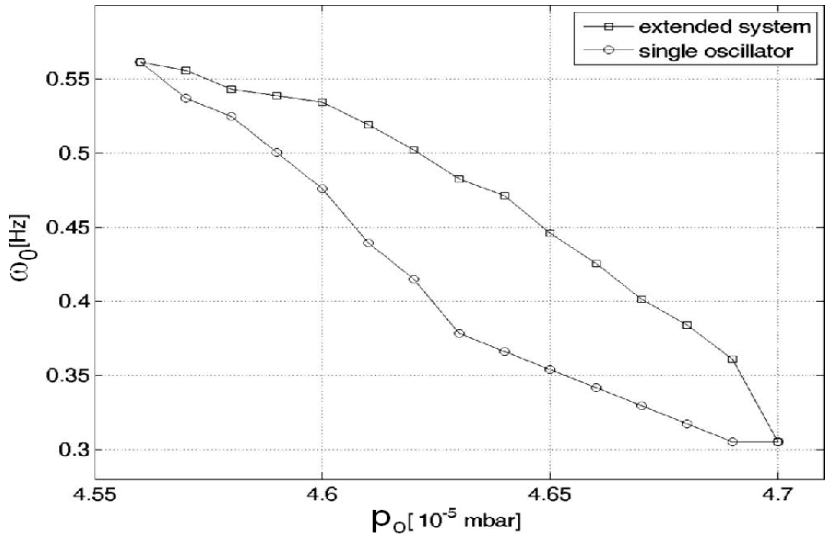

Figure 5.2: Oscillation frequency of a single oscillator (circles) and mean oscillation frequency of the extended system (squares) using the KEE model with different p_0 within the turbulent regime. The end points, where both frequencies coincide, indicate the onset of homogeneous oscillations.

in the turbulent state the system oscillates at higher frequencies due to diffusive interaction of the surface elements.

To get an overview over the oscillatory characteristics of an extended system, we performed Fourier analysis of the free running system in a fully developed turbulent state. The initial parameters of the partial pressures were chosen such that the unforced system oscillates and exhibits spontaneously spiral wave turbulence. The model parameters are given in Chapter 3 in Table 3.1.

Fig. 5.1(a) shows the most prominent frequency for each surface element. The local generic frequency variation spans a frequency range of about 0.4-0.6Hz. A certain frequency range is expected because of the turbulent state, but the distribution of oscillation frequencies found locally, shown as histogram in Fig. 5.1(b), shows that the mean frequency of 0.51Hz is remarkably higher than the oscillation frequency of the single oscillator, which is rarely found in the extended system.

Fig. 5.2 shows the course of both characteristic frequencies, the mean frequency of the extended system (squares) and the natural frequency of the single oscillator (circles), with increasing CO base pressure p_0. At the borders of the turbulent regime, homogeneous oscillations are found in the extended system, where the system behaves as a single oscillator. A maximum frequency difference of more than 0.1Hz appears in the center of the turbulent regime, at $p_0 = 4.63 \times 10^{-5}$ mbar. Defining the characteristic frequency of the extended system ω_0, extended as the mean local oscillation frequency, it was obtained for the chosen parameter set $\omega_{o,ext} = 0.51\text{Hz} \approx 1.2\omega_{0,single.}$

5.2 2:1 Forcing

The forcing frequency $\omega_f = 0.98$Hz was chosen to be near the second harmonic of the most prominent frequency in the extended system in fully developed turbulence ($\omega_{0,ext}$ = 0.51Hz) (Fig. 5.1(b)), rather than twice the single oscillator's natural frequency ($\omega_{0,single}$ = 0.42Hz).

Increasing the forcing amplitude, frequency locked 2:1 entrainment is obtained at A = 0.0078 (Fig. 5.3(a)). In the space-time plot (Fig. 5.3(b)), one can see that the domain

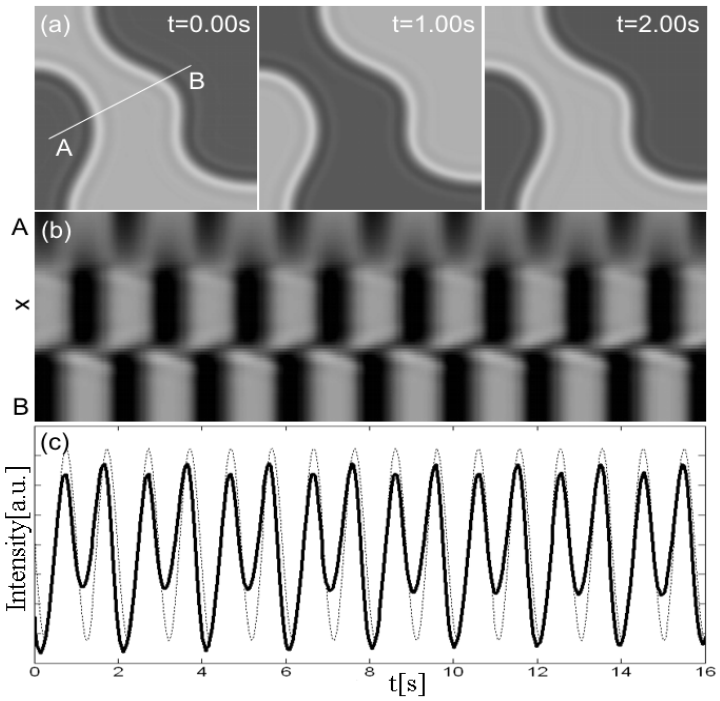

Figure 5.3: Two phase cluster at 2:1entrainment, KEE model. (a) Snapshots of CO coverage (size $400 \times 400\ \mu m^2$), (b) space-time plot along the AB line from Fig. 5.3(a), and (c) CO coverage along the line AB (solid line) and forcing signal (dotted line). Forcing parameters are $\omega_f = 0.98$Hz and A = 0.086.

between opposite phases are stationary.

It can be seen clearly in the space-time stroboscopic plot (Fig. 5.4), showing the pattern evolution along the same AB line of Fig. 5.3(a), choosing one frame every two forcing cycles. Non-equilibrium Bloch walls were observed as the borders between two different entrained states (π-fronts).

The phase and amplitude presentations are shown in Fig. 5.5. In phase pattern (Fig. 5.5(a)), the two phase states of black and dark gray are clearly visible. The amplitude is the same in the different domain except the cluster boundary (as seen in the amplitude pattern (in Fig. 5.5(b)). The phase difference between the two phase cluster is π, shown in the phase portrait (Fig. 5.5(c)) and phase histogram (Fig. 5.5(d)), respectively. The existence of two stable entrained states differing by a phase

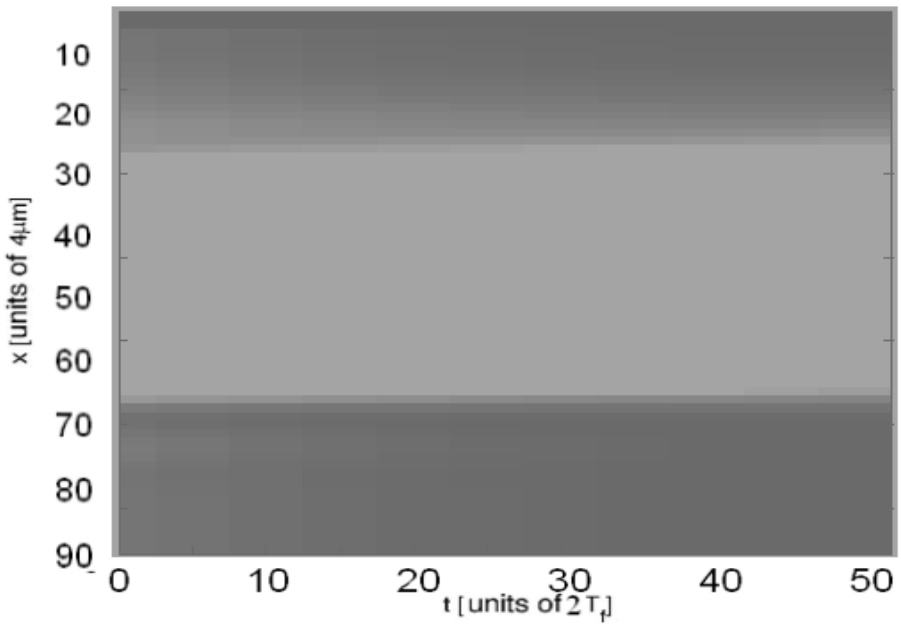

Figure 5.4: Stroboscopic space-time plot showing the pattern evolution along the line AB shown in Fig. 5.3(a), choosing one frame every two forcing cycle.

shift of π is a property of the 2:1 resonance, distinguishing it from the 1:1 resonance regime [128].

Period doubling to 4:1 entrainment takes place at A = 0.0102. A further period doubling to 8:1 entrainment could be found at A = 0.0108, leading to chaotic oscillations, similar to the experimental results (explained in section 4.2.2).

At the higher forcing amplitude A = 0.06, the chaotic regime is confined by an inverse period doubling cascade to final 1:1 entrainment. The phase and amplitude representation of 4:1 and 8:1 entrained data always exhibit phase clusters which differ by π or $\pi/2$ (data are not shown). An overview over the sub-harmonic frequency spectrum for increasing forcing amplitude is given in Fig. 5.6.

At 8:1 entrainment, the labyrinthine patterns were found. An example is given in Fig. 5.7(c). The transition between two phase cluster states and the labyrinthine pattern is induced by phase instabilities within the cluster boundary. However, transition times

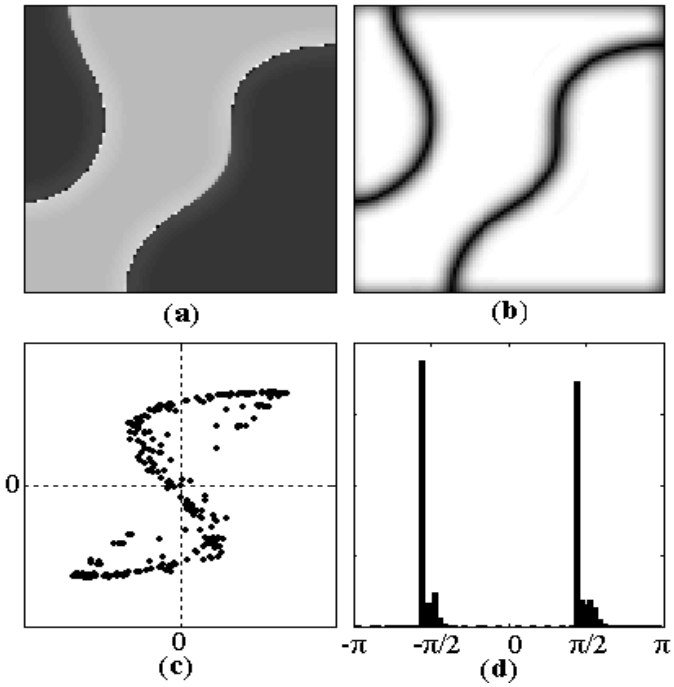

Figure 5.5: Phase and amplitude representation of the cluster patterns shown in Fig. 5.3(a). (a) phase pattern, (b) amplitude pattern, (c) phase portrait, and (d) phase histogram.

are longer than 300s and might not be fully covered within the experiment. In the chaotic regime, where the oscillation is not entrained to the forcing signal, chemical turbulence is nevertheless suppressed. Global coupling induced by the forcing is assumed to lead to low-dimensional chaos, where the system is spatially correlated. Cluster formations were observed similar to a 4:1 entrainment (see Fig. 5.7(b)), although phase fluctuation within the clusters were observed (see Fig. 5.7(d)).

The spatial correlation is determined by the cross-correlation of the dynamics at 100 evenly distributed surface locations, averaged over their distance. The results for unforced and forced spatiotemporal chaos in both the experimental (explained in section 4.2.2) and the simulated system are given in Fig. 5.8. The cross-correlation is normalized to the mean auto-correlation of the sample points, while the cross-correlation of the forced experimental system is nearly independent of the distance; it decreases strongly with distance in the unforced turbulent state. The numerical results show

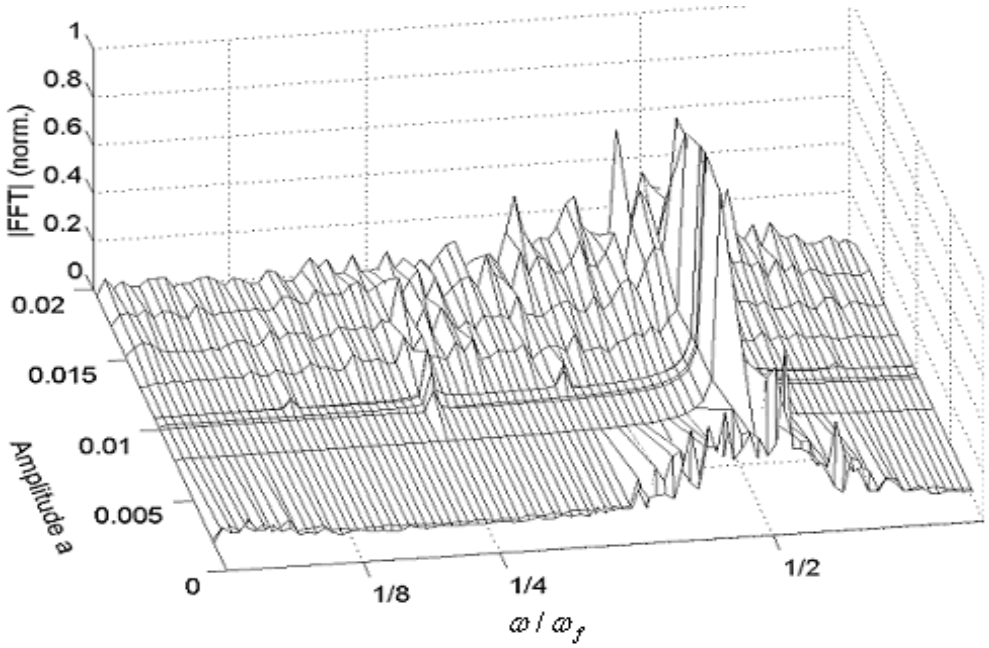

Figure 5.6: Periodically forced KEE model. Low frequency part of Fourier spectra at different forcing amplitudes.

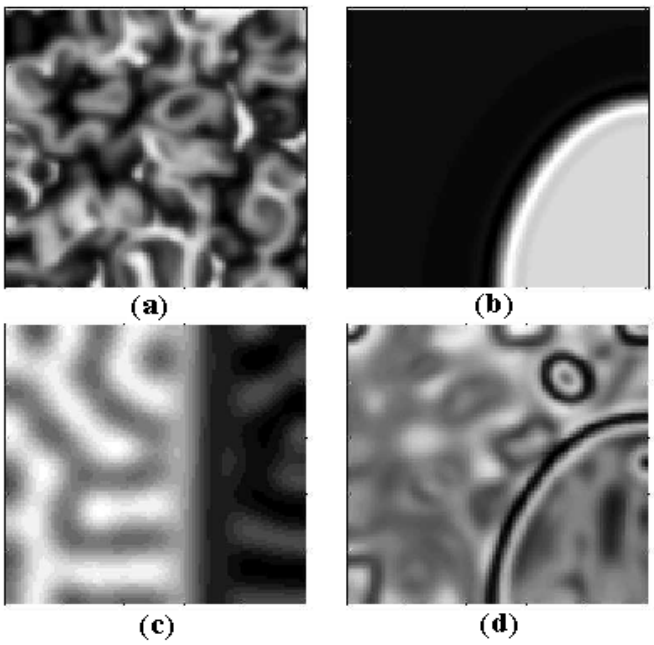

Figure 5.7: Simulated CO coverage for different entrainment states. (a) unforced turbulence, (b) 4:1 entrainment, (c) 8:1 entrainment, and (d) chaotic.

the same qualitative behavior, but the difference between the two states is less pronounced. The shorter correlation length in the unforced experiment compared with the simulation can be explained by noise. On the other hand, the higher correlation of the forced experiment might be induced by stronger forcing, as the numerical result is obtained near the lower amplitude boundary of the chaotic regime.

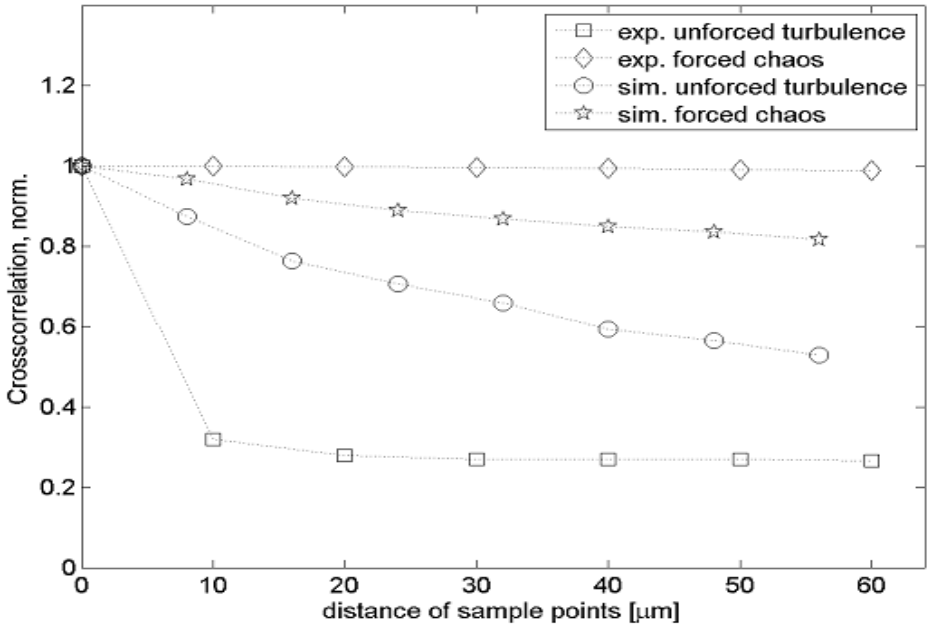

Figure 5.8: Mean spatial cross-correlation of unforced turbulence and forced chaotic oscillations. Results are given for experimental and numerical data.

5.3 3:1 Forcing

5.3.1 3:1 Entrainment

Resonant forcing was applied (ω_f close to $3\omega_{0,ext}$). At forcing amplitude A = 0.0865, the phase locked clusters were observed. In Fig. 5.9(a), the snapshots of three phase locked clusters after each forcing cycle are shown. The space-time plot (Fig. 5.9(b)) explains that the domain walls are not stationary. This is visible in the space-time stro-

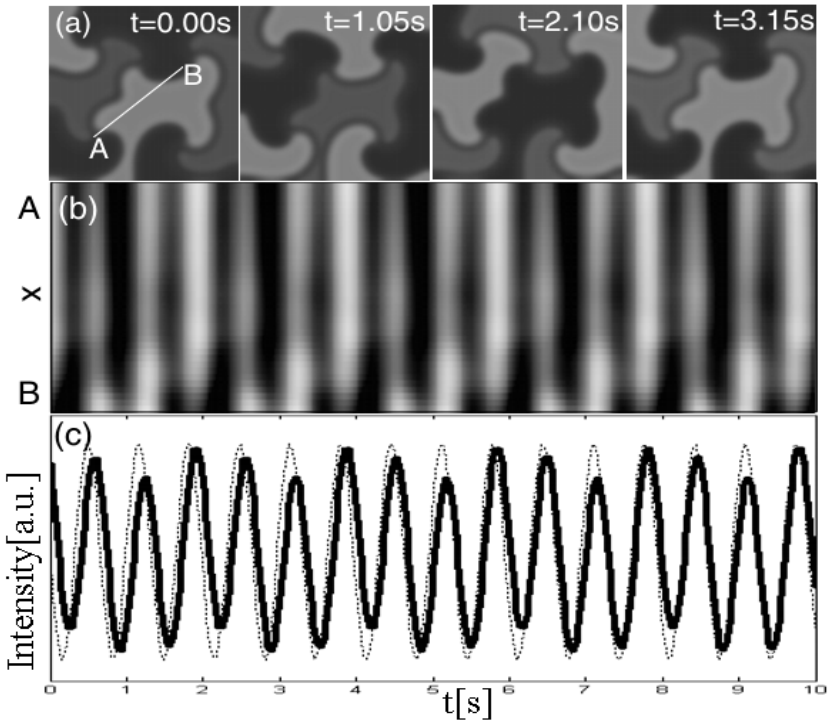

Figure 5.9: Three phase cluster at 3:1 entrainment. (a) snapshots of CO coverage (size $400 \times 400\ \mu m^2$), (b) space-time plot along the AB line from Fig. 5.9(a), and (c) CO coverage along the line AB (solid line) and forcing signal (dotted line). Forcing parameters are $\omega_f = 1.53$Hz and A = 0.0865.

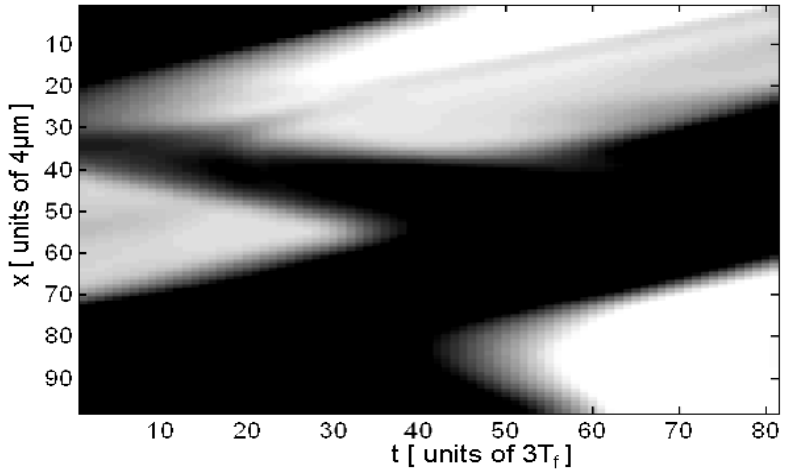

Figure 5.10: Space-time stroboscopic plot showing the pattern evolution along the same AB line of Fig. 5.9(a), choosing one frame every three forcing cycles.

boscopic plot Fig. 5.10 taken along the line AB shown in Fig. 5.9(a), but choosing one frame for every three forcing cycles. The amplitude is increased, moving three-phase clusters are observed until the system changes to 1:1 entrainment with homogeneous oscillations.

The three phase states are clearly visible in phase pattern Fig. 5.11(a) and the phase portrait Fig. 5.11(c). All phase states appear with the same amplitude (Fig. 5.11(b)), while only the phase fronts show decreased amplitude, and amplitude defects i.e., points where the amplitude is decreased to zero and the phase is undefined appear at locations where all three phase states meet. The histogram Fig. 5.11(d) shows that the phase difference between the cluster states is $2\pi/3$.

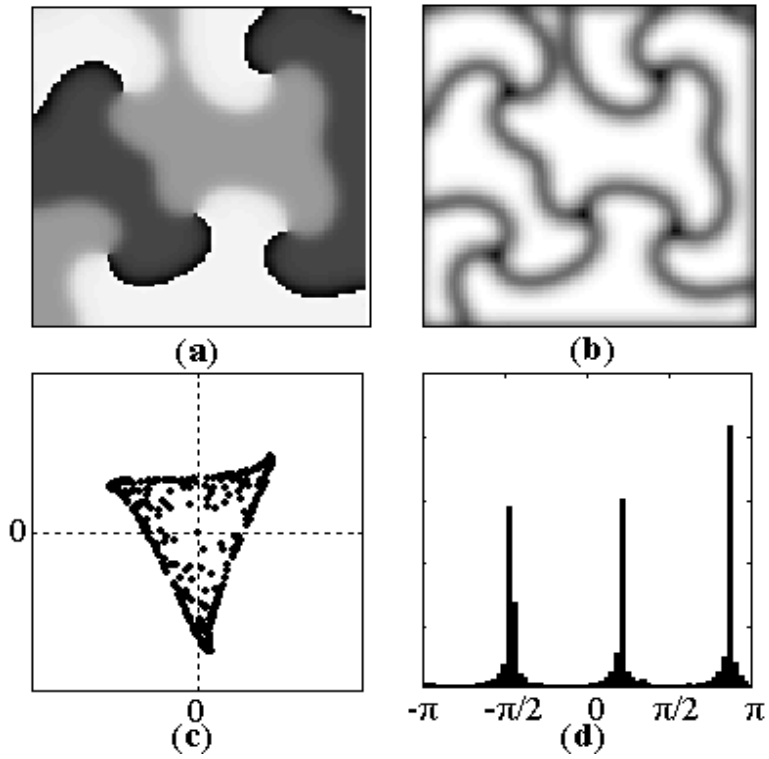

Figure 5.11: Phase and amplitude representation of the cluster patterns shown in Fig. 5.9(a). (a) phase pattern, (b) amplitude pattern, (c) phase portrait, and (d) phase histogram.

5.3.2 6:1 Entrainment

When the forcing amplitude A was fixed and the forcing frequency was changed to $\omega_f = 1.54$Hz, a phase locked regime with stable cluster patterns, 6:1 entrained, was observed (see Fig. 5.12). The arising spatiotemporal patterns exhibit a periodicity of six forcing cycles, which indicates that the system performs period doubled 6:1 entrained oscillations. The space-time plot (Fig. 5.12(b)) indicates that the domain walls are moving slowly.

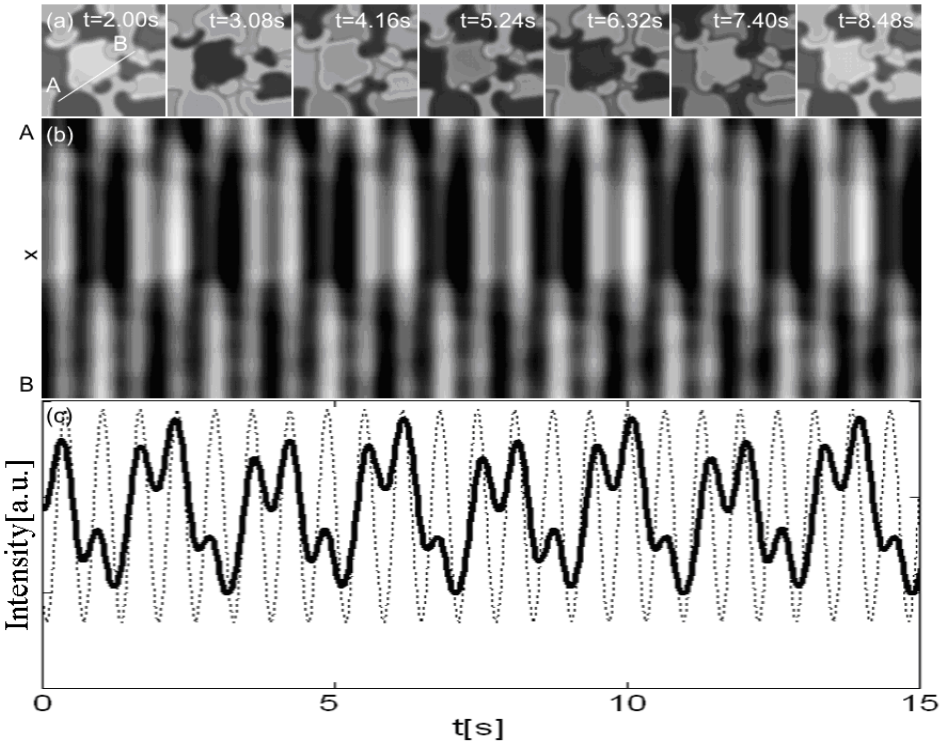

Figure 5.12: Six phase cluster under 3:1 forcing at 6:1 entrainment. (a) snapshots of CO coverage (size 400×400 μm^2), (b) space-time plot along the AB line from Fig. 5.12(a), and (c) CO coverage along the line AB (solid line) and forcing signal (dotted line). Forcing parameters are $\omega_f = 1.53$Hz and A = 0.0865.

The six phase states are clearly visible in phase pattern Fig. 5.13(a). The amplitude is different only at the boundaries of the clusters (Fig. 5.13(b)). At locations where

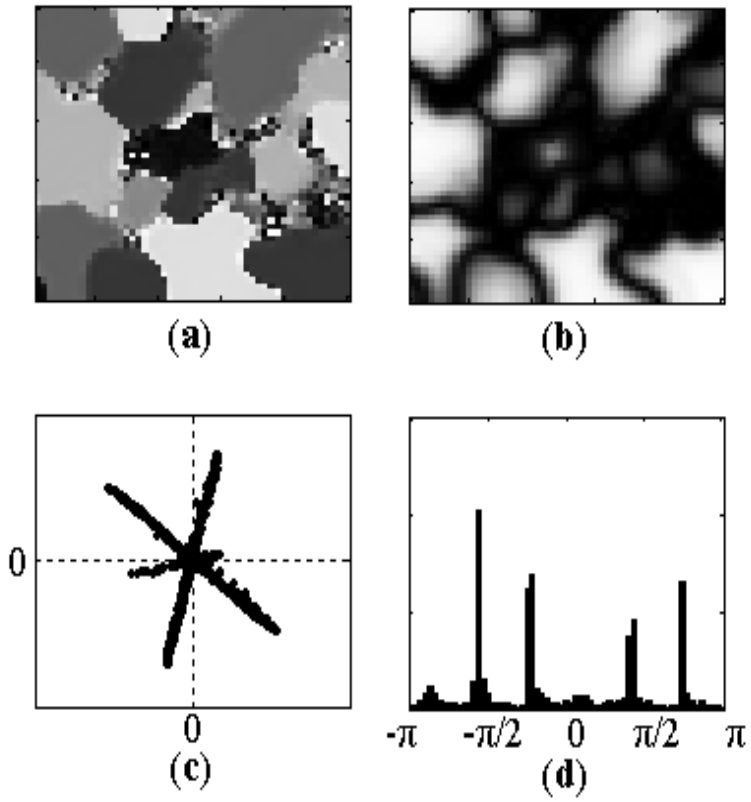

Figure 5.13: Phase and amplitude representation of the cluster patterns shown in Fig. 5.12. (a) Phase pattern, (b) amplitude pattern, (c) phase portrait, and (d) phase histogram.

more than two phase clusters meet, amplitude defects are present. The phase portrait Fig. 5.13(c) shows that the fronts between the six phases always traverse through zero, indicating a standing-wave pattern. The histogram Fig. 5.13(d) represents the high density of six different phases states where the maxima have a phase difference of $2\pi/6$. The six phases are not equally weighted.

On further increasing the forcing amplitude and frequency, transitions from 3:1 to 1:1 oscillation were always found. Like a single oscillator [45], at high forcing amplitude two phase cluster could not be observed under 2:1 entrainment. The transition from a three phase cluster to 1:1 oscillation is shown in Fig. 5.14.

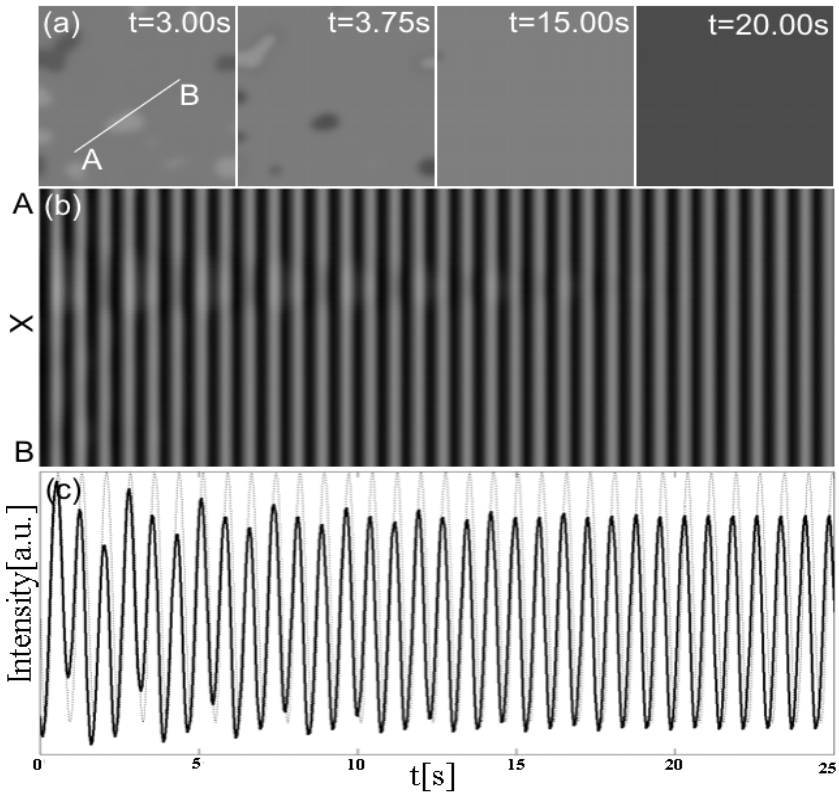

Figure 5.14: Transition from a three phase cluster to oscillation. (a) Snapshots of CO coverage (size $400 \times 400\ \mu m^2$), (b) space-time plot along the AB line from Fig. 5.14(a), and (c) CO coverage along the line AB (solid line) and forcing signal (dotted line). Forcing parameters are $\omega_f = 1.32$ Hz, and A = 0.093.

5.4 4:1 Forcing

5.4.1 Turbulent Regime

Simulations in the turbulent regime are performed for resonant forcing of the complex Ginzburg-Landau equation (CGLE) in Benjamin Fair instability with 2:1 and 3:1 forcing [47, 69, 129], but no simulations on 4:1 resonant forcing have been performed for oscillatory systems in a turbulent state.

As 4:1 forcing is unknown in a single oscillator in turbulent regime, as a first attempt

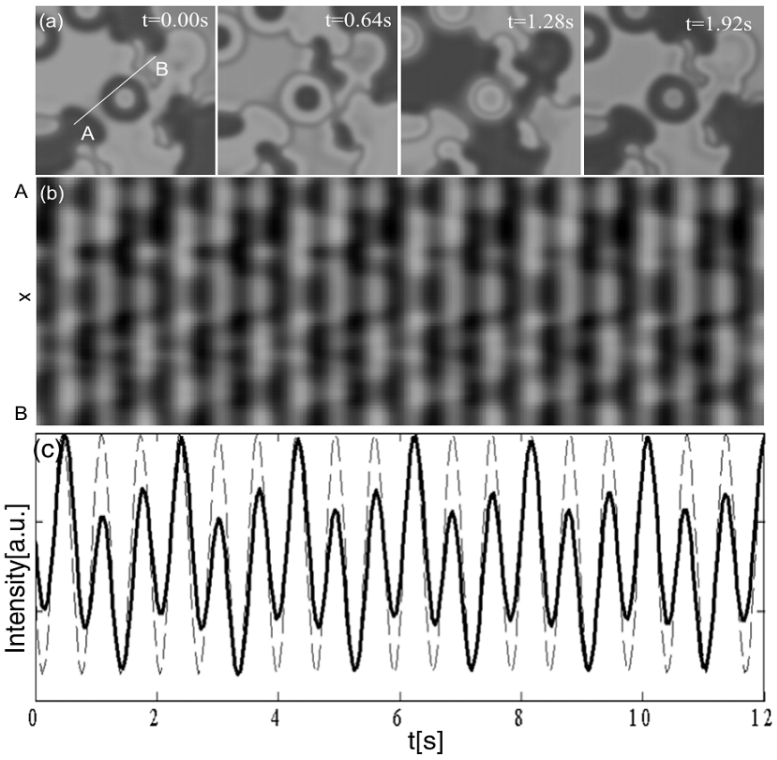

Figure 5.15: Three phase cluster and 3:1 entrainment at 4:1 resonant forcing. (a) snapshots of CO coverage (size 400×400 μm^2), (b) space-time plot along the AB line (see top panel), and (c) local CO coverage at point A and forcing signal (dotted line). Forcing parameters $\omega_f = 1.567$Hz and A = 0.065.

the 4^{th} harmonic of the generic frequency was applied ($\omega_f = 4\omega_{0,single}$), 3:1 entrainment was found with three phase cluster patterns in a wide parameter range of forcing amplitudes and frequency detuning.

Fig. 5.15 shows the snapshots of three phase clusters for A = 0.065, which repeat after three cycles of the forcing period and the space-time plot indicates that the domain walls are not stationary.

The phase and amplitude representations are given in Fig. 5.16. The three different phase states can clearly be seen in the phase plot Fig. 5.16(a) and the phase portrait Fig. 5.16(c). All phase states appear with the same amplitude in Fig. 5.16(b). These

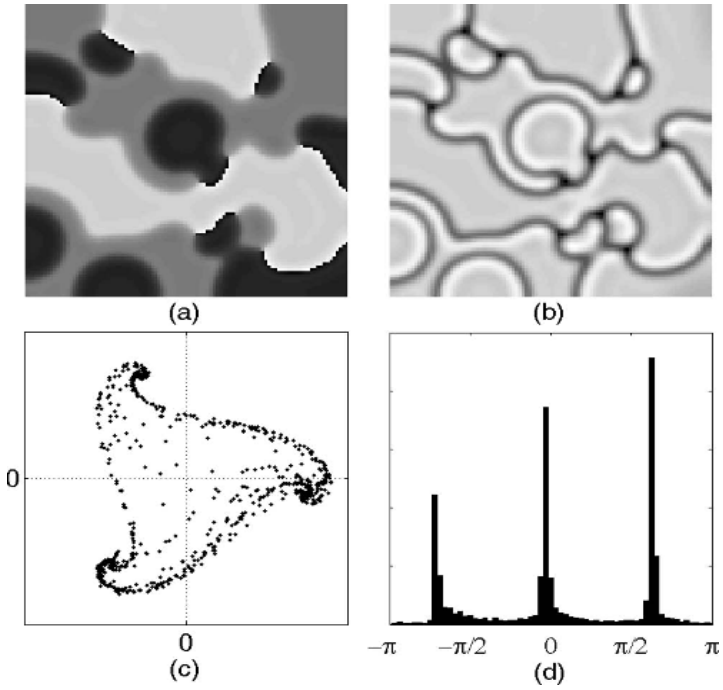

Figure 5.16: Phase and amplitude representations of the cluster patterns shown in Fig. 5.15(a). (a) phase pattern, (b) amplitude pattern, (c) phase portrait, and (d) phase histogram.

findings explain the 3:1 entrainment when forcing with the 4^{th} harmonic of the single oscillator's natural frequency and the absence of 4:1 entrainment.

Even if transient 4:1 entrainment was sometime observed, long-term simulations always ended up in 3:1 entrainment and three phase pattern or at high amplitude in homogeneous oscillations with 1:1 entrainment to the forcing frequency. Four phase entrainment under 4:1 resonance forcing was observed. A possible bistability between 3:1 and 4:1 locking, similar to the bistability of 3:1 and 2:1 near $\omega_f = 3\omega_0$ found by Davidson [45], could not be verified. A 4:1 regime within the vicinity of the $\omega_f = 4\omega_0$ could not be found.

Therefore, the system was forced by the 4^{th} harmonic of the most prominent frequency of the turbulent system which leads in four phase patterns with partial or full 4:1 entrainment, depending on the reaction parameters chosen. On applying A = 0.086,

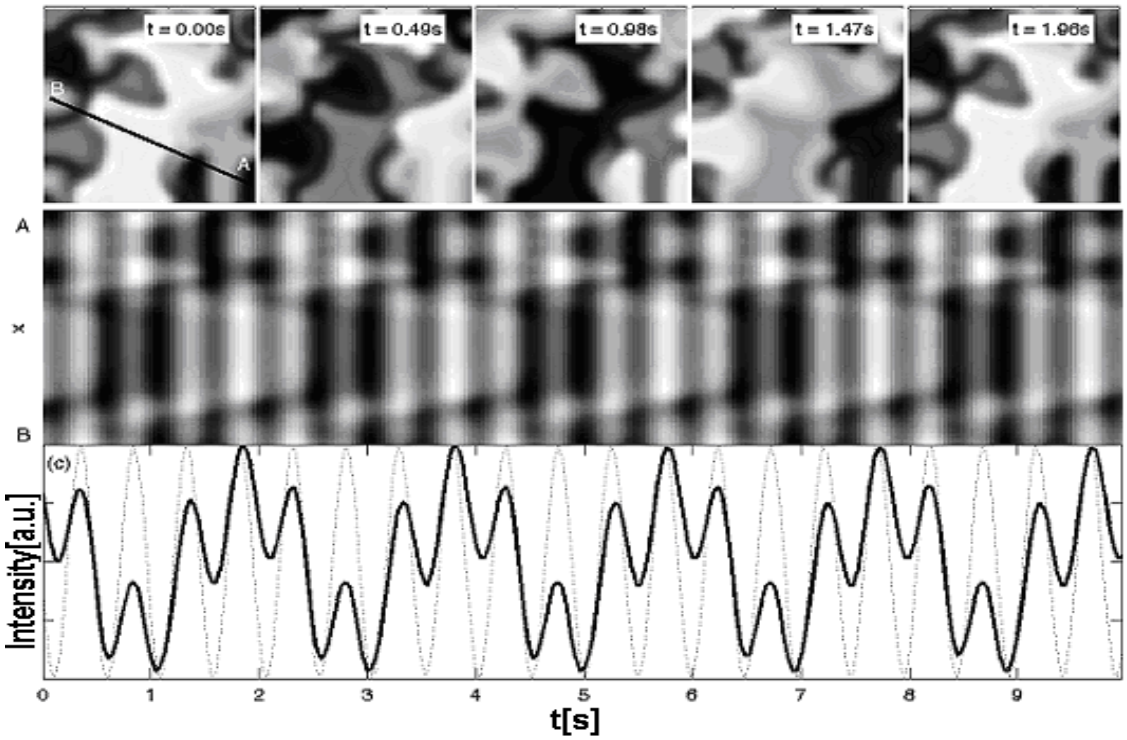

Figure 5.17: Four phase cluster and entrainment at 4:1 resonant forcing. (a) snapshots of CO coverage (size 400×400 μm^2), (b) space-time plot along the AB line (see top panel), and(c) Local CO coverage at point A and forcing signal (dotted line). Forcing parameters: $\omega_f = 2.04$Hz and A = 0.086.

$\omega_f = 2.04$Hz, the system is entrained and four phase clusters appear. Snapshots of the pattern, the evolution along a line section, and the CO coverage for a sample point is given in Fig. 5.17.

The snapshots show separated phase clusters, which repeat every four cycles of the forcing period. The boundaries of the phase clusters seem to move from one forcing cycle to the other. This is visible in the space-time plot (Fig. 5.17(b)), where the bright clusters seem to shrink, but then recover to their original width within the next cycle of the system's oscillation (covering four cycles of the forcing signal, as can be seen in Fig. 5.17(c)).

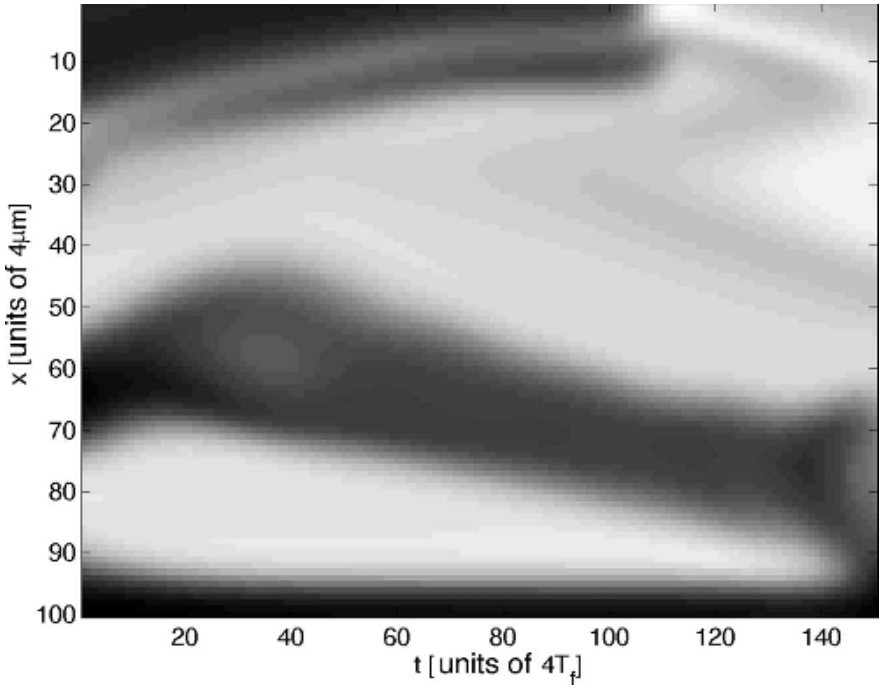

Figure 5.18: Stroboscopic space-time plot showing the pattern evolution along a vertical line on the surface every 4^{th} forcing cycle. Forcing parameters are the same as in Fig. 5.17.

Fig. 5.18 shows a stroboscopic space-time plot, where the CO coverage is shown along a vertical line of the surface every 4^{th} forcing cycle. The movement of the cluster boundaries is clearly visible. The phase front velocity varies, which might be due to the varying orientation of the phase front's normal to the intersection as well as due to the different curvature of the phase front.

The phase representation again shows the prominence of four phase states, visible as four different gray levels in Fig. 5.19(a) and as highly populated points in the phase portrait Fig. 5.19(c). The histogram Fig. 5.19(d) shows the high density of four different phase states where the maxima have a phase difference of $\pi/2$.

Fronts between the clusters are represented by lines of low amplitude in Fig. 5.19(b) where most of the phase fronts are $\pi/2$. The π fronts appear at the broadened boundaries. At locations, where more than two phase clusters meet, amplitude defects are

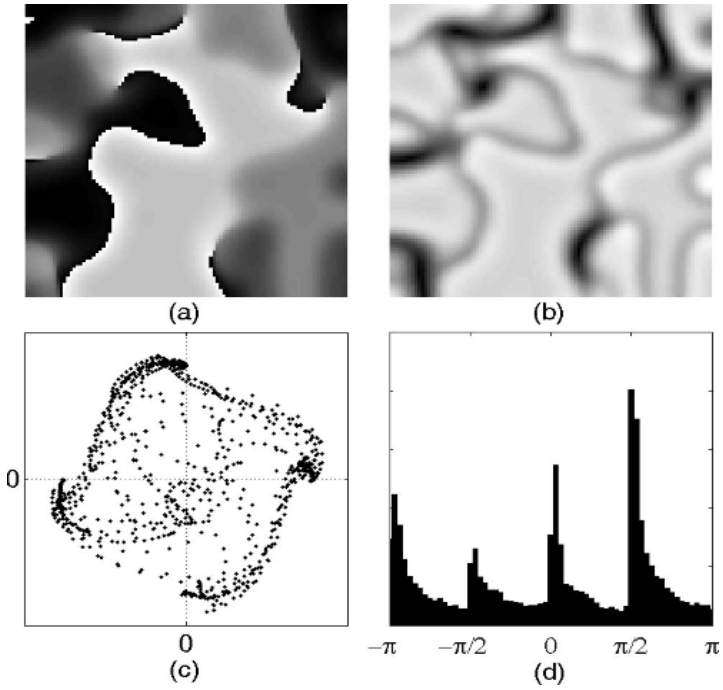

Figure 5.19: Phase and amplitude representations of the cluster patterns shown in Fig. 5.17(a). (a) phase pattern, (b) amplitude pattern, (c) phase portrait, and (d) phase histogram.

present. The phase fronts are not stationary but move slowly.

Due to local analysis and finite frequency resolution of 0.02Hz within the experiments, the estimation of the natural frequency is subject to errors, which may result in a slight frequency mismatching, therefore we simulated the response of the system under moderate detuning. The system is driven with $\omega_f = 2$Hz, keeping the amplitude at A = 0.086. Results are presented in the time domain (Fig 5.20) as well as in the Fourier domain (Fig. 5.21)). The snapshots of the CO coverage (Fig. 5.20(a)) show remarkable higher turbulent behavior. A few phase clusters with locally homogeneous CO coverage are visible, mainly located at the borders of the surface. Large parts of the surface show no sharp phase fronts, but a smooth change of CO coverage. They exhibit quasi-periodic behaviors, as deviations from periodic behaviors are not visible on small time scales of a few T_f.

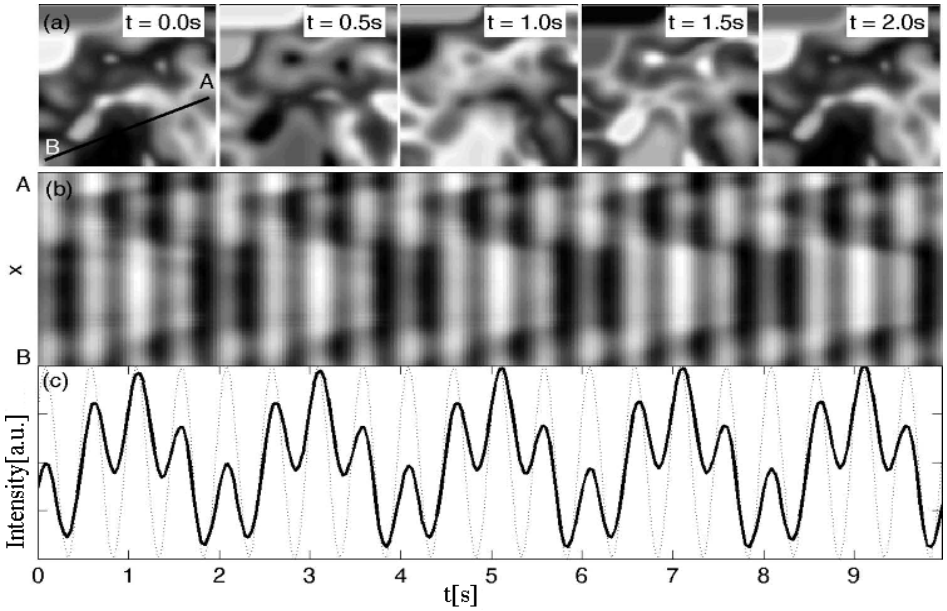

Figure 5.20: Four phase cluster and entrainment at 4:1 resonant forcing. (a) snapshots of CO coverage size 400×400 μm^2, (b) space-time plot along the AB line (see top panel), and (c) local CO coverage at point A and forcing signal (dotted line). Model parameters: $\omega_f = 2.04$Hz and A = 0.086.

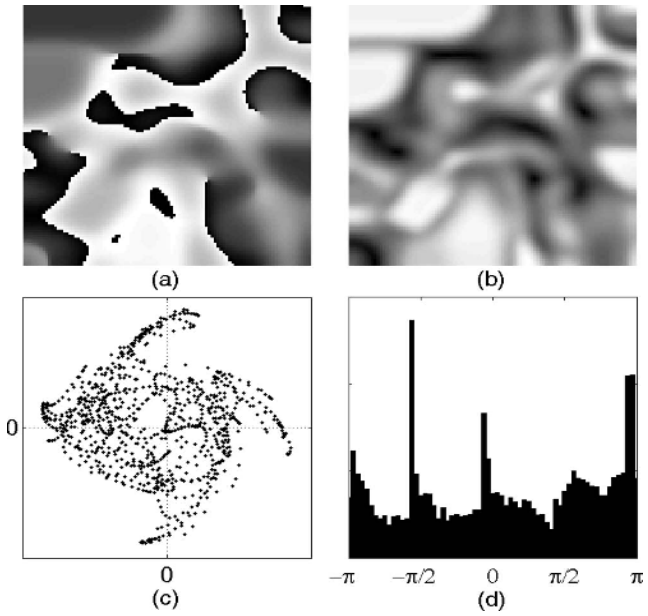

Figure 5.21: Phase and amplitude representations of the cluster patterns given in Fig. 5.20(a). (a) Phase pattern, (b) amplitude pattern, (c) phase portrait, and (d) phase histogram.

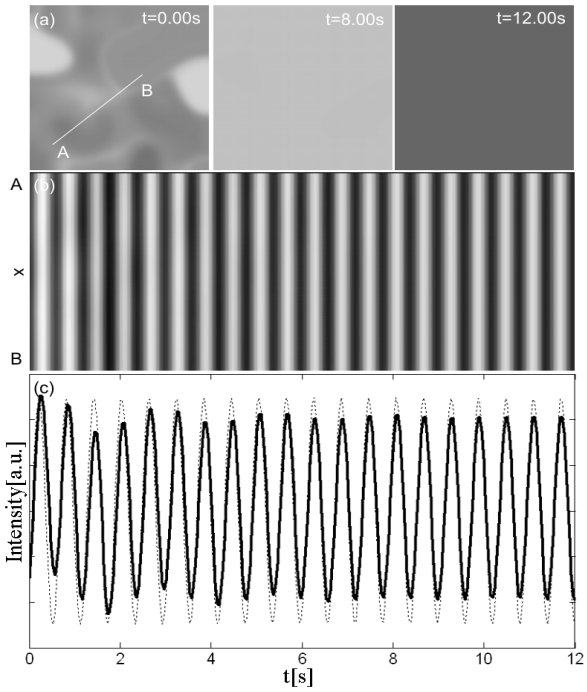

Figure 5.22: Transition from four phase cluster to oscillation at 4:1 resonant forcing. (a) snapshots of CO coverage (size 400×400 μm^2), (b) space-time plot along the AB line (see top panel), and (c) local CO coverage at point A and forcing signal (dotted line). Model parameters: $\omega_f = 2.04$Hz, and A = 0.129.

Although the space-time plot and the local time series show no qualitative difference from the system at resonant forcing (compared to Fig. 5.18), analysis of the phase and amplitude representation (Fig. 5.21 (a) and (b)) reveal an increased number of topological defects; large parts of the system feature a decreased oscillation amplitude while the phase clusters appear as regions with high amplitude, visible as bright regions in Fig. 5.21(b). This can also be seen in the phase portrait, shown in Fig. 5.21(c), where the phase-amplitude distribution of the surface elements is less concentrated at maximum amplitude. The phase histogram, presented in Fig. 5.21(d), still contains four peaks with a phase difference of $\pi/2$.

Increasing the amplitude, four phase clusters are observed moving until the system changes to 1:1 entrainment with homogeneous oscillations (Fig. 5.22).

5.4.2 Nonturbulent Regime

Most of the numerical studies are done in the nonturbulent regime. The well known examples are the CGLE, FitzHugh-Nagumo (FHN) and Brusselator models [39, 71]. All of the models predict four phase moving clusters at low forcing amplitude and two phase stationary clusters at high forcing amplitude.

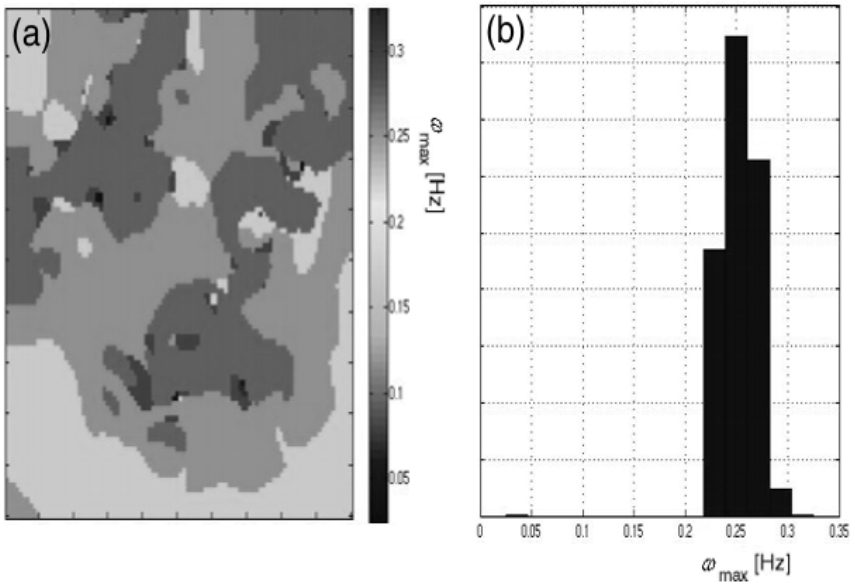

Figure 5.23: Natural frequency of the system in nonturbulent regime. (a) spatial distribution, and (b) histogram of most prominent frequency in a numerical simulation of unforced turbulence.

Four phase stationary cluster were consistently found at low forcing amplitude and two phase stationary clusters were found at high forcing amplitude. The model parameters and the reaction parameters are given in Chapter 3, Table 3.2. The natural frequency of the system is shown in Fig. 5.23, which is about 0.25Hz.

Four Phase Cluster

The forcing was applied at four times the natural frequency. At forcing amplitude A = 0.042, the four phase patterns were found. Fig. 5.24 shows the snapshots of the four

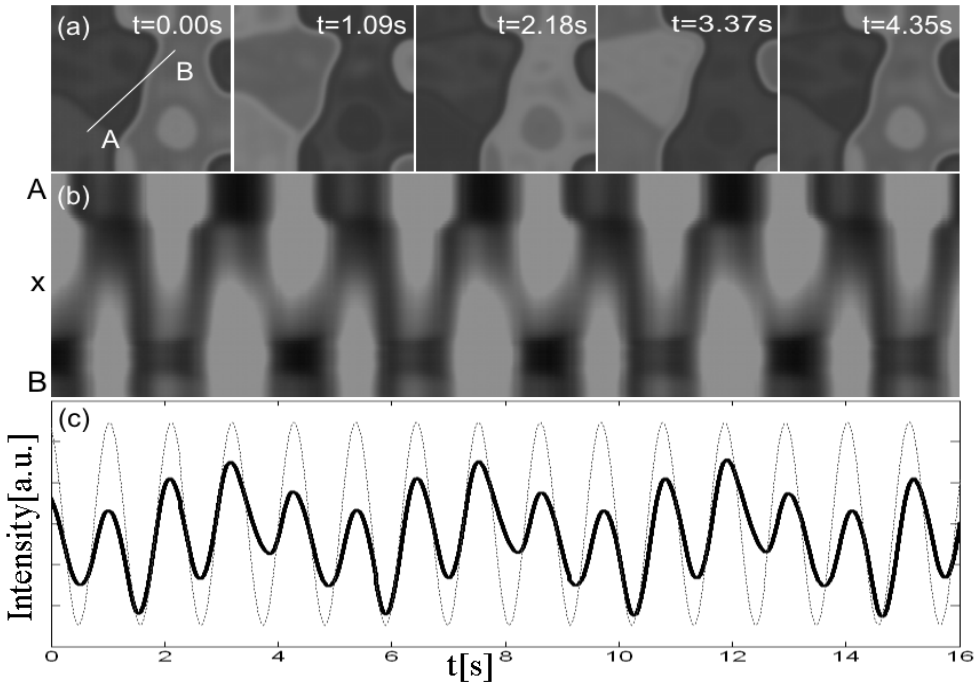

Figure 5.24: Four phase cluster at 4:1 resonant forcing. (a) snapshots of CO coverage (size 400×400 μm^2), (b) space-time plot along the AB line (see top panel), and (c) CO coverage (solid line) and forcing signal (dotted line). Model parameters: $\omega_f =$ 0.92Hz and A = 0.042.

phase clusters taken after one forcing cycle. The boundaries of the phase clusters are stationary from one forcing cycle another, as seen in the space-time plot Fig. 5.24(b). The stationary behavior of the cluster can be seen clearly in the stroboscopic space-time plot Fig. 5.25, where the CO coverage is shown along a vertical line of the surface every 4^{th} forcing cycle.

Phase and amplitude representations are given in Fig. 5.26. In phase pattern Fig. 5.26(a), four phase states (black, gray, light gray, and dark gray) are visible as four different gray levels. The amplitude drops only at the boundary of the cluster (Fig. 5.26(b)). The phase portrait Fig. 5.26(c) shows that the fronts between the four phases always traverse through zero, indicating a standing-wave pattern and the high density of four different phase states, where the maxima have a phase difference of $\pi/2$, as shown in phase histogram Fig. 5.26(d).

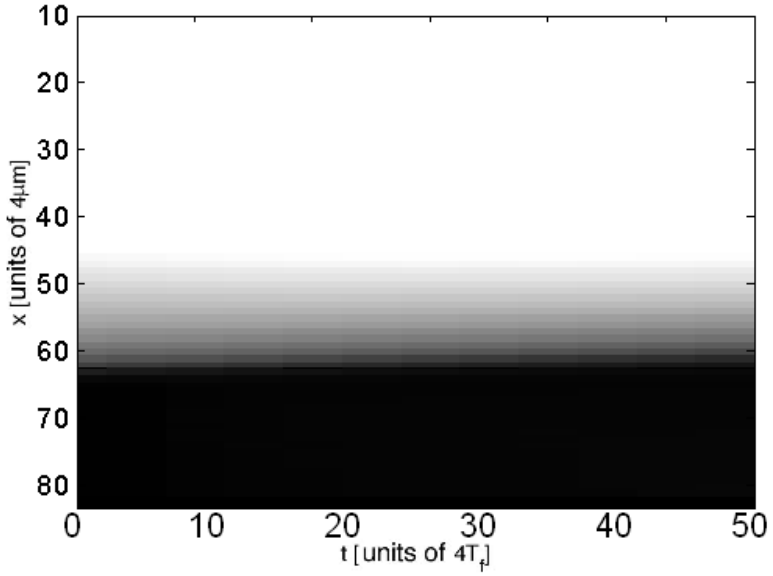

Figure 5.25: Space-time stroboscopic plot showing the pattern evolution along the same AB line of Fig. 5.24(a), choosing one frame every four forcing cycles.

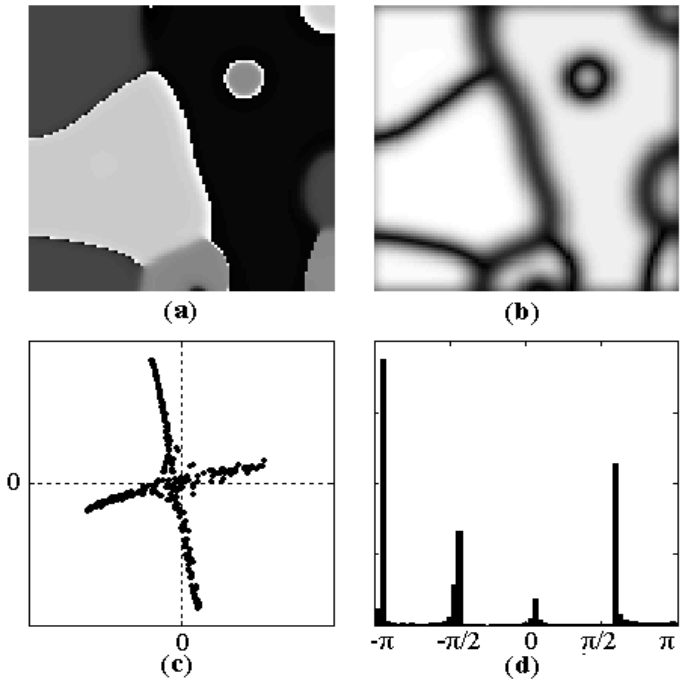

Figure 5.26: Phase and amplitude representations of the cluster patterns shown in Fig. 5.24(a). (a) phase pattern, (b) amplitude pattern, (c) phase portrait, and (d) phase histogram.

Two Phase Cluster

At forcing amplitude A = 0.074, the two phase stationary cluster was observed. Fig. 5.27(a) shows the snapshots of the two phase cluster, taken after each forcing cycle. The boundary of the cluster is always stationary, as can be seen in space-time plot Fig. 5.27(b). Fig. 5.28 shows a stroboscopic space-time plot, where CO coverage is shown along a vertical line of the surface every 2^{nd} forcing cycle.

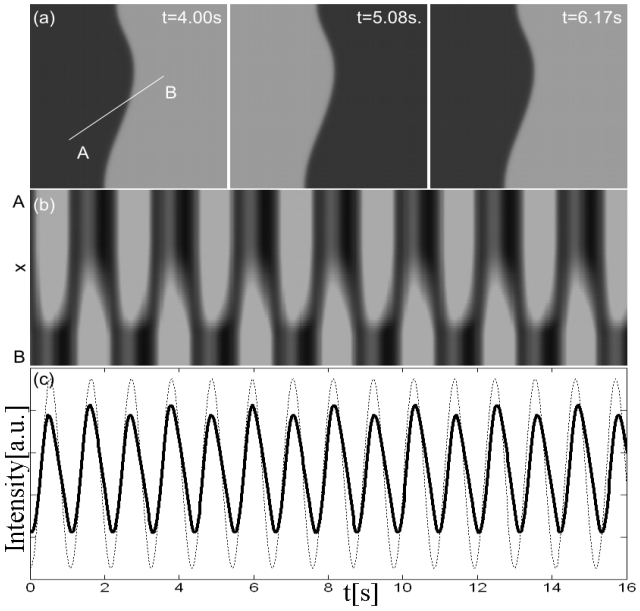

Figure 5.27: Two phase cluster at 4:1 resonant forcing. (a) snapshots of CO coverage (size 400 × 400 μm^2), (b) space-time plot along the AB line (see top panel), and (c) CO coverage (solid line) and forcing signal (dotted line). Model parameters: ω_f = 0.92Hz and A = 0.074.

Phase and amplitude representations are given in Fig 5.29. In phase pattern Fig. 5.29(a), two phase states are visible as two different gray levels. The amplitude pattern Fig. 5.29(b) shows that the amplitudes are approximately the same for the different domains except at the cluster boundary. The phase portrait Fig. 5.29(c) and phase histogram Fig. 5.29(d) shows the high density of four different phase states, where the maxima have a phase difference of $\pi/2$.

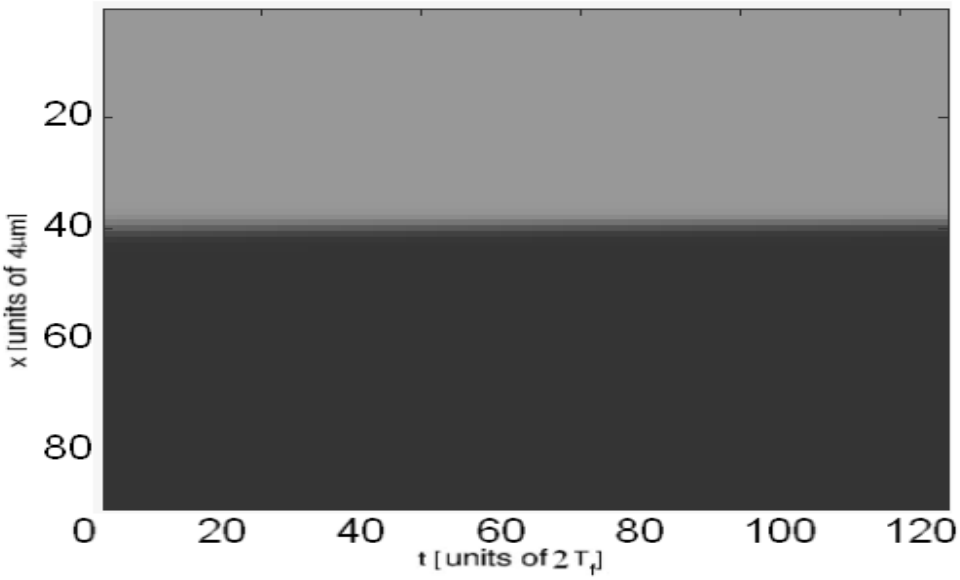

Figure 5.28: Space-time stroboscopic plot showing the pattern evolution along the same AB line of Fig. 5.27, choosing one frame every two forcing cycles.

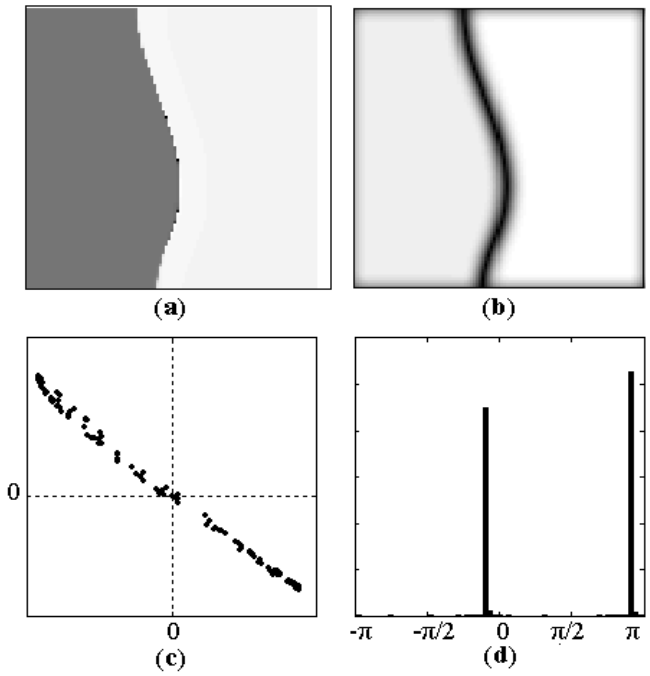

Figure 5.29: Phase and amplitude representations of the cluster patterns shown in Fig. 5.27(a). (a) phase pattern, (b) amplitude pattern, (c) phase portrait, and (d) phase histogram.

Conclusion:

Pattern formations have been investigated in a CO oxidation on Pt(110), forced by an external periodic perturbation in an extended system.

An analysis of the KEE model reveals significant differences between the oscillation frequency of the single oscillator and the mean frequency on the surface, which appears to be higher in the turbulent state due to diffusive interaction of the surface elements.

Interestingly, a similar frequency increase with respect to homogeneous oscillations was found for the spiral-wave oscillation frequency in the BZ reaction [71]. There, simulations showed entrainment when using the homogenous oscillation frequency and quasi-periodic behavior when forcing with the higher spiral-wave frequency, which is in contrast to the findings for the turbulent case. This is of major impact for the attempt of controlling the system by resonant forcing.

Under 2:1 forcing the path to chaos is given by a period doubling cascade, which could be followed by subsequent increase of the forcing amplitude is verified theoretically. Experimentally, two types of clusters named phase and amplitude clusters were found, however, theoretically only the phase clusters were observed.

In 3:1 resonance forcing, three phase moving clusters and six phase stationary clusters were found under 3:1 and 6:1 entrainment respectively, like in the FitzHugh-Nagumo (FHN) model [77].

The bistability between 2:1 and 3:1 could not be found even at high forcing amplitude and frequency. At high forcing amplitude and frequency the transition from three phase cluster to homogeneous oscillations takes place (see Fig. 5.14).

The application of 4:1 forcing with the 4^{th} harmonic of the natural frequency of the single oscillator leads to 3:1 entrained three phase patterns; 4:1 entrainment could be obtained by forcing with the 4^{th} harmonic of the mean oscillation frequency. Weak detuning leads to the appearance of turbulent regions.

Numerical simulations of the KEE model in the 4:1 nonturbulent regime reproduces standing four phase clusters as well as two phase clusters at a higher amplitude, in contrast to CGLE and FHN which predict four phase moving and two phase stationary

clusters at low and high forcing amplitudes [39, 71].

The greater the difference between these two characteristic frequencies, the more difficult it is to entrain both turbulent and phase-clustered regions. A necessary condition for entrainment of the phase clusters is that the forcing frequency lie within the respective Arnold's tongue of the single oscillator.

Further investigation of high-frequency forcing of turbulent reaction-diffusion systems may give new insight into the nature of turbulence and may lead to new strategies for controlling chaos.

Chapter 6

Defect Mediated Turbulence

The most basic feature of the chemical turbulence (also known as defect mediated turbulence), is that the spatial disorder is generated by so-called defects, which present singularities in the field of the oscillation phase.

The spatiotemporal chaos originates from the spontaneous and persistent creation and annihilation of topological defects.

A defect is characterized by its integer topological charge m_{top}, which is defined by

$m_{top} = \frac{1}{2\pi} \oint \nabla\phi(\mathbf{x}, t).d\mathbf{s}$

where $\phi(x, t)$ is the local phase and the integral is taken along a closed curve surrounding the defect.

Experimentally defect turbulence has been found to be abundant in systems such as autocatalytic chemical reactions [130, 131], fluid convection [132, 133], electro convection in liquid crystals [134], and in nonlinear optics [135].

Theories about defect mediated turbulence have been extensively studied in the CGLE

system [10, 10, 136], which describes universal dynamics features of spatially extended systems near a supercritical Hopf bifurcation.

The first probabilistic characterization of defect turbulence was given by Gil *et. al.* [136] for the regime of amplitude turbulence in the CGLE. They considered a system with periodic boundary conditions and assumed a constant rate of creation for pairs of topological defects, independent of the number of pairs m in the system. The rate of annihilation was taken proportional to m^2 since defects annihilate in pairs of opposite topological charge. In this Chapter the statistical properties of defect mediated turbulence in catalytic CO oxidation on Pt(110) are described by using the probabilistic model with increasing order of CO pressure.

Recently Beta *et. al.* [131] have analyzed the statistical properties of chemical turbulence in oscillatory catalytic CO oxidation on Pt(110) based on the experimental data, where the two-dimensional experimental images are transformed into phase and amplitude patterns. The defects are identified from phase images which are not related to the surface heterogeneities.

By assuming that the defects are statistically independent, the shape of the probability distribution function (PDF) can be explained in terms of a simple probabilistic model, based on the gain and loss rates of defects in the observed area. By use of a nearest-neighbor tracking algorithm, they follow defects between adjacent frames and identify creation (C) and entering (E) events as well as defects decay (D) and leaving (L) the area of observation.

The observed rates are approximately given by

$$C(N)) = C_0 \tag{6.1}$$

$$E(N) = E_0 \tag{6.2}$$

$$L(N) = L_0 N \tag{6.3}$$

$$D(N) = D_{01}N^2 + D_{02}N \tag{6.4}$$

In the statistically stationary state, the master equation for the probability p(N) of finding a number of N defects in the observed area can be written in the simple recursive relation.

$$\begin{aligned} \partial_t p(N,t) = k_+(N-1)p(N-1,t) + k_-(N+1)p(N+1,t) \\ -k_+(N)p(N,t) - k_-(N)p(N,t) \end{aligned} \tag{6.5}$$

where $k_+(N)$ and $k_-(N)$ are the gain and loss rates of the defects. In a asymptotic regime, $\partial_t p(N,t) = 0$, equation (6.5) yields a simple recursive relation for the probability p(N)

$$p(N) = \frac{k_+(N-1)}{k_-(N)} p(N-1) \tag{6.6}$$

where $k_+(N) = C_0 + E_0$,

$k_-(N) = D_{01}N^2 + (D_{02} + L_0)N$

where N denotes the number of positive and negative defects $\mathrm{N} = N_\pm$. C_0, E_0, L_0, D_0 are the creation, entering, leaving, and decay rates respectively.

By performing the recursion and normalization the distribution, a modified distribution is found,

$$p(N) = \frac{\gamma^{(\nu/2+N)}}{I_\nu(2\sqrt{\gamma})\Gamma(1+\nu+N)N!} \tag{6.7}$$

where I_ν is the modified bessel function , $\gamma = (C_o + E_0)/D_{01}$, and $\nu = (D_{02} + L_0)/D_{01}$.

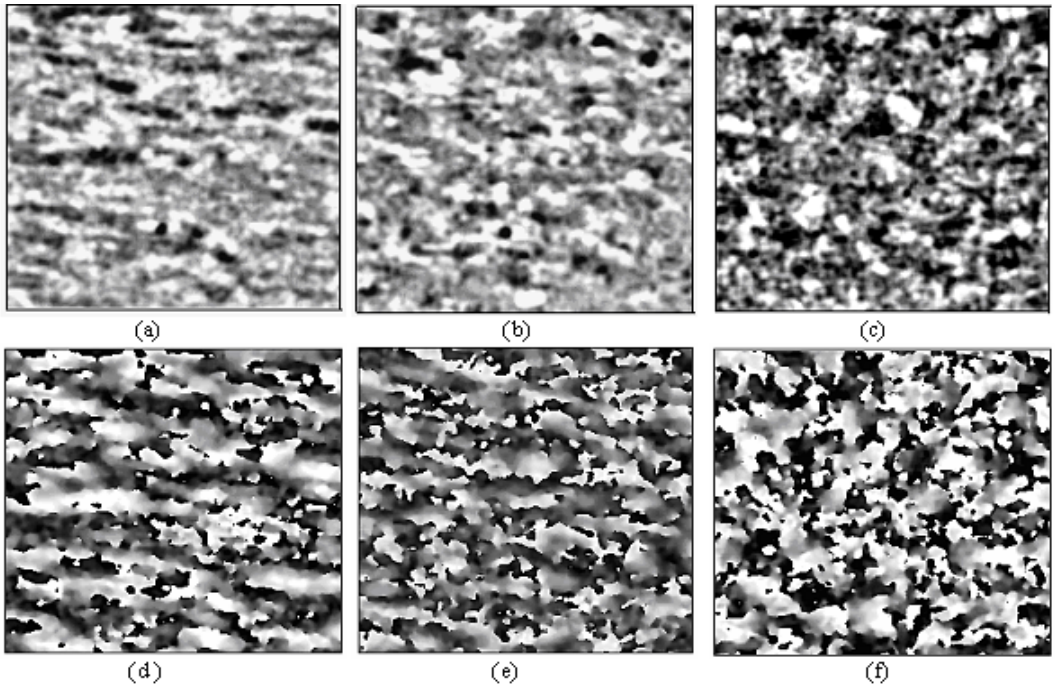

Figure 6.1: Defect mediated turbulence with increasing order of CO pressure. (a) , (b), (c) are PEEM images of size 300×300 μm^2 and, (d), (e), and (f) are the respective phase patterns. The reaction parameters are: T = 534 K, $p_{o_2} = 1.58 \times 10^{-4}$ mbar, p_{co} = (a) 5.85×10^{-5} mbar, (b) 5.91×10^{-5} mbar, and (c) 6.05×10^{-5} mbar

.

6.1 Method

The snapshots of the PEEM images shown in Fig. 6.1 (a), (b), and (c) are 300×300 μm^2 in size. Prior to the actual characterization of turbulent dynamics, standard image processing techniques were applied to enhance contrast and minimize the level of experimental noise. The PEEM images were denoised by application of a 3×3 median filter and finally, a Butterworth high pass filter of order seven with a frequency cutoff at k = 1 was applied to eliminate large scale modulations in the illumination of the PEEM images. The chemical turbulence in oscillatory system with increasing order of CO pressure is analyzed based on a phase and amplitude method.

The phase and amplitude variables are computed from the experimental data by em-

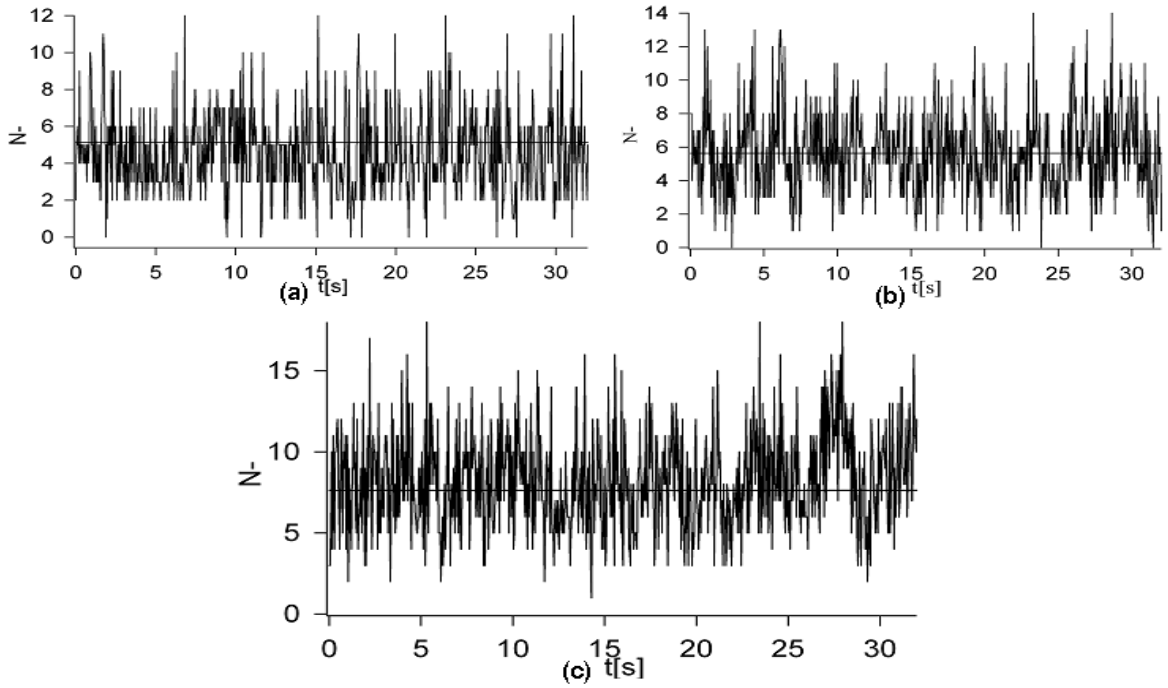

Figure 6.2: Number of negatively charged defects N_- as a function of time (sec.) with increasing order of CO pressure. The mean over all series $N_{+,-}(t)$ in (a) 4.58, (b) 5.62, and (c) 8.23.

ploying a variant of the analytic signal approach. This method is used to transform sequences of experimental PEEM images into time-dependent spatial distributions of phase and amplitude variables. For the local PEEM intensity $I(x,t)$ at an observation point x, its Hilbert transform,

$\zeta(x,t) = I(x,t) + i\bar{I}(x,t)$

where

$\bar{I}(x,t) = \frac{1}{\pi} \int_{-\infty}^{\infty} (t-t')^{-1} I(x,t')dt'$

is the Hilbert transform of $I(x,t)$. The time-dependent spatial distributions of phase $\phi(x,t)$ and amplitude $R(x,t)$ were determined from the analytic signal. The phase was directly computed as $\phi = \arg\xi$, thus representing the polar angle in the plane spanned by the variables I and $\bar{I}$.

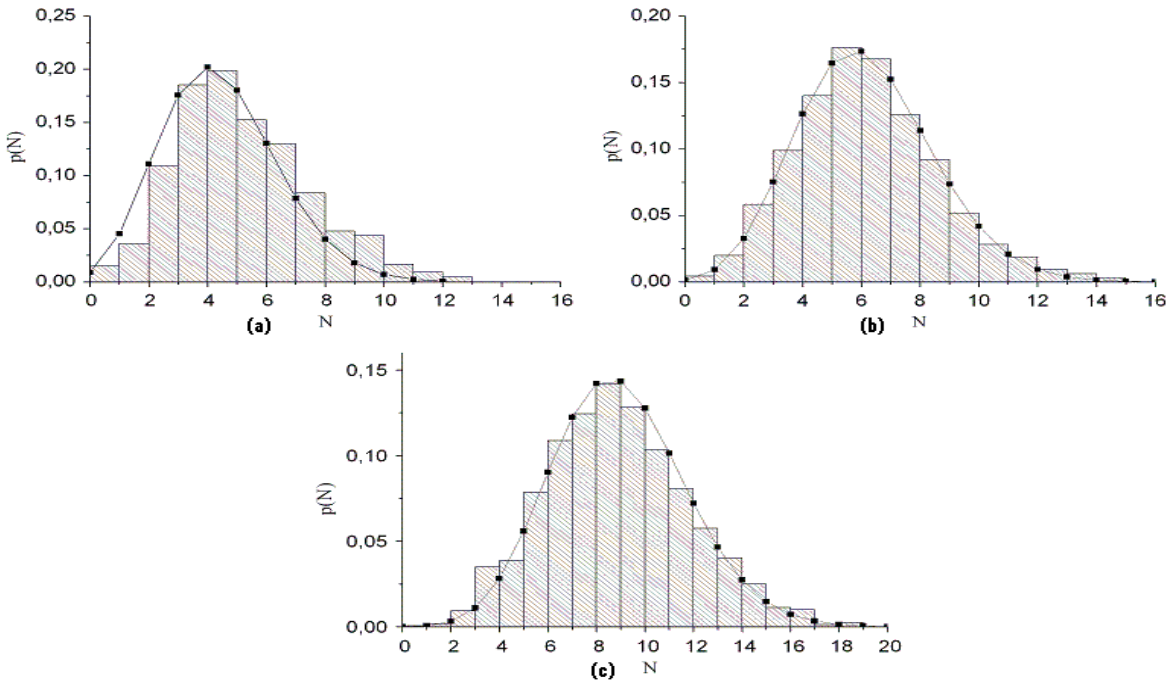

Figure 6.3: Probability distribution function (PDF) of number of defects (N) computed from the all time series $N_{+,-}(t)$ and the modified Poisson distribution (open circles).

The amplitude was defined as $R = \rho/\rho_{ref}(\phi)$, where ρ is the standard definition of the amplitude modulus within the analytic signal approach.

6.2 Experimental Results

Fig. 6.1 (d), (e), and (f) are the phase representations of the PEEM image, shown in (a), (b), and (c), with increasing order CO pressure. In PEEM images and phase patterns one can see that as the CO pressure increases the patterns became more chaotic.

Fig. 6.2 (a), (b), and (c) show the number of negative defects as a function of time with increasing pressure of CO. A steadily increasing average number of defects and growing fluctuation indicate that as the CO pressure increases the system becomes

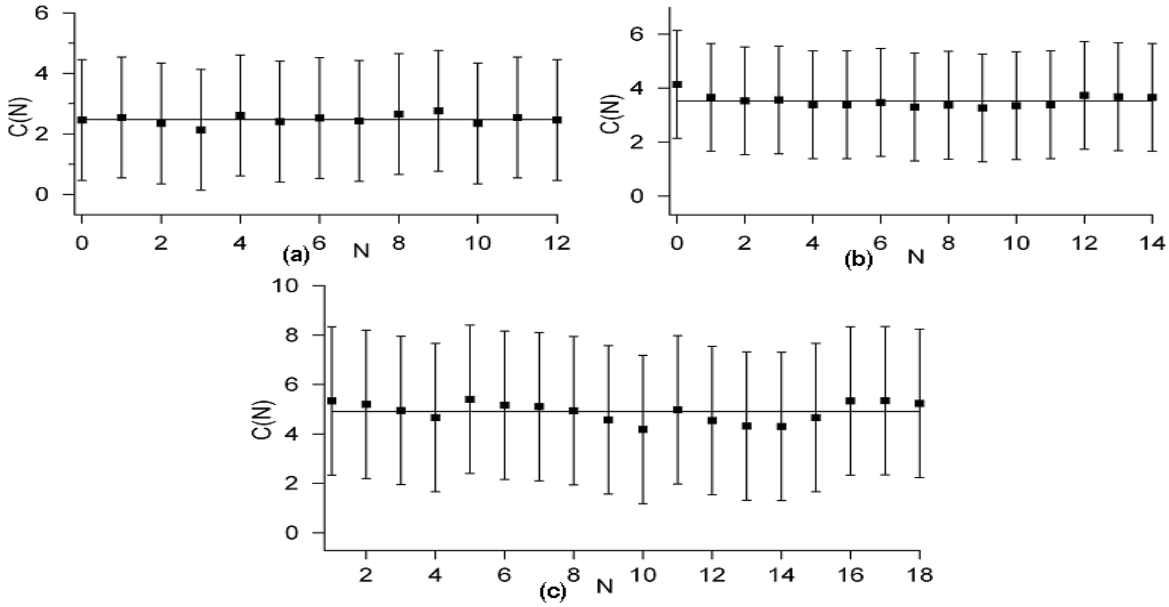

Figure 6.4: Creation rates averaged over the rates for both positive and negative defects. The measured rates are fitted with (a) 2.42, (b) 3.52, and (c) 4.93.

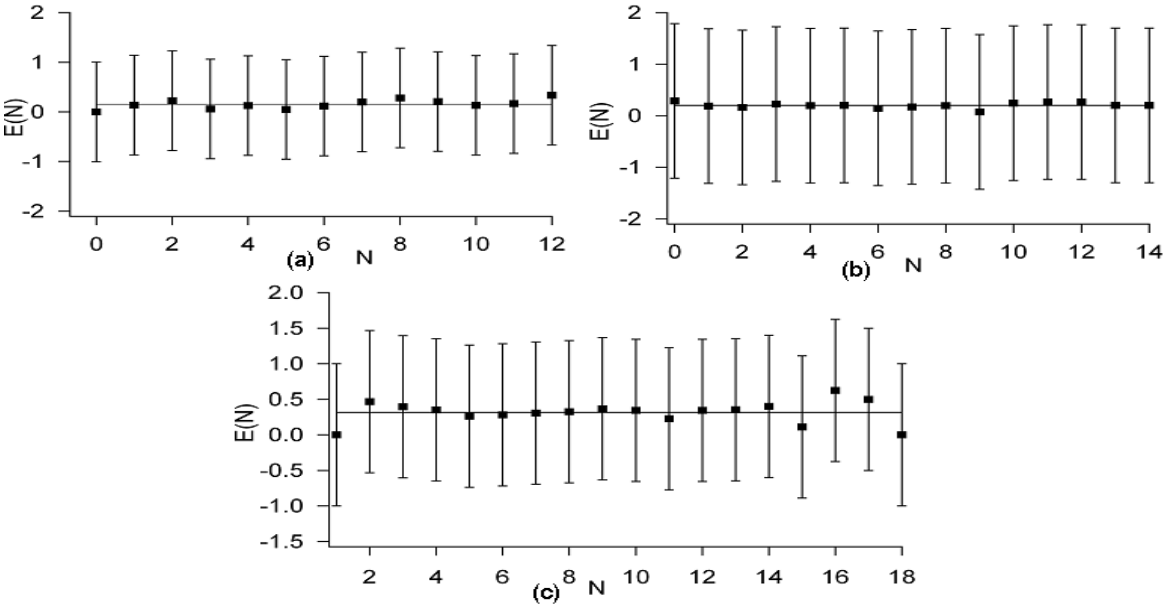

Figure 6.5: Entering rates averaged over the rates for both positive and negative defects with increasing order of CO pressure. The measured are fitted with (a) 0.066, (b) 0.19, and (c) 0.29.

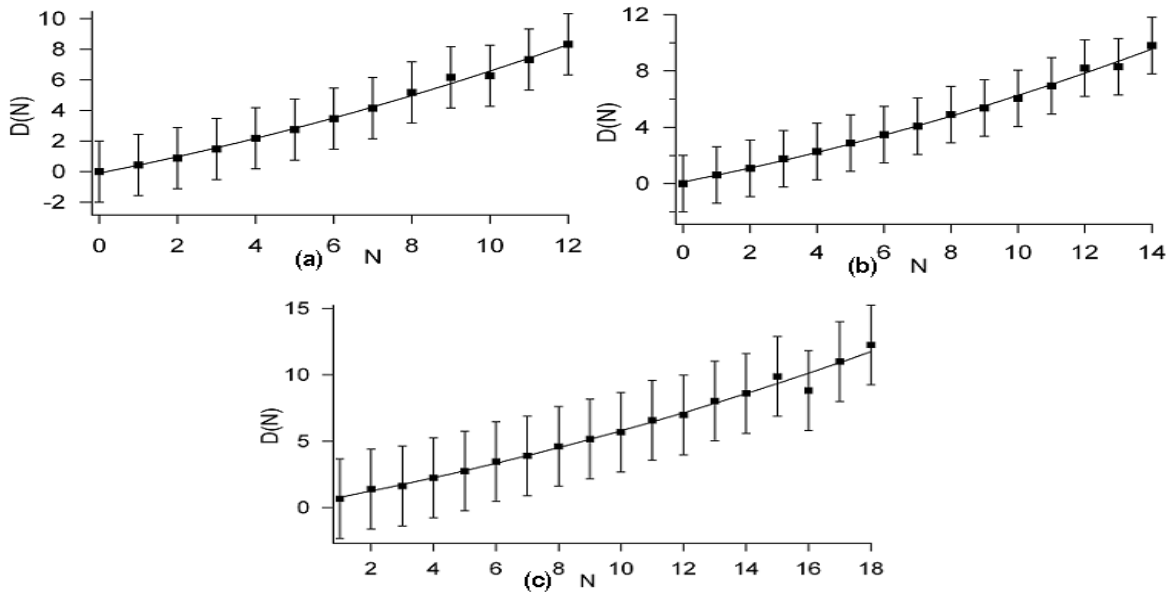

Figure 6.6: Decay rates averaged over the rates for both positive and negative defects with increasing order of CO pressure the measured rates are fitted with (a) $D_{01}(N^2)$ =0.016, $D_{02}(N) = 0.45$, (b) $D_{01}(N^2) = 0.017$, D_{02}(N) = 0.46, (c) $D_{01}(N^2) = 0.014$, D_{02}(N) = 0.44.

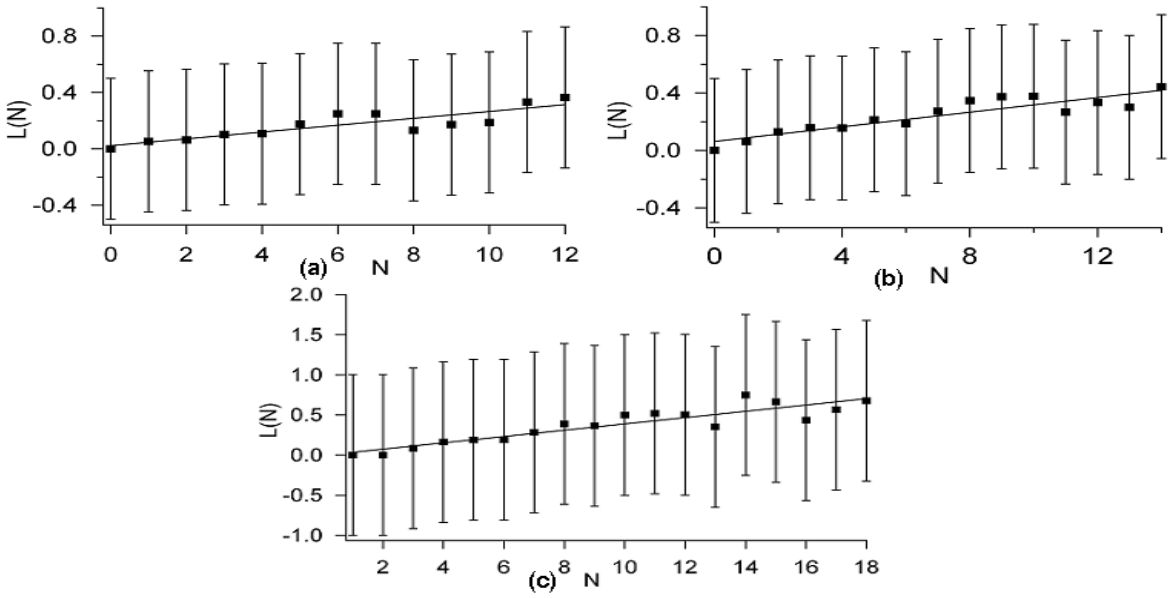

Figure 6.7: Leaving rates averaged over the rates for both negative and positive defects. The measured rates are fitted with (a) 0.024, (b) 0.025, and (c) 0.035

more turbulent. The mean value of Fig. 6.2 (a), (b), and (c) are 4.58, 5.62, 8.23 obtained for the number of positive/ negative defects respectively. Fig. 6.3 (a), (b), and (c) display the PDF for the number of defects (N) in area of 50×50 μm^2 with increasing order of CO pressure.

The resulting gain (creation and entering) and loss (decay and leaving) rates are shown in Fig. 6.4, 6.5, 6.6, and 6.7 respectively. This is the effect due to the dependence of topological defects. The CO pressure is anticipated to have increased the amount of phase instability in the system which is responsible for the creation of defects. The phase gradient under the action of stochastic fluctuations of CO pressure has led to a faster pinching of the equiphases. The relaxation of the field leads thereby to a faster creation of defects (Fig. 6.4).

The modified Poisson distribution shown in Fig. 6.3 (a), (b) , and (c) for the values (open circle) with increasing order of the CO pressure. The modified Poisson distribution approximately match with the experimental data (bars).The modified Poisson distribution obtained by performing the recursion of equation (6.6), shows the well agreement with experimental data from Fig. 6.4, 6.5, 6.6, and 6.7. The modified Poisson distribution correctly captures the mean and width of the PDF. In Fig. 6.3 the modified Poisson distribution is shown for the values in (a) $\gamma = 150.70$, $\nu = 28.75$, (b) $\gamma = 218.70$, $\nu = 28.52$, and (c) $\gamma = 373.07$, $\nu = 33.92$ respectively.

6.3 Conclusion

Like in Beta *et. al.* [131], it was found that the creation and entering rates were constant, leaving rates increase linearly, and the decay rates increase in linear and quadratic way.

The creation and entering rates of defects, which is approximately a constant, is raised to a higher level as the CO pressure increases. The decay and leaving rate of the defects is also increased by the CO pressure.

Under the influence of CO pressure, the probability distributions of defects are flattened more and more as the CO pressure increases, and can be fitted with the modified-

Poisson distribution also found theoretically in modified FHN model under the influence of noise, however they found that the decay rate depended on N linearly [137].

To summarize, it has been shown that the dynamics of defects in defect-mediated turbulence driven by CO pressure can be described by a simple statistical model. Like noise, CO pressure has the ability to create defects in the turbulent background with a constant rate [138], while at the same time destroying the existing defects at a rate that is best approximated by adding a linear contribution to the quadratic annihilation term.

6.4 Appendix: PDF of Topological Defects

The following Appendix includes a detailed derivation of the PDF of the number of topological defects. Based on the gain and loss rates of defects, $k_+(N)$ and $k_-(N)$, the master equation for the probability p(N, t) reads

$$\begin{aligned} \partial_t p(N,t) = k_+(N-1)p(N-1,t) + k_-(N+1)p(N+1,t) \\ -k_+(N)p(N,t) - k_-(N)p(N,t) \end{aligned} \tag{6.8}$$

In the asymptotic regime, $\partial_t p(N,t) = 0$ transforms into a recursive relation for the probability p(N),

$$p(N) = \frac{k_+(N-1)}{k_-(N)} p(N-1) \tag{6.9}$$

The gain and loss rates are approximated by the following expressions

$$k_+(N) = C_0 + E_0 \tag{6.10}$$

$$k_-(N) = D_{01}N^2 + (D_{02} + l_0)N \tag{6.11}$$

putting 6.10 and 6.11 in equation 6.9

$$p(N) = \frac{C_0 + E_0}{D_{01}N^2 + (D_{02} + l_0)N} p(N-1) \tag{6.12}$$

$$p(N) = \frac{\gamma}{N(N+\nu} p(N-1) \tag{6.13}$$

where $\gamma = \frac{C_0+E_0}{D_{01}}$ and $\nu = \frac{D_{02}+L_0}{D_{01}}$

the above equation can be further expanded to

$$p(N) = p(0)\frac{\gamma^N}{N!}\prod_{k=1}^{N}\frac{1}{k+\nu} \tag{6.14}$$

using product of the components of mathematic series

$$a_1.a_2.a_3.....a_N = d^N \frac{\Gamma(\frac{a_1}{d} + N)}{\Gamma(\frac{a_1}{d})} \tag{6.15}$$

where a_1 is first term of the series with total N terms and d is common difference, equation 6.14 leads to

$$p(N) = \frac{\gamma^N}{N!}\frac{\Gamma(1+\nu)}{\Gamma(1+\nu+N)} p(0) \tag{6.16}$$

Since p(N) is a probability, normalization leads to

$$\sum_{N=0}^{\infty} p(N) = 1 \tag{6.17}$$

gives

$$p(0) = 1/\sum_{N=0}^{\infty} \frac{\gamma^N \Gamma(1+\nu)}{\Gamma(1+\nu+N)} \tag{6.18}$$

using the value of p(0) and modified Bessel function of the first kind

$$I_\nu(z) = (z/2)^\nu \sum_{N=0}^{\infty} \frac{(z^2/4)^\nu}{N!\Gamma(1+\nu+N)} \tag{6.19}$$

in equation 6.16

$$p(N) = \frac{\gamma^{(\nu/2+N)}}{I_\nu(2\sqrt{\gamma})\Gamma(1+\nu+N)N!} \tag{6.20}$$

Chapter 7

Summary and Outlook

Spatially extended systems are known to exhibit spatiotemporal pattern formation including oscillations, spirals, chemical waves and turbulence. The present work is devoted to giving deeper insight into the nature of chemical turbulence in catalytic CO oxidation on a Pt(110) single crystal surface. The reaction is a well known example of an extended system.

A focus of the work is on periodic forcing in order to control defect mediated turbulence which has been studied experimentally and numerically by using the KEE model.

It is found that resonance forcing allows turbulence in the considered system, and it can be successfully used as a tool to produce various complex patterns, but depending on the forcing frequency, period doubling cascades to chaos are also observed.

The mean frequency of the turbulent state may differ strongly from the system exhibiting homogeneous oscillations. Due to experimental noise, homogeneous oscillations are unstable, but can be simulated numerically. In contrast to the nonturbulent state, where the natural frequency of the single oscillator is identical with the oscillation frequency of the extended system, in the turbulent state the system oscillates at

higher frequencies due to diffusive interaction of the surface elements.

This is important for the definition of resonance as the generic frequency, experimentally determined as the mean oscillation frequency average over a certain area of the surface, should not be set equal to the single oscillators generic frequency, as it is sometimes found in theoretical publications [126]. Furthermore, it implies that the generic frequency in the turbulent state is more of a statistical measure than a sharply defined value. Therefore a resonance forcing frequency is used, which is in vicinity of the measured generic frequency or a harmonic of it.

The present work covers the range of 2:1 to 4:1 harmonic forcing. The following main results are found experimentally. Under 2:1 resonances forcing two different types of cluster patterns have been identified: amplitude clusters and phase clusters. In contrast to phase clusters, that just differ in their oscillation phase relative to the (sub harmonic) forcing frequency and belong to the same limit cycle, amplitude clusters indicate the coexistence of limit cycles of equal periods but different amplitudes. In both cluster types, the phase difference between the two cluster domains was π. The patterns did not show the property of phase balance, i.e., the total fractions of the medium occupied by the domains of the different clusters were different. However, phase balance is not expected in a small area of the surface as it is a global property. Stationary cluster walls could not observed probably due to the non-harmonicity of the CO oxidation. The path to chaos is given by a period doubling cascade, which could be experimentally followed by a subsequent increase of the forcing amplitude.

With the help of the new compressor, the regimes of 3:1 and 4:1 resonance forcing were successfully reached. However, the cluster formation takes place in finite regions of the surface, while other parts appear not to be 3:1 and 4:1 entrained, but still show turbulent behavior.

Numerical simulations of the KEE model support the experimental findings, and give further insight into the nature of catalytic CO oxidation. The resonant forcing is applied to the system according to the natural frequency of an extended system. Under 2:1 resonance which is in contrast to the experiments, phase clusters were found rather than amplitude clusters. Interestingly, labyrinthine patterns were found at 8:1 entrainment. The transition between two phase cluster states and the labyrinthine

pattern is induced by phase instabilities within the cluster boundary.

In 3:1 resonance forcing, the bistability between 2:1 and 3:1 could not be observed by applying the forcing according to the extended system.

At 4:1 periodic forcing, forcing with the 4^{th} harmonic of the natural frequency of the single oscillator leads to 3:1 entrained three phase patterns, 4:1 entrainment could be obtained by forcing with the 4^{th} harmonic of the mean oscillation frequency. Weak detuning leads to the appearance of turbulent regions, similar to the experimental results.

However, it was found that the greater the difference between the two characteristic frequencies (single and extended system), the more difficult it is to entrain both turbulent and phase-clustered regions. A necessary condition for entrainment of the phase clusters is that the forcing frequency lie within the respective Arnold tongue of the single oscillator. As the Arnold's tongues generally become smaller for higher harmonics, the effect of differing characteristic frequencies became more and more pronounced by forcing the system with higher frequencies. In 2:1 forcing with the natural frequency of the single oscillator leads to 2:1 entrainment, 3:1 forcing resulted in bistability of 2:1 and 3:1 entrainment [45]. 4:1 forcing finally resulted in 3:1 entrainment, while 4:1 entrainment could not be obtained.

Further investigation of high-frequency forcing of turbulent reaction-diffusion systems may give new insight into the nature of turbulence and may lead to new strategies for controlling chaos.

Further studies on cluster patterns are performed on 4:1 forcing within the nonturbulent system.

The 4:1 resonance forcing in nonturbulent regime shows the two phase traveling phase cluster experimentally. Numerical simulations of the KEE model in the nonturbulent regime reproduce stationary four phase clusters as well as two phase clusters at higher amplitudes, while other models namely the CGLE, FHN show traveling four phase clusters and stationary two phase clusters at low and high forcing amplitudes respectively [39, 78].

Finally, the spiral wave turbulence in catalytic CO oxidation was statistically charac-

terized, with increasing order of CO pressure only experimentally. By using a Hilbert transform, the experimental data was translated into phase and amplitude variables. In this representation, topological defects could be identified at higher CO pressure defining a measure for the strength of turbulence.

The temporal fluctuations in the number of defects were characterized in terms of statistical moments and probability distribution functions. On the basis of the gain and loss rates of defects, a probabilistic model was derived that yields a good approximation of the experimental results. As the CO pressure increases the probability distribution of the defect are flattened more and more and can be fitted with the modified distribution function also found in FHN and Rössler models as the noise intensity increases.

In summary, once again catalytic CO oxidation turns out to be one of the most powerful nonlinear model systems, where many effects predicted by nonlinear theory can be observed experimentally and reproduced numerically. The system allows for switching between distinct spatiotemporal chaotic states by tuning an easily accessible experimental parameter. Investigation of the complex nature of reaction-diffusion systems - as this work is a part of - may lead to improved strategies for control of extended nonlinear systems.

Bibliography

[1] J. P. Keener and J. Sneyd *Mathematical physiology. Berlin: Springer-Verlag*, 1998.

[2] C. Fall, E. Marland, J. Wagner, and J. Tyson *Computational cell biology. New York: Springer- Verlag*, 2002.

[3] J. D. Murray, *Mathematical Biology. Berlin: Springer- Verlag.* 1989.

[4] M. C. Cross and P. C. Hohenberg, "Pattern formation outside of equilibrium," *Rev. Mod. Phys.*, vol. 65, p. 851, 1993.

[5] A. J. Koch and H. Meihardt, "Biological pattern formation: from basic mechanisms to complex structures," *Rev. Mod. Phys.*, vol. 66, p. 1481, 1994.

[6] A. T. Winfree, "The geometry of biological time," *Springer, New York*, 1980.

[7] A. T. Winfree, "When times breaks down," *Princeton University Press, Princeton*, 1987.

[8] Y. Kuramoto, *Chemical oscillations, waves and turbulence.* Berlin – Heidelberg – New York: Springer-Verlag, 1984.

[9] H. Chat and P. Manneville, "Transition to turbulence via spatio-temporal intermittency," *Phys. Rev. Lett.*, vol. 58, p. 112, 1987.

[10] P. Coullet, L. Gil, and J. Lega, "Defect-mediated turbulence," *Phys. Rev. Lett.*, vol. 62, p. 1619, 1989.

[11] B. Shraiman, A. Pumir, W. van Saarloos, P. Hohenberg, H. Chaté, and M. Holen, "Spatiotemporal chaos in the one-dimensional complex Ginzburg-Landau equation," *Physica D*, vol. 57, p. 241, 1992.

[12] P. Glansdorff and I. Prigogine, "Thermodynamic theory of structure, stability and fluctuations," *Wiley, London*, 1971.

[13] G. Nicolis and I. Prigogine, *Self-Organization in Non-equilibrium Systems*. Wiley, New York, 1977.

[14] S. Jakubith, H. H. Rotermund, W. Engel, A. v. Oertzen, and G. Ertl, "Spatiotemporal concentration patterns in a surface-reaction: Propagating and standing waves, rotating spirals, and turbulence," *Phys. Rev. Lett.*, vol. 65, p. 3013, 1990.

[15] *Oscillations and Traveling Waves in Chemical Systems, edited by R. J. Field and M. Burger (Wiley, New York)*. 1985.

[16] T. Engel and G. Ertl, "Elementary steps in the catalytic oxidation of carbon monoxide on platinum metals," *Adv. Catal.*, vol. 28, p. 1, 1979.

[17] A. T. Winfree, "The prehistory of the Belousov-Zhabotinsky oscillator," *J. Chem. Educ.*, vol. 61, p. 661, 1984.

[18] A. M. Zhabotinsky, "A history of chemical oscillations and waves," *Chaos*, vol. 1, p. 379, 1991.

[19] A. N. Zaikin and A. M. Zhabotinsky, "Concentration wave propagation in two-dimensional liquid-phase self-oscillating system," *Nature*, vol. 225, p. 535, 1970.

[20] A. T. Winfree, "Spiral waves of chemical activity," *Science*, vol. 175, p. 634, 1972.

[21] I. Langmuir, "The mechanism of the catalytic action of platinum in the reactions $2CO+O_2 = 2CO_2$ and $2H_2+O_2 = 2H_2O$," *Transactions of the Faraday Society*, vol. 17, p. 0621, 1922.

[22] H. H. Rotermund, "Imaging pattern formation in surface reactions from ultra-high vacuum up to atmospheric pressures," *Surf. Sci.*, vol. 386, p. 10, 1997.

[23] R. Imbihl and G. Ertl, "Oscillatory kinetics in heterogeneous catalysis," *Chem. Rev.*, vol. 95, p. 697, 1995.

[24] V. P. Zhdanov, "Monte carlo simulations of oscillations, chaos and pattern formation in heterogeneous catalytic reactions," *Surf. Sci. Rep.*, vol. 45, p. 231, 2002.

[25] P. Hugo, "Stabilitt und zeitverhalten von durchflu - kreislauf - reaktoren," *Ber. Bunsenges. Phys. Chem*, vol. 74, p. 121, 1970.

[26] G. Ertl, P. R. Norton, and J. Rüstig, "Kinetic oscillations in the platinum-catalyzed oxidation of CO," *Phys. Rev. Lett.*, vol. 49, p. 177, 1982.

[27] E. Ott, C. Grebogi, and J. A. Yorke, "Controlling chaos," *Phys. Rev. Lett.*, vol. 64, p. 1196, 1990.

[28] R. Roy, T. W. Murphy Jr, T. D. Maier, Z. Gills, and E. R. Hunt, "Dynamical control of a chaotic laser: Experimental stabilization of a globally coupled system," *Phys. Rev. Lett.*, vol. 68, p. 1259, 1992.

[29] A. Garfinkel, M. L. Spano, W. L. Ditto, and J. N. Weiss, "Controlling cardiac chaos," *Science*, vol. 257, p. 1230, 1992.

[30] V. Petrov, V. Gspr, J. Masere, and K. Showalter, "Controlling chaos in the Belousov-Zhabotinsky reaction," *Nature*, vol. 361, p. 240, 1993.

[31] P. Parmananda, P. Sherard, R. W. Rollins, and H. D. Dewald, "Control of chaos in an electrochemical cell," *Phys. Rev. E*, vol. 47, p. R3003, 1993.

[32] M. C. Cross and P. Hohenberg, "Spatiotemporal chaos," *Science*, vol. 263, p. 1569, 1994.

[33] A. Péntek, J. B. Kadtke, and Z. Toroczkai, "Stabilizing chaotic vortex trajectories: an example of high-dimensional control," *Phys. Lett. A*, vol. 224, p. 85, 1996.

[34] P. Colet, R. Roy, and K. Wiesenfeld, "Controlling hyperchaos in a multimode laser model," *Phys. Rev. E*, vol. 50, p. 3453, 1994.

[35] V. Petrov, M. J. Crowley, and K. Showalter, "Tracking unstable periodic orbits in the Belousov-Zhabotinsky reaction," *Phys. Rev. Lett.*, vol. 72, p. 2955, 1994.

[36] K. Hall, D. J. Christini, M. Tremblay, J. J. Collins, L. Glass, and J. Billette, "Dynamic control of cardiac alternans," *Phys. Rev. Lett.*, vol. 78, p. 4518, 1997.

[37] I. S. Aranson and L. Kramer, "The world of the complex Ginzburg-Landau equation," *Rev. Mod. Phys.*, vol. 74, p. 99, 2002.

[38] P. Coullet, J. Lega, B. Houchmanzadeh, and J. Lajzerowicz, "Breaking chirality in nonequilibrium systems," *Phys. Rev. Lett.*, vol. 65, p. 1352, 1990.

[39] C. Elphick, A. Hagberg, and E. Meron, "Phase front instability in periodically forced oscillatory systems," *Phys. Rev. Lett.*, vol. 80, p. 5007, 1998.

[40] H. Chate, A. Pikovsky, and O. Rudzick, "Forcing oscillatory media: phase kinks vs. synchronization," *Physica D*, vol. 131, p. 17, 1999.

[41] H.-K. Park, "Frequency locking in spatially extended systems," *Phys. Rev. Lett.*, vol. 86, p. 1130, 2001.

[42] D. Battogtokh and A. S. Mikhailov, "Controlling turbulence in the complex Ginzburg-Landau equation," *Physica D*, vol. 90, p. 84, 1996.

[43] D. Battogtokh, A. Preusser, and A. S. Mikhailov, "Controlling turbulence in the complex Ginzburg-Landau equation II. two-dimensional systems," *Physica D*, vol. 106, p. 327, 1997.

[44] G. Franceschini, S. Bose, and E. Schöll, "Control of chaotic spatiotemporal spiking by time-delay autosynchronization," *Phys. Rev. E*, vol. 60, p. 5426, 1999.

[45] J. Davidsen, A. Mikhailov, and R. Kapral, "Front explosion in a periodically forced surface reaction," *Phys. Rev. E*, vol. 72, p. 046214, 2005.

[46] K. Krischer, M. Eiswirth, and G. Ertl, "Oscillatory CO oxidation on Pt(110) - modeling of temporal self-organization," *J. Chem. Phys.*, vol. 96, p. 9161, 1992.

[47] C. Hemming and R. Kapral, "Front explosion in a resonantly forced complex ginzburg-landau system," *Physica D*, vol. 168, p. 10, 2002.

[48] C. Hemming and R. Kapral, "Phase front dynamics in inhomogeneously forced oscillatory systems," *Physica a-Statistical Mechanics and Its Applications*, vol. 306, p. 199, 2002.

[49] K. Krischer *Dissertation, Free University of Berlin*, 1990.

[50] A. S. Mikhailov, "Foundations of synergetics I," *Springer, Berlin*, 1994.

[51] S. C. Müller and V. S. Zykov, "Simple and complex spiral wave dynamics," *Phil. Trans. R. Soc. Lond. A*, vol. 3, p. 677, 1994.

[52] P. Lipp and E. Niggli, "Microscopic spiral waves reveal positive feedback in subcellular calcium signaling," *Biophys. J.*, vol. 6, p. 2272, 1993.

[53] J. Sneyd and A. Atri, "Curvature dependence of a model for calcium wave propagation," *Physica D*, vol. 6, p. 365, 1993.

[54] P. S. Chen, A. Garfinkel, J. N. Weiss, and H. S. Karagueuzian, "Spirals, chaos, and new mechanisms of wave propagation," *Pacing and Clinical Electrophysiology*, vol. 2, p. 414, 1997.

[55] J. M. Davidenko, A. M. Pertsov, R. Salomonsz, W. Baxter, and J. Jalife, "Stationary and drifting spiral waves of excitation in isolated cardiac muscle," *Nature*, vol. 3, p. 349, 1992.

[56] H. Zhang, H. Bambi, and H. Gang, "Suppression of spiral waves and spatiotemporal chaos by generating target waves in excitable media," *Phys. Rev. E*, vol. 68, p. 026134, 2003.

[57] C. Beta, M. Moula, A. S. Mikhailov, H. H. Rotermund, and G. Ertl, "Excitable CO oxidation on Pt(110) under nonuniform coupling," *Phys. Rev. Lett.*, vol. 93, p. 188302, 2004.

[58] J. Christoph, R. Otterstedt, M. Eiswirth, N. Jaeger, and J. Hudson, "Negative coupling during oscillatory pattern formation on a ring electrode," *J. Chem. Phys.*, vol. 110, p. 8614, 1999.

[59] P. Strasser, J. Christoph, W. Lin, M. Eiswirth, and J. L. Hudson, "Standing wave oscillations in an electrocatalytic reaction," *J. Phys. Chem.*, vol. 104, p. 1854, 2000.

[60] P. Grauel, H. Varela, and K. Krischer, "Spatial bifurcations of fixed points and limit cycles during the electrochemical oxidation of H_2 on Pt ring-electrodes," *Faraday Discuss*, vol. 120, p. 165, 2002.

[61] F. Plenge, H. Varela, and K. Krischer, "Asymmetric target pattern in one-dimensional oscillatory media with genuine nonlocal coupling," *Phys. Rev. Lett.*, vol. 94, p. 198301, 2005.

[62] M. H. Jensen, P. Bak, and T. Bohr, "Transition to chaos by interaction of resonances in dissipative systems. I. circle maps," *Phys. Rev. A*, vol. 30, p. 1960, 1984.

[63] L. Glass, "Synchronization and rhythmic processes in physiology," *Nature*, vol. 410, p. 277, 2001.

[64] M. Braune and H. Engel, "Compound rotation of spiral waves in active media with periodically modulated excitability," *Chem. Phys. Lett.*, vol. 211, p. 534, 1993.

[65] O. Steinbock, A. Toth, and K. Showalter, "Navigating complex labyrinths - optimal paths from chemical waves," *Science*, vol. 267, p. 868, 1995.

[66] R. M. Mantel and D. Barkley, "Periodic forcing of spiral waves in excitable media," *Phys. Rev. E*, vol. 54, p. 4791, 1996.

[67] V. Hakim and A. Karma, "Theory of spiral wave dynamics in weakly excitable media: Asymptotic reduction to a kinematic model and applications," *Phys. Rev. E*, vol. 60, p. 5073, 1999.

[68] A. Karma and V. S. Zykov, "Structure of the resonance attractor for spiral waves in excitable media," *Phys. Rev. Lett.*, vol. 83, p. 2453, 1999.

[69] P. Coullet and K. Emilsson, "Pattern-formation in the strong resonant forcing of spatially distributed oscillators," *Physica A*, vol. 188, p. 190, 1992.

[70] C. Elphick, A. Hagberg, and E. Meron, "Multiphase patterns in periodically forced oscillatory systems," *Phys. Rev. E*, vol. 59, p. 5285, 1999.

[71] A. L. Lin, A. Hagberg, A. Ardelea, M. Bertram, H. L. Swinney, and E. Meron, "Four-phase patterns in forced oscillatory systems," *Physical Review E*, vol. 62, p. 3790, 2000.

[72] V. Petrov, Q. Ouyang, and H. L. Swinney, "Resonant pattern formation in a chemical system," *Nature*, vol. 388, p. 655, 1997.

[73] A. L. Lin, M. Bertram, K. Martinez, H. L. Swinney, A. Ardelea, and G. F. Carey, "Resonant phase patterns in a reaction-diffusion system," *Phys. Rev. Lett.*, vol. 84,, p. 4240, 2000.

[74] M. Yoneyama, A. Fujii, and S. Maeda, "Wavelength-doubled spiral fragments in photosensitive monolayers," *J. Am. Chem. Soc.*, vol. 117, p. 8188, 1995.

[75] A. Goryachev, H. Chat, and R. Kapral, "Synchronization defects and broken symmetry in spiral waves," *Phys. Rev. Lett.*, vol. 80, p. 873, 1998.

[76] M. Zhan and R. Kapral, "Model for line defects in complex-oscillatory spiral waves," *Phys. Rev. E*, vol. 72, p. 046221, 2005.

[77] B. Marts, D. J. W. Simpson, A. Hagberg, and A. L. Lin, "Period doubling in a periodically forced Belousov-Zhabotinsky reaction," *Phys. Rev. E*, vol. 76, p. 026213, 2007.

[78] A. L. Lin, A. Hagberg, E. Meron, and H. L. Swinney, "Resonance tongues and patterns in periodically forced reaction-diffusion systems," *Phys. Rev. E*, vol. 69, p. 066217, 2004.

[79] M. Bertram, C. Beta, M. Pollmann, A. S. Mikhailov, H. H. Rotermund, and G. Ertl, "Pattern formation on the edge of chaos: Experiments with CO oxidation on a Pt(110) surface under global delayed feedback," *Phys. Rev. E*, vol. 67, p. 036208, 2003.

[80] P. S. Bodega, P. Kaira, C. Beta, D. Krefting, D. Bauer, B. M. Schulz, C. Punckt, and H. H. Rotermund, "High frequency periodic forcing of the oscillatory catalytic CO oxidation on Pt(110)," *New J. Phys.*, vol. 9, p. 61, 2007.

[81] M. Bertramm, "Controlling turbulence and pattern formation in chemical reactions," *Ph.D. thesis, Technische Universitaet Berlin*, 2002.

[82] C. Beta, "Controlling chemical turbulence in surface reactions," *Dissertation, Freie Universitaet Berlin*, 2004.

[83] H. H. Rotermund, W. Engel, M. Kordesch, and G. Ertl, "Imaging of spatiotemporal pattern evolution during carbon-monoxide oxidation on platinum," *Nature*, vol. 343, p. 355, 1990.

[84] W. Engel, M. E. Kordesch, H. H. Rotermund, S. Kubala, and A. v. Oertzen, "A UHV-compatible photoelectron emission microscope for applications in surface science," *Ultramicroscopy*, vol. 36, p. 148, 1991.

[85] H. H. Rotermund, W. Engel, S. Jakubith, A. v. Oertzen, and E. G., "Methods and application of UV photoelectron microscopy in heterogeneous catalysis," *Ultramicroscopy*, vol. 36, p. 164, 1991.

[86] H. H. Rotermund, G. Haas, R. U. Franz, R. M. Tromp, and G. Ertl, "Pattern formation in surface reactions from ultrahigh vacuum up to atmospheric pressures," *Science*, vol. 270, p. 608, 1995.

[87] H. H. Rotermund, "Imaging of dynamic processes on surfaces by light," *Surf. Sci.Rep.*, vol. 29, p. 267, 1997.

[88] T. E. Jackman, J. A. Davies, D. P. Jackson, W. N. Unertl, and P. R. Norton, "A study by rutherford backscattering, nuclear microanalysis, leed and thermal-desorption spectroscopy," *Surf. Sci.*, vol. 120, p. 389, 1982.

[89] H. Niehus, "Analysis of the Pt(110)-(1 × 2) surface reconstruction," *Surf. Sci.*, vol. 145, p. 407, 1984.

[90] G. L. Kelloggm, "Direct observations of the (1×2) surface reconstruction on the Pt(110) plane," *Phys. Rev. Lett.*, vol. 55, p. 2168, 1985.

[91] P. Fery, W. Moritz, and D. Wolf, "Structure determination of the (1 × 2) and (1×3) reconstructions of Pt(110) by low energy electron diffraction," *Phys. Rev. B*, vol. 38, p. 7275, 1988.

[92] P. Fenter and T. Gustafsson, "Structural analysis of the Pt-(1 × 2) surface using medium-energy ion scattering," *Phys. Rev. B*, vol. 38, p. 10197, 1988.

[93] G. Blyholder, "Molecular orbital view of chemisorbed carbon monoxide," *J. Phys. Chem.*, vol. 68, p. 2772, 1964.

[94] G. Doyen and G. Ertl, "Theory of carbon-monoxide chemisorption on transitionmetals," *Surf. Sci.*, vol. 43, p. 197, 1974.

[95] P. H. Emmett and P. Sabatier, *Catalysis then and now. Part I: A survey of advances in catalysis*. Englewood, NJ: Franklin Publishing, 1965.

[96] R. K. Sharma, W. A. Brown, and D. A. King, "The adsorption of CO on Pt(110) over the temperature range from 90 to 300 k studied by rairs," *Surf. Sci.*, vol. 414, p. 68, 1998.

[97] C. M. Comrie and R. M. Lambert, "Chemisorption and surface structural chemistry of carbon monoxide on Pt-(1×2)," *J. Chem. Soc., Faraday Trans.*, vol. I 72, p. 1659, 1976.

[98] R. W. McCabe and L. D. Schmidt, "Adsorption of H_2 and CO on clean and oxidized Pt(110)," *Surf. Sci.*, vol. 60, p. 85, 1976.

[99] S. Ladas, R. Imbihl, and G. Ertl, "Kinetic oscillations and facetting during the catalytic CO oxidation on Pt(110)," *Surf. Sci.*, vol. 198, p. 42, 1988.

[100] P. R. Norton, J. A. Davies, and T. E. Jackman, "Absolute coverages of CO and O on Pt(111); comparison of saturation CO coverages on Pt(100), (110), and (111) surfaces," *Surf. Sci.*, vol. 122, p. L593, 1982.

[101] W. N. Unertl, T. E. Jackman, P. R. Norton, D. P. Jackson, and J. A. Davies, "Surface phases of clean, CO and NO covered Pt(110)," *J. Chem. Phys.*, vol. 20, p. 607, 1982.

[102] M. Wilf and P. T. Dawson, "The adsorption and desorption of oxygen on the Pt(110) surface; a thermal desorption and LEED/AES study," *Surf. Sci.*, vol. 65, p. 399, 1977.

[103] V. S. Sundaram and P. T. Dawson, "Oxygen on Pt(110): Thermal enhancement of electron stimulated desorption," *Surf. Sci.*, vol. 146, p. L593, 1984.

[104] S. Helveg, J. K. Norskov, and F. Besenbacher, "Oxygen adsorption on Pt(110)-(1x2): new high-coverage structures," *Surf. Sci.*, vol. 430, p. L533, 1999.

[105] R. Ducros and R. P. Merrill, "Interaction of oxygen with Pt(110)," *Surf. Sci.*, vol. 55, p. 227, 1976.

[106] N. Freyer, M. Kiskinova, G. Pirug, and H. P. Bonzel, "Oxygen-adsorption on Pt(110)-(1×2) and Pt(110)-(1×1)," *Surf. Sci.*, vol. 166, no. 1, p. 206, 1986.

[107] A. V. Walker, B. Kltzer, and D. A. King, "Dynamics and kinetics of oxygen dissociative adsorption on Pt{110}(1 × 2)," *J. Chem. Phys.*, vol. 109, p. 6879, 1998.

[108] K. Krischer, M. Eiswirth, and G. Ertl, "Bifurcation-analysis of an oscillating surface-reaction model," *Surf. Sci.*, vol. 251, p. 900, 1991.

[109] S. Ladas, R. Imbihl, and G. Ertl, "Microfacetting of a Pt(110) surface during catalytic CO oxidation," *Surf. Sci.*, vol. 197, p. 153, 1988.

[110] G. Ertl, "Oscillatory catalytic reactions at single crystal surfaces," *Adv. Catal.*, vol. 37, p. 213, 1990.

[111] R. Imbihl, S. Ladas, and G. Ertl, "The CO-induced 1×2 ↔ 1×1 phase transition of Pt(110) studied by leed and workfunction measurements," *Surf. Sci.*, vol. 206, p. L903, 1988.

[112] V. P. Zhdanov, "Periodic perturbation of the kinetics of heterogeneous catalytic reactions," *Surf. Sc. Rep.*, vol. 55, p. 1, 2004.

[113] R. P. H. Gasser and E. B. Smith, "A surface mobility parameter for chemisorption," *Chem. Phys. Lett.*, vol. 1, p. 457, 1967.

[114] M. Eiswirth, K. Krischer, and G. Ertl, "Subsurface oxygen formation on the Pt(110) surface: experiment and mathematical modeling," *Surf. Sci.*, vol. 350, p. 259, 1996.

[115] H. Beusch, E. Wicke, and P. Fieguth, "Thermisch und kinetisch verursachte Instabilitäten im Reaktionsverhalten einzelner katalysatorkörner," *Chem.-Ing.-Tech.*, vol. 44, no. 7, p. 445, 1972.

[116] M. Eiswirth and G. Ertl, "Kinetic oscillations in the catalytic CO oxidation on a Pt(110) surface," *Surf. Sci.*, vol. 177, p. 90, 1986.

[117] S. Jakubith, "Dissertation, Free University of Berlin," 1991.

[118] H. H. Rotermund, S. Jakubith, A. von Oertzen, and G. Ertl, "Solitons in a surface-reaction," *Phys. Rev. Lett.*, vol. 66, p. 3083, 1991.

[119] K. C. Rose, D. Battogtokh, A. Mikhailov, R. Imbihl, W. Engel, and A. M. Bradshaw, "Cellular structures in catalytic reactions with global coupling," *Phys. Rev. Lett.*, vol. 76, p. 3582, 1996.

[120] S. Nettesheim, A. von Oertzen, H. H. Rotermund, and G. Ertl, "Reaction-diffusion patterns in the catalytic CO oxidation on Pt(110) - front propagation and spiral waves," *J. Chem. Phys.*, vol. 98, p. 9977, 1993.

[121] A. v. Oertzen *Diploma Thesis, Free University of Berlin*, 1990.

[122] H. H. Rotermund, "Imaging surface reactions with a photoemission electron microscope," *J. Electron. Spectrosc.*, vol. 98-99, p. 41, 1999.

[123] A. v. Oertzen, "Dissertation, Free University of Berlin," 1992.

[124] M. Bertram, C. Beta, H. H. Rotermund, and G. Ertl, "Complex patterns in a periodically forced surface reaction," *J. Phys. Chem. B*, vol. 107, p. 9610, 2003.

[125] D. S. Scientic, "Foundations of vacuum technique," *Wiley, New York*, 1949.

[126] P. Kaira, P. S. Bodega, C. Punckt, H. H. Rotermund, and D. Krefting, "Pattern formation in 4:1 resonance of the periodically forced CO oxidation on Pt(110)," *Phys. Rev. E*, vol. 77, p. 046106, 2008.

[127] M. Falcke, H. Engel, and M. Neufeld, "Cluster formation, standing waves, and stripe patterns in oscillatory active media with local and global coupling," *Phys. Rev. E*, vol. 52, p. 763, 1995.

[128] A. S. Mikhailov and K. Showalter, "Control of waves, patterns and turbulence in chemical systems," *Physics Reports*, vol. 425, p. 79, 2006.

[129] C. Hemming and R. Kapral, "Turbulent fronts in resonantly forced oscillatory systems," *Faraday Discussions*, vol. 120, p. 371, 2001.

[130] Q. Ouyang and J.-M. Flesselles, "Transition from spirals to defect turbulence driven by a convective instability," *Nature*, vol. 379, p. 143, 1996.

[131] C. Beta, A. S. Mikhailov, H. H. Rotermund, and G. Ertl, "Defect-mediated turbulence in a catalytic surface reaction," *Europhysics Letters*, vol. 75, p. 868, 2006.

[132] S. Morris, E. Bodenschatz, D. S. Cannell, and G. Ahlers, "Spiral defect chaos in large aspect ratio rayleigh-bénard convection," *Phys. Rev. Lett.*, vol. 71, p. 2026, 1993.

[133] K. E. Daniels and E. Bodenschatz, "Defect turbulence in inclined layer convection," *Phys. Rev. Lett.*, vol. 88, p. 034501, 2002.

[134] I. Rehberg, S. Rasenat, and V. Steinberg, "Travelling waves and defect-initiated turbulence in electroconvecting nematics," *Phys. Rev. Lett.*, vol. 62, p. 756, 1989.

[135] P. L. Ramazza, S. Residori, G. Giacomelli, and F. T. Arecchi, "Statistics of topological defects in linear and nonlinear optics," *Europhys. Lett.*, vol. 19, p. 475, 1992.

[136] L. Gil, J. Lega, and J. L. Meunier, "Statistical properties of defect-mediated turbulence," *Phys. Rev. A*, vol. 41, p. 1138, 1990.

[137] H. Wang and Q. Ouyang, "Effect of noise on defect chaos in a reaction- diffusion model," *Chaos*, vol. 15, p. 023702, 2005.

[138] H. Wang, "Statistics of defect-mediated turbulence influenced by noise," *Phys. Rev. Lett.*, vol. 93, p. 154101, 2004.

Publications

- P. S. Bodega, P. Kaira, C. Beta, D. Krefting, D. Bauer, B. Mirwald-Schulz, C. Punckt, and H. H. Rotermund. High frequency periodic forcing of the oscillatory catalytic CO oxidation on Pt(110). New Journal of Physics 9 (2007) 61.
- P. Kaira, P. S. Bodega, C. Punckt, H. H. Rotermund, and D. Krefting. Pattern formation in 4:1 resonance of the periodically forced CO oxidation on Pt(110). Physical Review E 77 (2008) 046106.
- D. Krefting, P. Kaira, and H. H. Rotermund. Period doubling and spatiotemporal chaos in periodically forced CO oxidation on Pt(110). Physical Review letter, submitted.
- P. Kaira, D. Krefting, C. Beta, and H. H. Rotermund. Effect of CO pressure on defect-mediated turbulence in a catalytic surface reaction. New Journal of Physics, in preparation.
- P. Kaira, D. Krefting, P. S. Bodega, C. Punckt, and H. H. Rotermund. Pattern formation in 3:1 resonance of the periodically forced surface reaction. In preparation.
- C. Punckt, P. S. Bodega, P. Kaira, and H. H. Rotermund. Forest fires in the lab: experiments, simple modeling, and relation to other phenomena. In preparation.

Acknowledgements

First of all, I would like to thank my supervisor Prof. Harm. H. Rotermund for giving me an opportunity to make this work within his group at the Fritz-Haber-Institute, for encouraging and supporting me throughout my PhD. His ingenuity, enthusiasm and extreme kindness will always be in my memory. I am truly honoured that I could work in his outstanding group.

I would also like to acknowledge Prof. Gerhard Ertl, who provided me ideal conditions to carry out my PhD work in his department.

I want to thank Prof. Harald Engel, for taking on the responsibility of being my second supervisor at the Technische Universität Berlin.

I would also like to thank Dr. Dagmar Krefting for her support and countless discussions in the frames of this research work and outside, and for spending many hours to carefully read and correct my thesis.

Dieter Bauer, for his friendly help and assistance in the experiments, numerous technical improvements and many helpful comments.

Prof. Dr. Alexander S. Mikhailov, Dr. Sergio Alonso, Dr. Carsten Beta, and Dr. Oliver Rudzick for helpful discussions.

I am very grateful to my colleagues and friends, especially to Pablo Sánchez Bodega, Christian Punckt, Willi Krauss, Dai Zhang, Katrin Domke, Monika Dornhege, Pablo Kaluza, Peter Klages, Yuichi Togashi, Mirwald-Schulz Birgit, Santiago Gil, Michael Stich, and Waruno Mahdi.

This work would not have been possible without the support and encouragement from

my husband, Pushkar Singh. He has been extremely patient, understanding, and loving throughout my research.

Finally, I would like to thank my family for their unconditional support.